ALMA MATER STUDIORUM
UNIVERSITÀ DI BOLOGNA

Dottorato di ricerca in Fisica

XXXVII ciclo

Settore concorsuale: 01/A4 - FISICA MATEMATICA
Settore scientifico-disciplinare: MAT/07 - FISICA MATEMATICA

Applications of Delay Differential Equations to the Physics of Complex Systems

Presentata da:
Giulio Colombini

Coordinatore Dottorato:
prof. Alessandro Gabrielli

Supervisore:
prof. Armando Bazzani

Co-supervisore:
prof. Daniel Remondini

Esame finale anno 2025

Non so che storia è questa,
non so cosa pensar.
Ma quel ch'è fatto è fatto,
e non si può cangiar.

VICENTE MARTÍN Y SOLER,
Una cosa rara,
Atto Primo, Scena XVIII.
1786, Vienna

Abstract

In the physical study of Complex Systems where a large number of components in interaction exhibits emergent collective states the typical models are formulated in terms of coupled dynamical systems on a graph structure. This is a natural choice on the one hand, as collective states are understood to be generated by the interplay of a component-intrinsic dynamics and the structure of interactions between different components, and a convenient one on the other, since it allows scientists to implement dynamics and structure into a model in two separate steps, highlighting the role of each in the behaviour of entire systems. Furthermore, with very few exceptions, most of the interaction networks which we observe in Nature are revealed by some kind of dynamical process that can be modeled as taking place on them, making networked dynamical systems a paradigmatic example also in the problem of network reconstruction.
Most of the available results on the dynamics of network-coupled dynamical systems are formulated for coupled linear systems or by linearizing in the vicinity of equilibrium solutions. This is due to the relatively simple relationships that exist in this case between the spectral properties of the network matrices and the global properties of the dynamics and to the possibility of interpreting them as mean field models for random walks on a network. On undirected networks in particular the relaxation to an equilibrium state is granted under very broad detailed balance conditions, and in presence of directed links strong correspondences have been proved between topological features of the network and dynamical properties of the system. Nevertheless, most Complex Systems are investigated at a mesoscopic scale, and thus incorporate some degree of nonlinearity and directionality of interaction. For this reason, a renewed interest is developing in these more realistic models.
In the present Thesis, we focus our attention on how the intertwining of time scales plays a very important role in the emergence and self-sustainance of collective states in these models, and propose an effective approach to account for these effects based on Delay Differential Equations. We concentrate our attention on models related to neuronal phenomena and epidemiological forecasting. Our work on neural models mainly consists in the elucidation of how

neural spiking and refractoriness time scales interact with each other and with cyclic structures in a directed interaction network giving rise to self-sustained traveling waves, which could be a nonlinear analogue of the Non Equilibrium Steady States of linear systems. We also build a description of the bifurcation phenomenon and the dynamical steady state in terms of a single Delay Differential Equation, which is equivalent up to global properties, and can be considered the equivalent for this type of traveling wave states of the synchronous manifold equation used in the Master Stability Function framework. Focusing on systems that exhibit privileged locations in phase space we formulate a simple normal form model to explain how the interplay of a delayed feedback and the natural timescale of the system can stabilize a periodic structure in the vicinity of the mentioned locations. In light of the recent interest in neural computation and information processes we also consider the problem of constructing a discrete stochastic model that can preserve the activation statistics of a full nonlinear model in presence of noise, with a particular focus on the different time scales involved in the process.

The results on epidemiological modeling are mainly concerned with the usage of Distributed Delay Differential Equations in the forecast of epidemic events on the short and medium term on a metropolitan scale in Bologna. We show that these models can cover for the shortcomings of models based on Ordinary Differential Equations at the considered scales, despite the more complicated nature of Delayed Equations. In particular we study the possibility of using traffic data as a proxy for model parameters on which otherwise a regression should be performed, and find that these can be a valid device to reveal changes in transmissive contact rates, on periods when other factors can be considered to be approximately unchanging. We also set a basis for quantitative predictivity analysis, by obtaining linear response laws for the model and in particular for the variables used in the regression process.

Contents

Introduction

The Physics of Complex Systems deals with all those problems where a great number of systems are in interaction and their dynamical properties give rise to non-trivial collective states, which have often been studied in their own right as elementary objects in other sciences or disciplines. The generality of the definition we have just given preludes to the wide variety of Complex Systems that surround us, as the perspective at which this branch of Physics typically situates itself is a mesoscopic one, at the interface between a Dynamical Systems and Statistical Physics approach thus addressing in general the emergent properties of ensembles of interacting units. Because of this perspective situated at an intermediate scale, the typical model considered in this branch of Physics consists of a set of dynamical systems coupled according to a network structure, unless one is considering purely structural or relational studies where networks are merely used to express relationships between objects. This is a natural choice, as at the mesoscale emergent behaviours are dictated in general by an interplay of local dynamics, i.e. the processes proper of each network node, and their interactions, which due to the scales at play one can neither neglect nor treat in an average sense. While the concept of graph as a mathematical object had been introduced historically by Euler, the realization of the power of a network formalism in tackling complex and emergent phenomena is a relatively recent development.

Several examples can be found from very different fields. In the study of human mobility often one considers networks with nodes which exchange agents representing individuals, cars or means of transportation, in a natural schematization of transportation networks at various scales [24, 67]. The spreading of epidemics can analogously be approached through this class of models [74], where nodes can represent individuals linked by a network of social contacts, or also metapopulations, i.e. points of interaction where the infective dynamics takes place, letting the network structure consequently represent mobility patterns and the transfer of population from one interaction point to another [85]. In the modelling of ecosystems, networks are often used to represent relationships between species [57], and can be endowed with dynamics to represent predation or more complex metabolic relationships [1]. Another classical example of dynamical systems on networks, and one of the earliest fields to adopt the network formalism, is the study of complex chemical reactions [5],via models where nodes represent chemical species and links, usually directed and weighted, the reactions with the associated rates. Recently, in response to the challenges posed by climate change, dynamical network models have been employed also in the study of climate, in particular to model cascades of tipping elements and their interaction [22, 97]. Finally, perhaps the most famous application of dynamical systems on graphs is in the field of neural networks. The network models used in the study of neural phenomenology are many and highly variegated [9], but since we are interested in the Physics of such models we will concentrate on those that include a dynamical behaviour. The microscopic structure of the nervous system, with neurons that have an internal dynamics and that can exchange signals through synapses, is very well suited to be described in good approximation by dynamical systems, representing the neurons, coupled according to a network representing the synapses. This microscopical approach was pioneered already in the 1940s by McCulloch and Pitts [65], who introduced a very simple discrete neural model with a binary activation level. Despite its simplicity, a networked population of such neurons has been proved in subsequent years to be a Turing complete computing model [19], and to model associative memory phenomena [50], shedding light on the divide between the way in which machines and human beings recall previously stored information. More recently, the usage of dynamical neural networks has seen a surge as a method of information processing, with a progressive detachment from physiological modeling, towards a purely technological endeavor, aimed to the improvement of prediction and data generation capabilities of network models. The questions related to networks of realistic neurons, though, are far from being completely understood. Indeed, while some issues regarding the synchronization transition on undirected structures have been addressed [60], many aspects of the dynamics still need to be characterized when one considers directed architectures, which are the natural formulation ground for neural models. Finally, there has recently been a renewed interest in the study of the computation capabilities of realistic neural units, in the field of reservoir computing [2]. This is particularly interesting for an investigation of the role of structure and dynamics in defining information processing, as it allows on the one hand to access structural and dynamical properties of the system quite easily, and on the other hand to define quite straightforwardly the information processing capabilities, by framing them as a machine learning task.

In the context of dynamical network models, the properties of the interaction network are reflected into properties of the coupling matrix that enters the dynamical equations of the coupled system. In particular, when Laplacian couplings are considered, the spectrum of the Laplacian matrix carries a large amount of information regarding the network topology [18], and this information is reflected into the dynamics. The relationship between a network topology and the dynamical phenomena that take place on it has generally been studied in linear models [88], where the simplicity of the dynamics allows for a better investigation, and to directly construct the stable attractive solution from graph theoretical considerations. In this picture, the detailed balance condition on the link weights is sufficient to ensure stability of the equilibrium solution. Following the same approach it is possible to establish a connection between the directed cycles present in the network and the independent currents that can be identified on it. Additionally, by recognizing that the linear master equation on a network corresponds to a mean field model for an associated random walk on the same structure, it is possible to unify the study of properties of both system, so that cycles can further be connected to the emergence of steady currents, linked to the so called Non Equilibrium Steady States (NESS) in a Markovian Dynamics on the network.

However, when considering mathematical models for real complex systems, it is common to encounter some degree of nonlinearity. Although linear systems are fundamental to the formulation and development of key mathematical results and physical intuition, they often fail to capture the phenomenology typical of actual complex systems. These features, from a mathematical perspective, can only be introduced by incorporating nonlinearities at some stage during model construction. For example the mass-action dynamics, the applications of which extend far beyond physical chemistry to most models of population and contagion dynamics, is inherently nonlinear. In social systems, nonlinear models have been successfully applied to a range of phenomena, including marriage dynamics [33], panic transitions, and traffic congestion on roads [68]. Among the most prolific fields for nonlinear dynamics are the research areas of mathematical biology and biophysics. Nonlinearity is ubiquitous at all scales in these disciplines, from micro to macroscopic systems. At the cellular scale, nonlinear ordinary differential equations (ODEs) are commonly used to model genetic regulatory networks [77] and cell metabolism [20]. A specialized area at the single-cell level focuses on modeling membrane potentials and ionic channel exchange in excitable cells, such as neurons and cardiac tissue [29, 31, 45, 47, 53, 71], where several notable historical results have been achieved, of which we give a brief account in **Chapter 1**. At the systemic scale, nonlinear dynamics are classically applied in fields such as immunology, viral reproduction dynamics [73], and erythrocyte homeostasis [63].

Whenever network structure and nonlinearity are combined the established picture based on the properties and the dynamics of the master equation and its analogue random walk gets considerably more complicated. In the case of undirected networks, the main problem that has been addressed is that of synchronization, i.e. the class of phenomena where the interaction structure affects the local node dynamics in such a way to generate a coordinated motion of all the nodes. This can be considered in some sense a paradigmatic example of the effects of the interaction between structure and dynamics in networked dynamical system, as the compromise solution characterizing the synchronized state is created explicitly by the interplay of these two elements. The most classical model in this context is due to Kuramoto [56], who formulated it for simplicity on a complete graph. A general framework to study the stability of global synchronous states exists [75], and it can be extended to study the road to synchronization, i.e. the cascade of partially synchronized macroscopic states through which a dynamical network reaches a global synchronization solution [10]. Despite its flexibility, that even allows to consider in some approximation delay-coupled systems [59], the main drawback of this approach lies in its lack of general applicability to directed coupling networks. Indeed the study of signal propagation in directionally coupled networks of dynamical systems has been studied mostly in a phenomenological way so far, e.g. through numerical simulations [42], revealing that when nonlinearity is involved, the time scales of local processing, dictated e.g. by the dynamical system reaction time, and those characterizing propagation may interact with each other in determining the spreading of perturbations on the network. Particularly in propagation phenomena, delay effects emerge, and these can play a role in the local stabilization of dynamical solutions that in the original system would not be able to be self-sustained.

It is in this context that we can situate **Chapter 2** of the present thesis. In this Chapter we address the emergence of persistent stationary solutions as a consequence of the interplay of a neuron-like spiking dynamics and a loop structure. In particular we find that such stable states are not originating from a Hopf bifurcation of the system's fixed point, corresponding to physiological stationarity, but from a limit cycle saddle node bifurcation, that leaves unaltered the system properties in the rest of phase space. Building on the intuition that the bifurcation is caused by the interplay of reaction and propagation time, we formulate an equivalent model that can express the same dynamical stationary state as the limit cycle of a Delay Differential equation, where the explicit delay is set in function of the inter-site propagation time of the nonlinear wavefront. Observing the shape of the limit cycle stabilized by the action of delayed feedback, which rests for an extensive fraction of time in the vicinity of a system nullcline, we conjecture that the mechanism of stabilization of this orbit rests in its *quasi-invariance*, i.e. in the fact that the system is naturally brought near it by the nonlinear part of its dynamics, spending there a long time despite eventually being attracted by a global fixed point.

We develop this intuition in **Chapter 3**, wherein we formulate a simplified model to address the problem analytically. By leveraging the formalism of Birkhoff normal forms and adapting it to the case of an isolated quasi-invariant orbit, and are able to show in an *ad hoc* adiabatic *ansatz* that the interplay between a skew feedback with an explicit delay and the system's natural timescale is able to stabilize the quasi-invariant structure. Moreover, we are able to build a sequence of finite dimensional approximants to the full infinite dimensional dynamical system in a perturbative approach, which at the two lowest perturbative orders display already the same bifurcation of the full model, showing the phenomenon is planar, at least at its onset. By tracing back to the FitzHugh-Nagumo system we show in a quasi-adiabatic approximation that the system possesses an isolated quasi-invariant orbit, so that the stabilization mechanism can in principle be the same of the simplified system. We conclude the Chapter by summarizing some features observed on a unidirectional chain of simplified system. The delay stabilization of limit cycles is not an entirely new topic, as some seminal contribution to the theory have been given by Pyragas [81, 82], who has investigated the problem in the framework of control theory for chaotic systems. We remark that the key assumption of Pyragas control, which is the identification of feedback delay and stabilized orbit period, is justified in chaotic systems that possess a dense spectrum of frequencies, but does not necessarily hold in our approach, which is able to predict stabilization also for macroscopic differences between the natural period of the system and the feedback delay.

An inherent capability of many networks of active elements is some degree of information processing, transmission and storage. This is expected for example in genetic regulatory networks [92], where information clearly is transmitted from the DNA to the expressed proteins, but regulatory mechanisms must ensure that also the opposite is in some measure true. Similarly, the immune system has been considered as computationally capable, due to the complex reaction mechanisms it implements [21]. Finally, above all others, the nervous system is capable of all these three types of operation with respect to information sources, making an approach via information theory desirable and likely fruitful in terms of insight on the information processing role of dynamics and structure. An obstacle to this development is the fact that information theoretical measures are most easily defined on discrete systems, and the *a posteriori* discretization of a nonlinear dynamical system orbit can be a highly non-trivial task. For this reason in **Chapter 4** we set out to formulate a simplified discrete system that can preserve the firing statistics of a FitzHugh-Nagumo nonlinear differential equation in presence of noise. We do this by framing the system as a Kramers escape rate problem, with a slow dependence of the potential wells on the time since the last activation, closing the equations for the interspike time distribution in an approximated setting. With this distribution we are able to construct, up to a parametric regression on data generated by the full neuron dynamics, a binary neuron with a refractoriness mechanism that reproduces the single neuron firing statistics to a good accuracy. When a loop of these simplified neurons is considered, we observe qualitatively similar but quantitatively different dynamical states with respect to the full FitzHugh-Nagumo case, highlighting once again how the timescale interplay is relevant in these systems, so that any discretization or coarse graining of the dynamics must be effected while preserving these relationships.

Finally, in **Chapter 5** we present a typical application of Delay Differential Equations to epidemiological modeling. Despite being formulated for the first time in terms of Delay Differential Equations [54], the most commonly used compartmental models are in general nonlinear Ordinary Differential Equations. While giving acceptable results for large populations, and in describing general epidemiological trends on longer periods, ODE based models tend to be less reliable in short-to-middle range forecasting, and for smaller populations, such as that of a city. Furthermore, whenever a disease presents highly varying time scales, such as SARS-CoV-2 , which range from a few days of infectivity to months of temporary immunity, the *effective* representation of timescale separation which is implemented in regular SIR models via transition rates starts to show its shortcomings. In addition SARS-CoV-2 incubation times can have large inter-patient variations, so that any effective model for medium-sized populations should encode it in its dynamics. Tasked with the realization of a model to predict the hospitalization trend in the Bologna Metropolitan Area, we have developed a distributed delay compartmental model for SARS-CoV-2 disease. Through a weekly regression procedure on the new positive cases, we were able to follow the development of pandemic waves in the region of interest, and aid the local health unit in its readiness effort. Proceeding semi-analytically we are able to perform linear response studies on this distributed delay equation, and study extensively the sensitivity of the solutions on a change in the regression parameter. The regression parameter, interpreted as a sociability index measuring the relative number of unprotected social contacts between individuals per unit time, has been compared to a normalized mobility proxy obtained from magnetic coil data available through open data policies of the local administration. A significant correlation has been found between the two time series, that could be enhanced by performing additive shifts in correspondence of periods characterized by different requirements in terms of personal protection devices but by roughly similar levels of mobility restrictions.

1 | Elements of dynamical neural modeling

The most significant electrophysiological characteristic of a neuron is its excitability, i.e. its capacity to rapidly depolarize and repolarize relative to its resting membrane potential, generating a sudden spike called an action potential, depicted in Figure 1.1, in response to electrical and chemical changes in the surrounding extracellular medium. By membrane potential we refer to the difference in electric potential between the interior and exterior of the cell membrane, i.e., the intracellular and extracellular media. A brief summary of the electrophysiological mechanisms underlying this phenomenon is provided here, following the exposition of [53], to which the interested reader is referred for a more detailed explanation of the dynamical aspects of neurophysiology, and the fundamental contributions to their modelization.

1.1 | Elements of physical chemistry of action potential generation

The currents involved in neuronal electrophysiology are ionic in nature, with charge carriers primarily consisting of Na^+, K^+, Ca^{++}, and Cl^-. Potassium $K^+$and negatively charged molecules, which are usually grouped together under the symbol A^-, are predominantly found in the intracellular medium, while calcium ions Ca^{++}, sodium ions Na^+, and chlorides $Cl^-$are more concentrated outside the cell. The cellular membrane, which separates the intracellular and extracellular environments, consists of a phospholipidic double layer that is impermeable to ions. However, it contains protein channels that permit the passage of these ions according to their electrical potentials and concentration gradients, except for A^-, which are too large to pass through. In theory, ions can redistribute across the membrane to reduce concentration asymmetries between the intracellular and extracellular mediums. In practice, however, this is not always the case, as the only significant currents that flow solely due to this

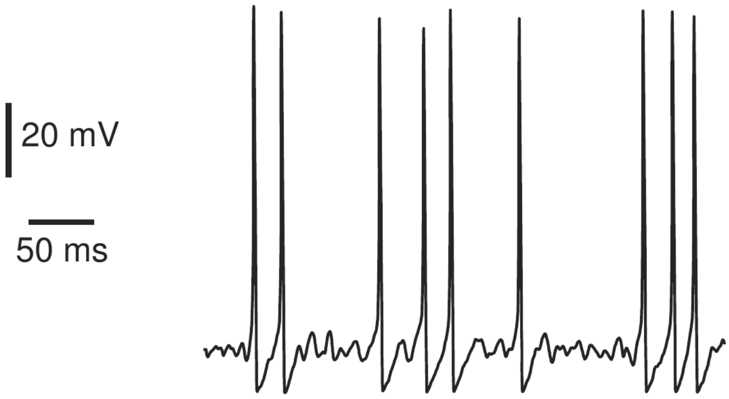

FIGURE 1.1: Membrane potential time series for a mesencephalic neuron subject to noisy input. Image from [53].

mechanism are those of $K^+$and Cl^-. Moreover, even for these ions, the concentration gradient alone is insufficient to eliminate the concentration asymmetry, as several mechanisms work to maintain these imbalances. Among the most relevant we mention:

- passive redistribution mechanisms, due to the electrostatic interaction of the A^- species, that attract $K^+$and repel Cl^-but are constrained by their size to remain within the membrane, as they do not fit through any of the channels, and thus contribute to the preservation of asymmetry,

- active transport mechanisms, due to the presence across the membrane of active *ion pumps*, such as the Na^+-K^+pump, that brings within the cell two $K^+$for each three Na^+that it releases in the extracellular medium, maintaining the concentration of K^+higher inside the cell.

If we were to consider only the mechanisms responsible for maintaining the concentration gradient, the ionic current driven by concentration asymmetry would continue to flow indefinitely. However, since ions carry electric charges, we must account for the electrical effects of their movement. For instance, in the case of K^+, the outward flow of potassium ions gradually accumulates positive charge outside the membrane and negative charge inside, due to the remaining A^- ions. This buildup creates a potential difference between the interior and exterior of the cell. Eventually, equilibrium is reached when the concentration-driven current is counterbalanced by the current resulting from the electrical potential difference. The value of this potential difference, at which the two opposing forces are in balance, is called the *Nernst equilibrium* *potential*, and it depends on the specific ionic species in question, as well as environmental factors such as temperature. In this context, if E_S denotes the Nernst potential for a given species S, the current of ion species S driven by a total membrane potential difference V can be described by

$$I_\mathrm{S} = g_\mathrm{S}\left(V - E_\mathrm{S}\right), \tag{1.1}$$

where g_S is the conductance of the ion channel associated to species S. We will comment soon more specifically on the form of this conductance. Now, if we consider Equation (1.1), for the four major ion species mentioned before, and treat the impermeable membrane as a capacitor of capacitance C [1] we are able to formulate an *equivalent circuit model* for the membrane.

$$C\dot{V} = I - g_\mathrm{Na}(V - E_\mathrm{Na}) - g_\mathrm{Ca}(V - E_\mathrm{Ca}) - g_\mathrm{Cl}(V - E_\mathrm{Cl}) - g_\mathrm{K}(V - E_\mathrm{K}) \tag{1.2}$$

where I is the total current across the membrane. Now, if all the channels were *Ohmic*, i.e. if the conductances were all constants, for $I = 0$ the system would simply relax to a weighted average of the Nernst potentials

$$V_\mathrm{rest} = \frac{g_\mathrm{Na}E_\mathrm{Na} + g_\mathrm{Ca}E_\mathrm{Ca} + g_\mathrm{Cl}E_\mathrm{Cl} + g_\mathrm{K}E_\mathrm{K}}{g_\mathrm{Na} + g_\mathrm{Ca} + g_\mathrm{Cl} + g_\mathrm{K}} \tag{1.3}$$

which for $I \neq 0$ is simply displaced

$$V_\mathrm{rest} \to V_\mathrm{rest} + \frac{I}{g_\mathrm{Na} + g_\mathrm{Ca} + g_\mathrm{Cl} + g_\mathrm{K}} \tag{1.4}$$

This behavior is overly simplistic compared to the complicated phenomenology observed in neurons, indicating that some crucial feature is missing to explain the typical spiking activity of neural cells. The key missing element lies in the fact that, with the exception of some K^+or Cl^-channels, membrane ion channels are *not* Ohmic. Their conductances are generally nonlinear and depend on a multitude of other factors. This phenomenon is known as *channel gating*. Ionic channels are large protein structures with aqueous pores that permit ion transit. These channels, although, may also be associated with gating particles that can open or close the channel depending on certain conditions in the surrounding environment, known as gating variables. The most common gating mechanisms include:

- Voltage gating: the opening or closing of a gate depends on the membrane potential → K^+, Na^+channels

---

[1] An average value for the specific membrane capacitance per membrane surface unit is given as 0.90 ± 0.03 μF/cm^2 for neurons in [30].

- Intracellular agent gating: the gating variable for a species can be the concentration of another ionic species → Ca^{++}-gated K^{+}channels
- Extracellular agents (neurotransmitter) gating: opening and closing can be triggered by some neurotransmitter substance in the extracellular medium → γ-Aminobutyric acid (GABA), N-Methyl-D-aspartic acid (NMDA) gated channels

This being said, the study of gating dynamics is a rich field of research in its own right. Typically, the phenomenon is treated as probabilistic in nature, with activation and inactivation probabilities evolving over time as functions of the relevant gating variables, from such models it is then possible to reconstruct deterministic gating dynamical equations via mean field approaches, but a treatment of such topics exceeds the scope of the present work.

1.2 | The Hodgkin-Huxley model of neural excitability

One of the most influential models that incorporate gated channels to reproduce neuronal electrophysiology, and perhaps the most physiologically complete, is the Hodgkin-Huxley model [47]. Originally developed to model the squid giant axon, it is now widely regarded as representative of the general dynamics of neurons. Through experimental observations, Hodgkin and Huxley identified the key ionic channels and gating mechanisms responsible for the system's behavior, which include:

- a voltage-gated K^{+}current I_{K}, with four activation gates,
- a voltage-gated Na^{+}current I_{Na}, with three activation and one inactivation[2] gate,
- an Ohmic leak current I_{L}, mostly carried by Cl^{-}ions.

---

[2] A closed and an inactivated channel correspond to different situations: in the first case, an activation gate simply has simply not opened, while in the second an inactivation gate has closed a channel previously opened by an activation gate.

from which the resulting dynamical equations are

$$\begin{aligned} C\dot{V} &= I - \overbrace{\bar{g}_{\mathrm{K}} n^4 \left(V - E_{\mathrm{K}}\right)}^{I_{\mathrm{K}}} - \overbrace{\bar{g}_{\mathrm{Na}} m^3 h \left(V - E_{\mathrm{Na}}\right)}^{I_{\mathrm{Na}}} - \overbrace{\bar{g}_{\mathrm{L}} \left(V - E_{\mathrm{L}}\right)}^{I_{\mathrm{L}}} \\ \dot{n} &= \alpha_n(V)(1-n) + \beta_n(V)n \\ \dot{m} &= \alpha_m(V)(1-m) + \beta_m(V)m \\ \dot{h} &= \alpha_h(V)(1-h) + \beta_h(V)h, \end{aligned} \tag{1.5}$$

where the variables n, m, and h represent the activation probability for the K^+channel and the activation and inactivation probabilities for the Na^+channel, respectively. Each of these channel types has numerous specimens embedded in the membrane, resulting in a large number of gates, so that a mean field approach is justified and one can treat the activation and inactivation probabilities as the average fractions of gates that are activated or inactivated at any given time. The functions $\alpha(V)$ and $\beta(V)$ describe the transition rates between states. $\alpha(V)$ is typically taken to be a sigmoidal function, while $\beta(V)$ is generally chosen in an exponential form. These functions contain numerical constants that depend on the choice of the origin for the potential and the physical properties of the specific system under study.

1.3 | The FitzHugh-Nagumo model neuron

Although being very sound from a physiological point of view, the Hodgkin-Huxley model has several practical drawbacks. Due to its highly nonlinear dynamics, it can exhibit many different and possibly chaotic behaviours, which are quite difficult to study in four dimensions, as many techniques, and especially the phase plane methods that can be used for nonlinear two-dimensional systems, are much more difficult to apply in this context. For these reasons Richard FitzHugh and Jinichi Nagumo developed independently the so called FitzHugh-Nagumo model [29, 71] for neural excitability. The FitzHugh-Nagumo model can be regarded either as a 2D projection of the Hodgkin-Huxley model, as recognised by the author in the original paper [29], or as a modified version of the Van Der Pol oscillator in presence of a constant force, that can displace and stabilize its fixed point in order to account for excitable behaviour. Its dynamics is specified by two nonlinear Ordinary Differential Equations, characterised by the presence of two separate time scales, describing respectively the reactive and the refractory effects that concur in defining neural dynamics. Many formulations have been proposed, among which we choose, for simplicity

$$\begin{aligned} \varepsilon\dot{u} &= u - \frac{u^3}{3} - v + I_{\text{ext}}(t) \\ \dot{v} &= u + a, \end{aligned} \tag{1.6}$$

where u is the fast variable, presenting a *quasi-threshold* spiking dynamics, akin to the membrane potential. Conversely, the slow variable v is a recovery variable, representing the characteristic refractoriness of neurons after firing. The separation between the two time scales is dictated by the factor ε, so that the fast timescale is ε^{-1} times faster than the slow one. I_{ext} is an external stimulus, possibly representing currents given by the interactions with other neurons, or by external inputs. Finally, a is a dynamical parameter regulating the dynamical regime of the model. Indeed, the system possesses a single fixed point $(u^*, v^*)^T = \left(-a, -a + \frac{a^3}{3}\right)^T$ that is stable for $|a| > 1$ and becomes unstable for $|a| < 1$, when the system undergoes a supercritical Hopf Bifurcation and a stable limit cycle appears.

The first dynamical regime, for $|a| > 1$ is termed *excitable*, and can be interpreted physiologically as that of a standard neuron, whereas the second is called a *tonic spiking* state, and can be ideally interpreted as typical of a pacemaker neuron. To understand the mechanisms of spike production in the FHN system we can analyse its Phase Space (Figures 1.2, 1.3). We draw the *nullclines*, the curves along which the time derivative of one of the variables is zero. The v-nullcline takes the form of a vertical line at $u = -a$, while the u-nullcline is a cubic curve, intersecting the u axis at $-\sqrt{3}$, 0 and $\sqrt{3}$, with a minimum at -1 and a maximum at 1. The right and leftmost branches of the nullcline are identified respectively with the physiological *refractory* and *active* phases of the neuron. In the tonic spiking regime, the limit cycle can be described as composed of four stages:

1. slow upward motion, roughly along the right (active) branch
2. fast jump towards the left branch
3. slow downward motion, roughly along the left (refractory) branch
4. fast jump towards the right branch

In the tonic activity phase, these stages are indefinitely repeated.

In the excitable phase, the fixed point is stable, and the unperturbed system tends to approach it by following the cubic nullcline. For instance, if we consider a positive value of $a > 1$, the fixed point will lie on the left branch of the cubic nullcline. When a brief positive shock is applied via the I_{ext} variable, the

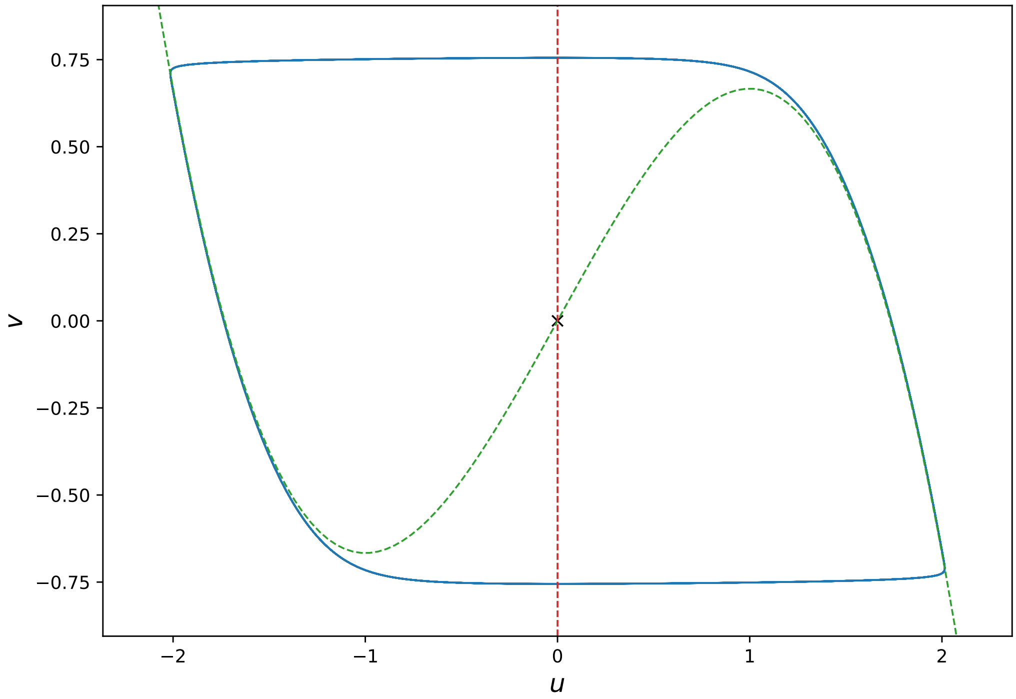

FIGURE 1.2: Phase space plot for the FHN system in the tonic spiking phase ($a = 0.8$, $\varepsilon = 0.01$). The dashed lines are respectively the u (green) and v (red) nullclines. The × marks the global fixed point.

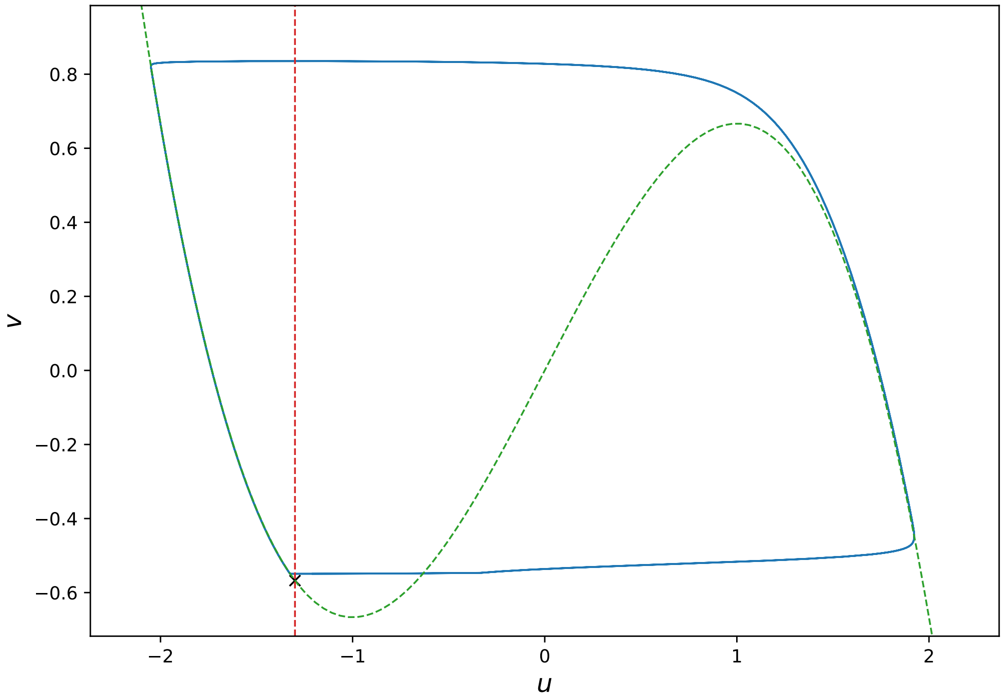

Figure 1.3: Phase space plot for the FHN system in the excitable state ($a = 1.3$, $\varepsilon = 0.01$). The dashed lines are respectively the u (green) and v (red) nullclines. The × marks the global fixed point. The spike is initiated via a square pulse input.

system is displaced towards positive u values. Depending on the magnitude of the shock, two outcomes are possible.

If the pulse is subthreshold, the system is recaptured by the refractory branch and gradually moves back towards the fixed point. Conversely, if the pulse exceeds the threshold, the system jumps to the active branch, follows it up to the maximum at $u = 1$, and then returns to the refractory branch, resuming its trajectory toward the fixed point. This behavior is referred to as a *quasi-threshold* effect because the critical value for spike generation depends on both the pulse duration and shape. As a result, there is no universal threshold, only one that applies to a fixed pulse duration and shape.

By analyzing the phase plane and conducting numerical experiments, we can further refine our understanding of the phenomenology of spike production. Evaluating the time derivative of u between the branches of the cubic nullcline reveals that the central branch is repulsive along the u axis. Moreover, simulations show that as the pulse amplitude is varied while keeping its duration and shape fixed, action potentials are consistently generated when the pulse displaces the system across the central nullcline branch. Nevertheless, in some cases where the system crosses the nullcline, no spike is produced. Therefore, while such a statement cannot be made in an absolute sense, the crossing of the central nullcline branch can be considered an approximate threshold for action potential generation.

This behaviour in the excitable state can be explained also by exploiting the explicit time scale difference between the two variables. We proceed along the lines of the original article [29]. The motion along variable u is of time scale ε, while that along variable v is of time scale 1. This allows us to consider, approximately, the motions along the two variables separately: the one along u can be considered to happen for constant v, the one along v can be considered to happen for a value of $u = u(v)$ that is a function of the coordinate v. Let's first consider the motion along u, which is governed by the equation

$$\varepsilon \dot{u} = u - \frac{u^3}{3} - \bar{v} \tag{1.7}$$

where $\bar{v}$ is the value of v that we consider to be fixed for evolution times of order ε. Equation (1.7) has three equilibria for $|\bar{v}| < \frac{2}{3}$, one for $|\bar{v}| > \frac{2}{3}$ and two in the limiting cases $|\bar{v}| = \frac{2}{3}$. The type of equilibrium at the fixed points depends on the u-nullcline branch on which they lay, Figure 1.4. For $|\bar{v}| < \frac{2}{3}$, the two outermost equilibria are attractive, while the one lying on the central branch is repulsive, for $|\bar{v}| > \frac{2}{3}$, the only equilibrium is attractive, and in the limiting cases we have one attractive point and a saddle node. With these considerations in mind, we can describe the generation of action potential-like spikes as follows.

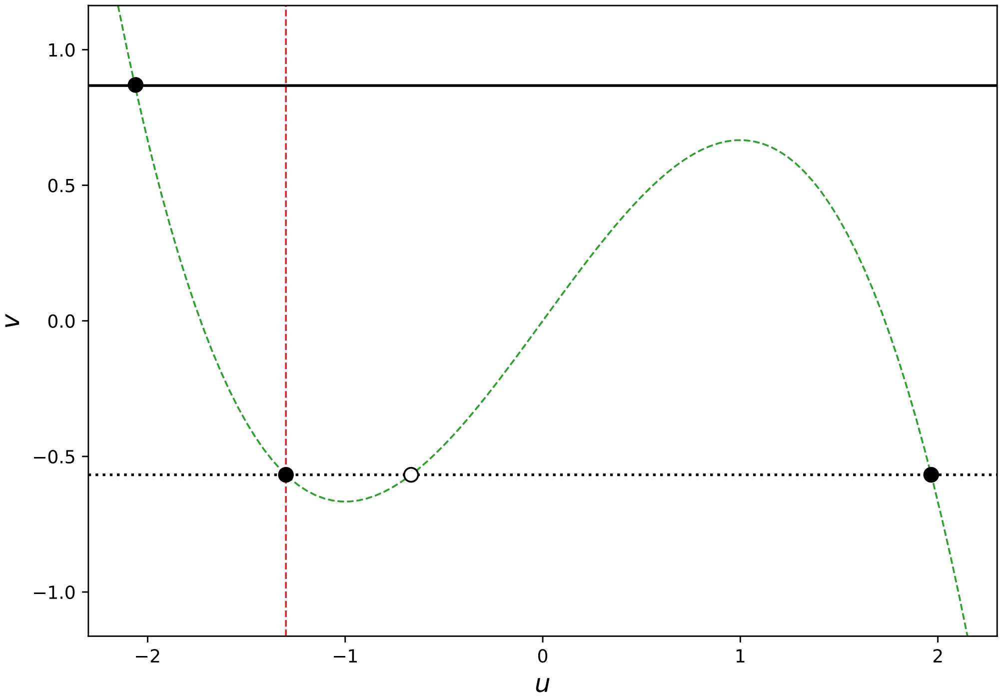

Figure 1.4: One-dimensional configuration space for the u variable for different values of v. Dotted line: $|v| < \frac{2}{3}$, two stable and one unstable fixed point. Solid line: $|v| > \frac{2}{3}$, single stable fixed point.

Consider a quiescent neuron, modeled by a FitzHugh-Nagumo system, situated near the global dynamic equilibrium point (u^*, v^*). Since we are working within the excitable regime, we can take this point to lie on the left branch of the u-nullcline without loss of generality. The one-dimensional phase space of the ε time scale dynamics resembles that depicted by the dotted line in Figure 1.4, where the global fixed point corresponds to the left-most equilibrium in the reduced dynamics. Let us now apply a Dirac delta function pulse to force the system in the direction of positive u. Depending on the magnitude of the pulse, two outcomes are possible: the system may either stop before reaching the unstable fixed point or jump across it, in the former scenario, the system is repelled back towards the initial equilibrium point, while in the latter, it is repelled towards the stable equilibrium point on the right branch of the nullcline, thus completing the firing event. Once the system reaches the right-most equilibrium, the u variable remains near this position while the v variable increases, as the term $u + a > 0$ is positive in the governing equation

$$\dot{v} = u + a, \tag{1.8}$$

where since we are now considering the dynamics of time scale 1, we can take u to approximately be given by the right-branch solution of equation

$$v = u - \frac{u^3}{3} \tag{1.9}$$

therefore, as v grows, u approximately follows the right nullcline branch. As v increases, it eventually crosses the threshold at $v = \frac{2}{3}$. Beyond this point, the ε time scale dynamics along u changes abruptly as the fixed points on the right and central nullcline branch coalesce in a saddle point transition, leaving a single fixed point on the left branch of the u-nullcline, corresponding to the phase space illustrated by the continuous black line in Figure (1.4). Becaus of this, the ε dynamics quickly drives the system toward the left branch. Once the nullcline is reached, the dynamics of time scale 1 resumes, this time in a downward direction, as one has $u + a < 0$. As the system moves along the left branch of the nullcline, it approaches the global dynamics fixed point, thereby re-entering a quiescent state, awaiting further stimuli. If we look at a time series of the system trajectory in Figure 1.5, we observe that the excursion of the u variable has produced an action potential-like spike, followed by a refractory period during which u gradually returns to the fixed point. Additionally, we note that the v time series exhibits maxima immediately after the action potential peaks, after which it slowly decreases back to its fixed point value. This behaviour highlights its role as a recovery variable associated with the neuron's refractoriness, which is maximal right after the action potential production.

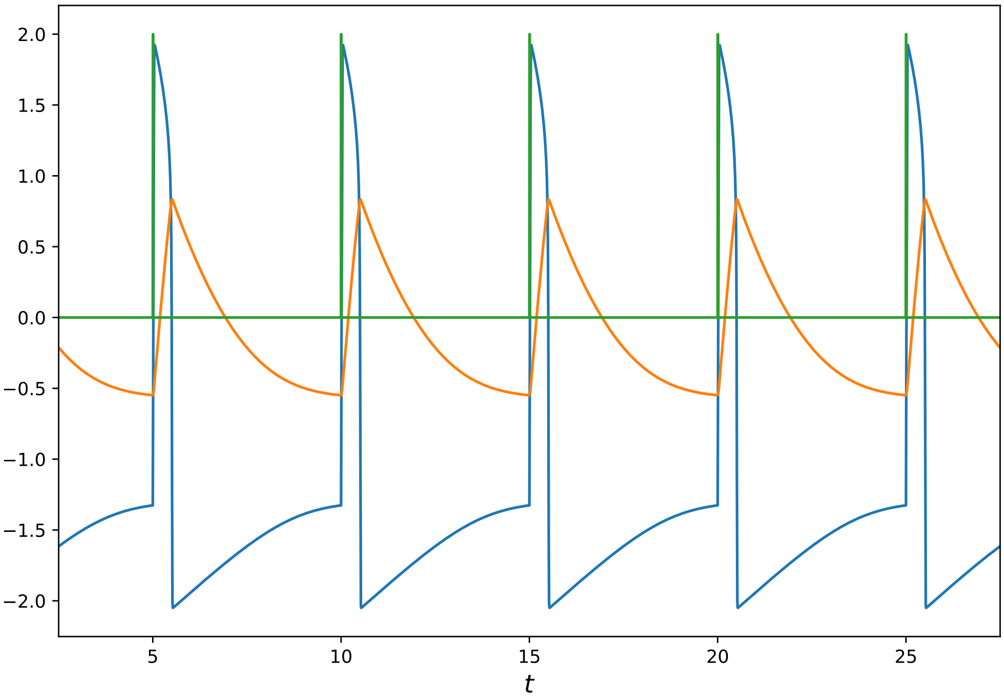

Figure 1.5: Time series of the dynamical variables, u in blue and v in orange, for an excitable FitzHugh-Nagumo system $\varepsilon = 0.01$, $a = 1.3$). The external stimulus, the green line, is a square wave pulse of amplitude 2, and of duration 10^{-3} time units, applied periodically each 5 time units.

2 | Equivalence of stationary solutions between a directed chain of neurons and a Delay Differential Equation

2.1 | Introduction

Complex networks theory has been mainly focused on understanding the topological structure of networks, often neglecting the dynamical properties of the interactions represented by the structure itself [72]. Diffusion processes on networks have been considered to study the relationship between the spectral properties of the Laplacian matrix associated to a network structure and the corresponding dynamical properties of the random walks stochastic dynamics in the relaxation process toward a stationary state [88]. Recently Boccaletti and collaborators [10] have extended the study of synchronization phenomena of network-coupled dynamical systems to the cascade of events that leads to the onset of global synchrony, highlighting how the network structure affects the dynamical path to macroscopic synchronized states. The considered models are an ensemble of N identical dynamical systems coupled by a network structure

$$\dot{x}_n = f(x_n) - J \sum_{m=1}^{N} \mathscr{L}_{nm} g(x_m) \qquad n = 1, \dots, N \tag{2.1}$$

where $x_n \in \mathbb{R}^d$ is the dynamical state of the n node that evolves according to the vector field $f(x)$ and $\mathscr{L}$ is a Laplacian matrix ($\sum_m \mathscr{L}_{nm} = 0$) describing the interaction among the nodes through the output function $g(x)$. The synchronous state $x_m(t) = y(t)$ is an equilibrium state of the system (2.1) where $y(t)$ is an orbit of the unperturbed system for $J = 0$. The matrix $\mathscr{L}_{nm}$ introduces a self-feedback dissipative effect ($\mathscr{L}_{nn} \neq 0$) so that the interaction depends on the differences in the dynamical state between different nodes. If the matrix

$\mathscr{L}$ is symmetric, all the eigenvalues are positive real, so that the synchronized state is stable. In particular, if the single node dynamics has a stable fixed point $y(t) = y_0$, the solution $x_n = y_0$ is a global stable solution of the system and we have a particular case of synchronized state corresponding to all nodes resting at the fixed point, and if the system $\dot{y} = f(y)$ has a periodic attractive solution, the equilibrium state corresponds to a synchronous oscillation of all the nodes with the same phase. In this framework the main problems are the study of the robustness of stable synchronized states, and the study of the relationships between the relaxation process, the spectral properties of the interaction matrix and the effect of stochastic perturbations.

From a statistical mechanics point of view, a symmetric character of the matrix $\mathscr{L}$ implies that the detailed balance (DB) condition [88] is satisfied for the stationary states and each node is in equilibrium with the environment, represented by the other nodes. In such a case, a local fluctuation of a node's state spreads in the network with a delay that depends on the local dynamics without any current density in the diffusion process. However the applications of complex network theory [28] to physical systems like neural networks [4], epidemic spread [74] and traffic dynamics [89], have pointed out that the Laplacian matrix associated to real networks do not satisfy the DB condition for the existence of a physical equilibrium, mainly due an intrinsically directed nature of the couplings. In such cases the diffusion processes on the network relax towards non-equilibrium stationary states (NESS), in which stationary currents persist in the system. The NESS are usually studied in the framework of Markov processes, in particular random walks on graphs, modeled by a master equation where the transition rate matrix is in turn built from the original network interaction structure. The existence of currents in the stationary states is strictly related to the cycle space of the graph, since we have as many independent currents as the cardinality of the cycle base, a fact that reflects the stochastic non reversibility of the microscopic dynamics. When each node is associated to a dynamical system, the relationship between the interaction structure and the existence of attractive global dynamical states has to be studied. If the single node dynamics has an attractive fixed point and the interaction structure is dictated by a Laplacian matrix, we always have a constant global solution. But simulations [70] suggest the existence of periodic stationary solutions, whose appearance can be related to a phase transitions of the system[49] as the result of bifurcation phenomena in phase space. A relevant observation highlighted by the numerical simulations is that the bifurcation phenomena can be explained by a low dimensional system even if the number of degrees of freedom is very large. We conjecture that the existence of stationary currents in the stationary state of a master equation could be related with the existence of a bifurcation phenomenon that breaks the symmetry of the synchronized solution in networked

dynamical systems, creating a traveling stationary wave in the system.
In the case of dynamical neural networks, the existence of cycles could induce feedback processes that create a self-consistent stable periodic solutions whose existence depends both on the interaction structure (i.e. the link weights) and on the dynamics on the single nodes. In this chapter we address the problem of the existence of periodic stable stationary states for an ensemble of FitzHugh-Nagumo (FHN) neurons coupled through a directed cycle when the single neuron dynamics has a single equilibrium point. This is the fundamental building block to understand how the graph geometry affects the global dynamics, thus we perform extensive numerical simulations to study the dependence of the solution on the model parameter. The directed character of the graph implies an asymmetric interaction among the nodes and the corresponding Laplacian matrix has a complex spectrum, which is a fingerprint of the non-reversible character of the Markov process associated to the network. The single node neuron model has an attractive equilibrium state so that the synchronized solution for the system corresponds to all the neurons at the equilibrium state. If the coupling strength reaches a critical threshold, the simulations highlight the rise of a periodic solution that bifurcates into a stable and unstable solutions so that the equilibrium state remains stable. To characterize the periodic solution we use a self-consistent approach based on a delay differential equation (DDE) whose periodic solution corresponds to the stationary solution of the neural network. We numerically study the bifurcation phenomenon on the DDE that gives rise to the periodic solution to perform a quantitative comparison with the neural network dynamics. Due to the stiff character of the FHN dynamics, specific algorithms have to be used to integrate the DDE [35–37]. The study of the existence of periodic solutions to DDEs has been considered [98] as model for systems exhibiting temporal dissipative solitons. We propose to interpret the solution described in the following as a spatial self-consistent wave on network-coupled interacting FitzHugh-Nagumo systems, whenever the interaction network exhibits cycles.

2.2 | The coupled FitzHugh-Nagumo oscillators model

We have explicitly considered the case of interacting FHN neurons as a relevant example of dynamical systems on a graph due to possible applications in neuroscience, as the solution of dynamical neural networks could highlight some relevant phenomena that would allow a better understanding of the dynamics of biological networks. In a general case, we consider an ensemble of interacting FHN neurons according to the equations

$$\begin{aligned}\varepsilon\dot{u}_n &= u_n - \frac{u_n^3}{3} - v_n + J\sum_m (w_{nm}u_m - w_{mn}u_n) \\ \dot{v}_n &= u_n + a\end{aligned} \tag{2.2}$$

where $w_{nm} > 0$, the link weights, defines the interaction network and quantify the effect of the state of neuron m on neuron n. We recall the u_n represents the cell potential of the n-th neuron and v_n a recovery variable, in principle representing several other internal variables. The parameter J defines the coupling strength of the neural network. The sum

$$I_n^i(t) = J\sum_m w_{nm}u_m(t)$$

is the input signal from the other neurons whereas

$$I_n^o(t) = J\sum_m w_{mn}u_n(t) = w_n u_n(t)$$

is the total output signal that introduces a dissipative effect in the neuron dynamics. Being interested in studying the role of fluctuations among the neuron states we assume the Laplacian condition for the weights

$$\sum_m w_{nm} = w_n \tag{2.3}$$

which means that the synchronized state $(u_n(t), v_n(t)) = (u(t), v(t))$ has to be a solution of the single neuron dynamics. The parameter a is chosen so that the single node dynamics has a single stable fixed point in phase space and the synchronized solution reduces to the equilibrium position (u^*, v^*) (see (2.7)). Our aim is study the existence of stationary attractive solutions $u_n^\infty(t)$ of the system (2.2)

$$u_n^\infty(t) = \lim_{T\to\infty} u_n(t+T) \tag{2.4}$$

given an initial condition. A mean field approach would provide

$$\begin{aligned}\frac{\varepsilon}{N}\sum_n \dot{u}_n &= \frac{1}{N}\sum_n\left(u_n - \frac{u_n^3}{3} - v_n\right) \\ \frac{1}{N}\sum_n \dot{v}_n &= \frac{1}{N}\sum_n u_n + a\end{aligned} \tag{2.5}$$

and, if it is possible to neglect local fluctuations, one recovers for the average network activity $U(t) = \sum_n u_n(t)/N$ the single neuron dynamics. When one considers directed graphs ($w_{nm} \neq 0 \Rightarrow w_{mn} = 0$), the mean field approximation cannot describe the signal propagation observed in neuron networks since the presence of feedback effects due to loops in the network can create new stationary global solutions that are not solutions of the averaged equation (2.5). Due to the algebraic relevance of loops in the structure of graphs and their physiological role as origins of feedback, these stationary solutions may be related to the emergence of memory mechanisms in brain structures. To study the existence of such solutions we consider a simplified model where N FHN neurons interact by a directed loop and the general network-coupled system (2.2) reduces to

$$\begin{aligned} \varepsilon \dot{u}_n &= u_n - \frac{u_n^3}{3} - v_n + J\,(u_{n-1} - u_n) \\ \dot{v}_n &= u_n + a \end{aligned} \tag{2.6}$$

where once the network is fixed the only free parameter is the excitatory coupling strength $J > 0$ and we identify site $N + 1$ and site 1 imposing a periodic boundary condition, see Fig. 2.1 for a schematic representation. We choose the parameter value $|a| > 1$ so that the equilibrium solution of the FHN oscillator

$$u^* = -a \qquad v^* = \frac{a^3}{3} - a \tag{2.7}$$

is a stable equilibrium for the whole system (2.6) and the single-node FHN system does not admit any other solutions. We recall that in the case $|a| < 1$ the single neuron exhibits a stable limit cycle, which for an undirected network implies the existence of a synchronized solution $u_n(t) = u(t)$ for all n (i.e. all the neurons move in a synchronous way on the limit cycle of the FHN oscillator) whose stability depending on the strength of the coupling J [76]. Indeed the single neuron dynamics undergoes a supercritical Andronov-Hopf bifurcation at $|a| = 1$ and a stable limit cycle appears in the single node dynamics, contextually to a loss of stability of the global fixed point. On the other hand, in the considered case $|a| < 1$ the only global equilibrium is the fixed point (2.7) that is stable, so that the existence of a non-trivial stationary solution (2.4) has to be the result of a global bifurcation of different nature that does not affect the fixed point stability.

In the case $\varepsilon \ll 1$ the system (2.6) has a stiff character, since the variables u_n and v_n evolve respectively on a fast timescale and a slow timescale. The fast timescale ε can be viewed as the reaction timescale of the neuron, i.e. the order of magnitude for the time it takes for a neuron to reach the peak of its action potential after receiving a triggering signal, whereas the slow time scale of order $\mathcal{O}\,(1)$ is the relaxation time scale to the single neuron equilibrium state.

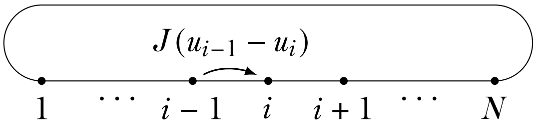

Figure 2.1: Schematic representation of the neuron ring.

Noticeably the limit $\varepsilon \longrightarrow 0$ is singular and we loose the regularity of the solutions at $\varepsilon = 0$, since for the equation becomes a differential-algebraic equation, however it is possible that the limit solution still exist despite loosing continuity. This problem therefore belongs to the class of singularly perturbed problems, and the numerical integration has to cope with the intrinsic stiffness of the system (2.6).

We address the existence problem of stable stationary solutions for a feed-forward loop of neurons which do not change the stability of the fixed point (2.7) (i.e. the physiological resting state of the neural network) by looking for a self-consistent solution

$$\begin{aligned} u_n(t) &= u\,(t - n\delta) \\ v_n(t) &= v\,(t - n\delta)\,, \end{aligned} \tag{2.8}$$

that corresponds to a wave propagating in the direction of increasing site number. The time interval δ is the time displacement between two consecutive neurons and it depends on the neuron dynamics. To obtain the relationship between δ and the other parameters, one should in principle study the equation

$$\begin{aligned} \varepsilon \dot{u} &= u - \frac{u^3}{3} - v + J\,(u(t+\delta) - u(t)) \\ \dot{v} &= u + a, \end{aligned} \tag{2.9}$$

with periodic boundary conditions $u(t+T) = u(t)$ and $v(t+T) = v(t)$ and $T = N\delta$ as the period. The bifurcations of (2.9) correspond to the bifurcations of a traveling wave solution to the full ring of excitable neurons, and could be obtained in principle by using a perturbation approach on the δ parameter, that has to be computed in a self-consistent way. On the other hand, since from simulations (see Sec. 2.3) we observe that δ cannot be made arbitrarily small, so the condition $\delta \ll 1$ that would justify a perturbative approach is not satisfied. A direct numerical solution of (2.9) is complicated by its advanced character and we use the periodic boundary condition to get a delay differential equation. Letting

$$\tau = T - \delta = T\frac{N-1}{N}, \tag{2.10}$$

the existence of a stationary periodic solution to (2.6), and equivalently to (2.9), corresponds to a solution of a delayed differential equation (DDE)

$$
\begin{aligned}
\varepsilon\dot{u} &= u - \frac{u^3}{3} - v + J(u_\tau - u) \\
\dot{v} &= u + a,
\end{aligned}
\tag{2.11}
$$

where $u_\tau = u(t-\tau)$ and τ is the positive delay defined in (2.10). We shall see that the limit $N \longrightarrow \infty$ corresponds to $T \longrightarrow \infty$ and $\delta = T/N$ remains finite so that the stationary solutions tend to a soliton wave in the system (2.6).

A stationary state of period T for (2.6) is a solution of the DDE with τ given by (2.10), but, since no specific boundary condition is required in the solution of (2.11), we cope with the problem of the existence of periodic solutions of the DDE for a delay τ when the coupling parameter J overcomes a critical threshold for a given ϵ. For $|a| > 1$ the fixed point (2.7) is a stable solution of (2.11). Using a heuristic argument, one observes that for $J = 0$ the dynamics is dissipative in the whole phase space, but the FHN system is able to create an orbit that follows the stable branch of the nullcline and relaxes to the fixed point, when the resting state is perturbed in a suitable way. If the perturbation is applied at a given position along the nullcline near the resting state we can create a periodic orbit with arbitrarily long periods T. The pertubation amplitude compensates the dissipation of the dynamics, but the average dissipation along the orbit depends inversely on the period T. If the average dissipation is small (i.e. $|a| - 1 \ll 1$) and the parameter J is sufficiently large, the delayed term $J(u_\tau - u)$ can induce a bifurcation in the phase space acting as continuous perturbation, thus creating a stable and an unstable periodic orbit. If $T - \tau = \delta$ is weakly dependent on the period, the study of this bifurcation phenomenon in the DDE varying τ implies the existence of stationary state for the neuron loop (2.6) when $T/\delta = N$ is integer. From the previous formulation of the problem, both the single system dynamical parameters a, ε and the coupling strength J will be the same across the two systems, whereas the relationship between the delay time τ and N is given by eq. (2.10). The dependence of the periodic solution on the coupling parameter J has to be the same for both cases.

The correspondence between the periodic solutions of the systems (2.6) and (2.11) only refers to the solutions admissibility, their stability and the measure of eventual attraction basins remains to be established.

We finally remark that the existence of a self-consistent wave solution is a consequence of the discrete character of the system and we shall see that we can obtain one with a finite period only for finite N.

2.2.1 | Stability problem of the stationary solution

The solution of the stability problem for the self-consistent wave solution $u_n(t) = u(t - \delta n),\ v_n(t) = v(t - \delta n)$ requires to study the linearized system

$$\begin{aligned} \varepsilon \delta \dot{u}_n &= \left(1 - u^2(t - Tn/N)\right) \delta u_n - \delta v_n + J\,(\delta u_{n-1} - \delta u_n) \\ \delta \dot{v}_n &= \delta u_n, \end{aligned} \tag{2.12}$$

where $(\delta u_n, \delta v_n)$ are small perturbations to the wave solution. Due to the periodic dependence on T one can consider the Poincaré matrix of the system and study its spectral properties. The stability property requires that for any choice of the perturbation the linearized system has all eigenvalues with a negative real part, so that the critical values of the parameters correspond to the existence of an imaginary eigenvalue. If one considers (2.11) linearized at the periodic solution $u(t),\ v(t)$, the equation for the periodic orbit's stability is obtained, in the form

$$\begin{aligned} \varepsilon \delta \dot{u} &= \left(1 - u^2(t)\right) \delta u - \delta v + J(\delta u_\tau - \delta u) \\ \delta \dot{v} &= \delta u, \end{aligned} \tag{2.13}$$

and the periodicity of the solution to (2.11) allows us to look for a solution in Floquet form

$$\delta u = e^{\lambda t} \delta \bar{u}(t), \qquad \delta v = e^{\lambda t} \delta \bar{v}(t),$$

where $\lambda \in \mathbb{C}$ is the Floquet exponent, corresponding to the Lyapunov exponent of the Poincaré map, and $\delta \bar{u}(t),\ \delta \bar{v}(t)$ is periodic with period T. Inserting this form in (2.13) we get

$$\begin{aligned} \varepsilon \delta \dot{\bar{u}} &= -\lambda \delta \bar{u} + \left(1 - u^2(t)\right) \delta \bar{u} - \delta \bar{v} + J(e^{-\lambda \tau} \delta \bar{u}_\tau - \delta \bar{u}) \\ \delta \dot{\bar{v}} &= -\lambda \delta \bar{v} + \delta \bar{u}. \end{aligned} \tag{2.14}$$

These solutions correspond to the eigenvectors of the Poincaré matrix computed at a given section $t_s \in [0, T]$ with λ their associated eigenvalue. By construction we have

$$\delta \bar{u}(t - \tau) = \delta \bar{u}(t + T/N), \qquad \delta \bar{v}(t - \tau) = \delta \bar{v}(t + T/N)$$

and if we set

$$\begin{aligned} \delta u_n(t) &= e^{\lambda t} \delta \bar{u}(t - Tn/N) \\ \delta v_n(t) &= e^{\lambda t} \delta \bar{v}(t - Tn/N) \end{aligned} \tag{2.15}$$

we get a solution for the system (2.12). Therefore, if (2.14) admits a periodic solution $\delta \bar{u}(t)$ with $\Re(\lambda) > 0$ we have instability for the self-consistent wave solution of the initial system (2.6). Since the stability of the origin of the Poincaré matrix implies linear stability for the self-consistent wave, the study of the periodic solutions of (2.14) when λ varies allows to solve the stability problem, in an approach reminiscent of the Master Stability Function framework, developed for the synchronization of dynamical systems [75].

2.3 | Numerical simulations results

We have studied the relationship between the system (2.6) and the DDE (2.11) by performing extensive numerical simulations. This approach has been preferred since due to the combination of stiff, delayed and nonlinear character of the system an analytical study of the parameter dependence and of the stability properties of solutions is highly not trivial.

2.3.1 | Chain solution dependence on the parameter values

We explore the dependence of the wave solution features on the parameters, in particular the number of neurons N and the coupling strength J. To gain some insight into the character of the self-consistent solutions we study the dependence of the wave speed on the coupling strength J for several values of size N. Since no explicit length scale can be identified in the model, we identify the wave speed as the inverse of the period, i.e. we fix without loss of generality the length of the chain to unit. The simulation results are collected in Fig. 2.2. Each of the selected system sizes displays the same value for the lower threshold of the coupling, below which no stable wave solution exists. Repeating simulations with several other values of N, the critical coupling value of $J \approx 0.05$ appears to remain the same independently of the selected system size. Above the critical value all the speeds start by growing concavely in function of the coupling and later settle into a roughly linear growth regime. An interesting feature of the system is the disappearance of the wave solution for too large values of J. This is clearly visible in the $N = 100$ and $N = 325$ plots of Fig. 2.2, but has been verified to happen, at larger values of J, for the other values of N as well. By looking at the velocity in units of sites per unit time in panel B of the Figure, we observe that at larger values of J the growth approaches a linear trend, of slope apparently common among the various chain size values, despite the presence of an offset which does not allow for a full superimposition. Performing a linear fit on the trend for each value of chain size we obtain the coefficients reported in Table 2.1.

In Fig. 2.3 we plot the dependence of the period T of the ring wave solution on the coupling strength J in a log-log scale, where we can see that as N grows larger and for the greater values of J the trend generally adapts to a

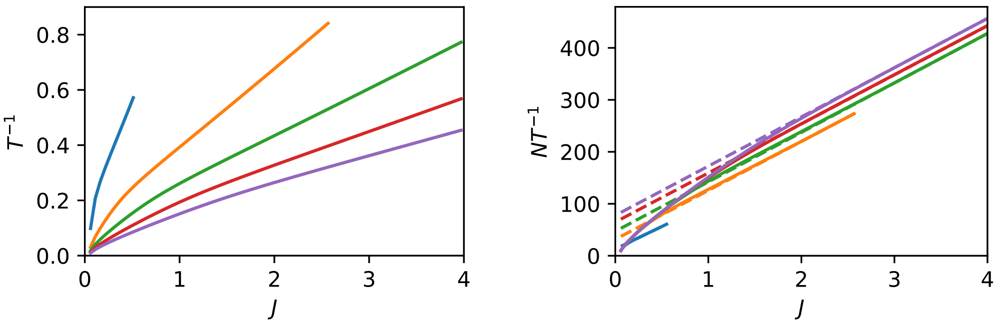

(A)

(B)

FIGURE 2.2: Panel A: self-consistent periodic wave speed as a function of J for several values of the chain size N. From top to bottom $N = 100$ (blue), 325 (orange) , 550 (green), 725 (red), 1000 (purple). Panel B: the same quantity multiplied by the chain size N. From bottom to top $N = 100$ (blue), 325 (orange) , 550 (green), 725 (red), 1000 (purple). The dashed lines mark the linear fits performed on the final 25% of the curve for each value of chain size. In both panels the interruption on the right end of the two lines $N = 100$ and $N = 325$ marks the disappearance of the wave solution.

power law. A power law fit to the tail of the plot for $N = 1000$, reproduced in Fig. 2.4, yields an exponent ≈ -0.84 pointing out the reasonable existence of some finer underlying trend with respect to the apparently linear growth observed in Fig. 2.2. To interpret these findings we propose the following picture. The lower coupling threshold is a consequence of the nonlinear nature of the system: J plays the role of magnification/attenuation factor for the preceding neuron signal, and as a consequence of the choice of the coupling increments the linear dissipation by an extra Ju_n. In this context the lower critical value of J can be interpreted as the minimal scaling which a spike from a FHN neuron can undergo, while still eliciting a spike in an identical unit, provided that an extra Ju_n dissipation is added to the driven unit. In light of this interpretation, also the linear trends in Fig.2.2 can be motivated. Indeed if we assume that existence of the wave solution for a given J requires that input from each preceding neuron rises to a sufficiently high level in a sufficiently short time to produce a spike in its following neuron, doubling the value of J will intuitively have the effect of halving the time it takes to reach said critical value. Since the timescale of the fast dynamics is ε we expect that analogous phenomena can take place when the latter is varied. From this discussion, and in the absence of scaling w.r.t. N in the coupling, it is apparent that the existence of

N	slope	intercept
100	86.67 ± 0.08	12.87 ± 0.04
325	94.18 ± 0.03	31.55 ± 0.06
550	95.15 ± 0.02	47.06 ± 0.06
725	94.49 ± 0.02	64.76 ± 0.04
1000	94.75 ± 0.01	77.64 ± 0.02

TABLE 2.1: Values for the slopes and intercepts of the linear fits to the plots in Fig. 2.2B. The average slope value is 93 ± 3, where the uncertainty is attributed as the standard deviation of the sample.

self-sustained site to site transmission of the neural pulse is a matter that entirely depends on the satisfaction of local requirements at each of the links, but does not depend on any global coordination effect in the solution. On the other hand, the disappearance of the wave solution for high values of the coupling can be justified by considering the increasing trend of the wave speed w.r.t. J, such that at some point the wave is too fast, and travels all the way around the ring, trying to excite neurons which are still in a refractory phase, i.e. too far from the fixed point to be displaced across the central nullcline branch by the spike of an identical neuron, so that a spike cannot be elicited self-sustainedly any longer, and the wave disappears. This picture could also explain how longer chains can attain larger speeds before the solution disappears when w.r.t. to shorter ones, even though at the same coupling value they always admit slower waves in comparison, the proposed reason being that due to the lack of a natural spatial scale in the system, in chains with more sites the wave can reach higher speeds without colliding with refractory neurons which cannot be excited yet. A relevant feature of the discussed self-consistent periodic wave is that throughout its existence the stable fixed point of the system remains such, as it would be expected with a directed Laplacian coupling, so that the observed phase transition cannot be regarded as an Andronov-Hopf bifurcation of the fixed point.

2.3.2 | Delay Differential Equation solution dependence on the parameter values

In this paragraph we study the properties of limit cycle solution to the DDE (2.11), versus the choice of parameters of the system J and τ. In particular we are interested in the existence of a sharp transition between a quiescent neuron, and a fully active and continuously spiking one. To study these properties we

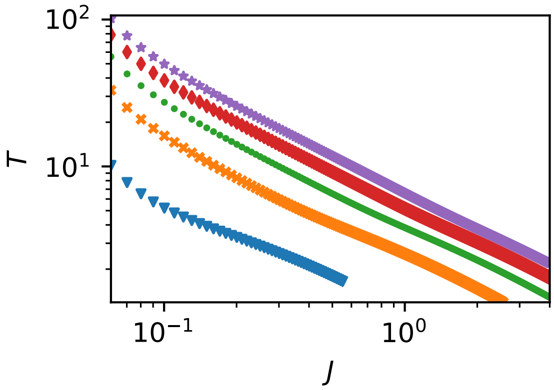

FIGURE 2.3: Dependence of the period T of the ring solution on the coupling J for several values of N in a log-log scale. The interruption of the $N = 100$ and $N = 325$ series on the right hand side of the plot indicates disappearance of the wave solution. The values of N with the corresponding symbols are 100 blue triangles, 325 orange crosses, 550 green dots, 725 red diamonds and 1000 purple stars.

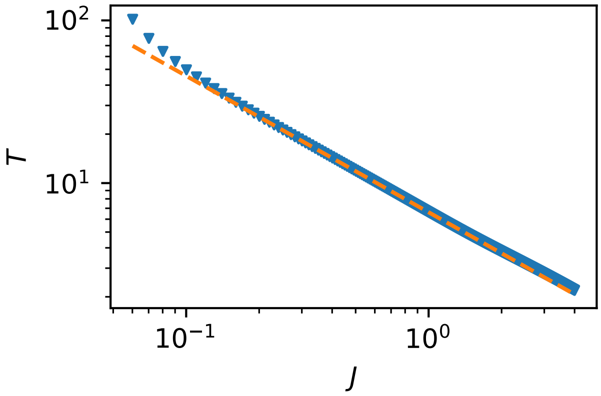

FIGURE 2.4: Dependence of the period T on the coupling J for a chain of $N = 1000$ sites. The dashed line is a power law fit, with an exponent ≈ -0.84.

simulate the system many times, varying $J \in [0.2, 2]$ and $\tau \in [0.5, 2]$ and calculate the area of the limit cycle that appears in the system, when it exists. In delayed systems the initial condition must be supplied as a function over the interval $[-\tau, 0]$ so to have a defined value for the delay term during the first τ of integration. Our choice for the initial condition is

$$\begin{aligned} \varphi_u(t) &= -a + \frac{1}{\sqrt{2\pi}\sigma} e^{-(t-\tau/2)^2/2\sigma^2} \\ \varphi_v(t) &= -a + a^3/3 \end{aligned} \tag{2.16}$$

which amounts to starting the system in its fixed point and providing a Gaussian stimulus in the fast variable. The value of choice for the width parameter has been set to $\sigma = 10^{-1}$. The results of this simulation are collected in Fig. 2.5. For any fixed J we observe that there exists a minimal value of τ below which the limit cycle is not created, and above which the cycle sharply appears, and a similar picture appears if we fix τ, highlighting the existence of a minimal critical J. Moreover we observe an increasing trend of the limit cycle area in function of the delay for a fixed J, and an analogous increasing trend versus J for a fixed τ. The properties of the solution for delayed systems can in principle depend strongly on the initial condition, due to the infinite dimensionality of the problem. To assess how much the properties of the initial spike influence the solution we change normalization of the initial spike and parametrize it as follows

$$\begin{aligned} \varphi_u(t) &= -a + Ae^{-(t-\tau/2)^2/2\sigma^2} \\ \varphi_v(t) &= -a + a^3/3 \end{aligned} \tag{2.17}$$

so that we can act independently on its width σ and amplitude A. As in the previous case, for each simulation we measure the value of the limit cycle area, when one is created. We perform also in this case extensive simulations, the results of which are collected in Fig. 2.6. The emerging picture is that both for A and σ there exist optimal values, for which the value of the other parameter becomes unimportant. Our interpretation for the optimal value of A is that it is the value for which the system starts out optimally displaced across the central nullcline, far enough from the fixed point to elicit a spike, but not too far, where the dissipative component of the dynamics would be dominant. Indeed, since the selected value for the delay is $\tau = 1$, as σ grows closer to 1 we are merely giving the system a nearly constant input, but we are still able to reach the limit cycle. We also observe the existence of a minimal σ value, which reasonably is the minimal duration that a pulse must have in order to generate a response in the system. On the other hand, for the optimal $\sigma \approx 0.1$ range, the proposed explanation is that in this interval we are feeding the system with pulses of a

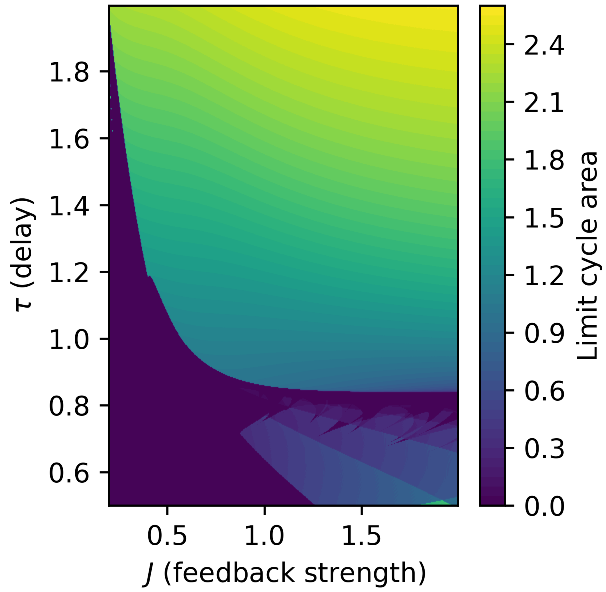

Figure 2.5: Phase diagram for the Delay Differential equation (2.11). The colour scale indicates the area of the limit cycle. In the lower right corner of the heatmap, the colour seems to suggest the existence of a limit cycle, but is in fact an artifact due to long transients before relaxation to the fixed point. The parametrization used for the initial spike is the one of Eq. (2.16).

similar duration to those that will appear in the limit cycle, in a sense putting it in closer proximity to it w.r.t. other initial condition choices. In this context as well, we observe a minimal A value below which, despite the optimality of the pulse shape, the input is too low to cause any activity in the system. In addition to these findings, we observe that whenever the limit cycle exists, there is hardly any dependence of the actual value of the area on the system parameters. As it is in the chain, the stable fixed point of the system (u^*, v^*) is not destabilized by the appearance of the limit cycle, so that an Andronov-Hopf bifurcation can be ruled out in this case as well.

2.3.3 | Correspondence of the solutions

We compare numerically the self-consistent periodic solutions for the loop of neurons with those of the single delay differential equation (2.11). To do so we fix a number of neurons N and check with a simulation for the existence of a stable periodic solution of the system (2.6). If it exists we calculate its period T

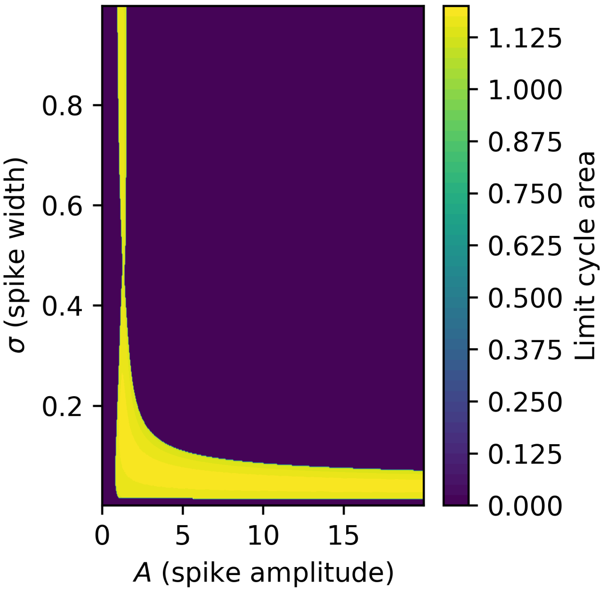

Figure 2.6: Area of the limit cycle in function of the amplitude A and width σ of the initial pulse for equation (2.11) with $J = 1$ and $\tau = 1$.

by measuring the time interval between two consecutive crossings of a Poincaré section. Then the relation (2.10) determines the delay time τ to be inserted in eq. (2.11) to get the corresponding periodic solution. In Fig. 2.7 we show some examples of comparison between the continuous stable periodic solution of eq. (2.11) and the self-consistent periodic wave solution of the neuron ring defined by the neuron states at a given time.

We observe that the numerical solutions of the delay differential equation interpolate perfectly the periodic solutions of the FHN neuron loop when the parameters are varied, and that due to the stiffness of the problem most of the chain sites are on the nullclines of the system. We can also infer some qualitative aspects of the limit cycle dependence on the system parameters. Namely, raising the value of the coupling J makes the cycle thinner along the vertical axis, this is easily noticeable e.g. comparing insets a) and b) or c) and d) from Fig. 2.7. This observation suggests that in the context of the chain model the wave solution speed is a non-decreasing function of the coupling J, causing the system to close the cycle in shorter and shorter times as J is increased. Since changing the system size N at fixed T amounts to changing the delay τ in the DDE, it is easy to match the a) → c) or b) → d) trend with the one observed for fixed J in Fig. 2.5. Conversely, the apparently contrasting decreasing trend of

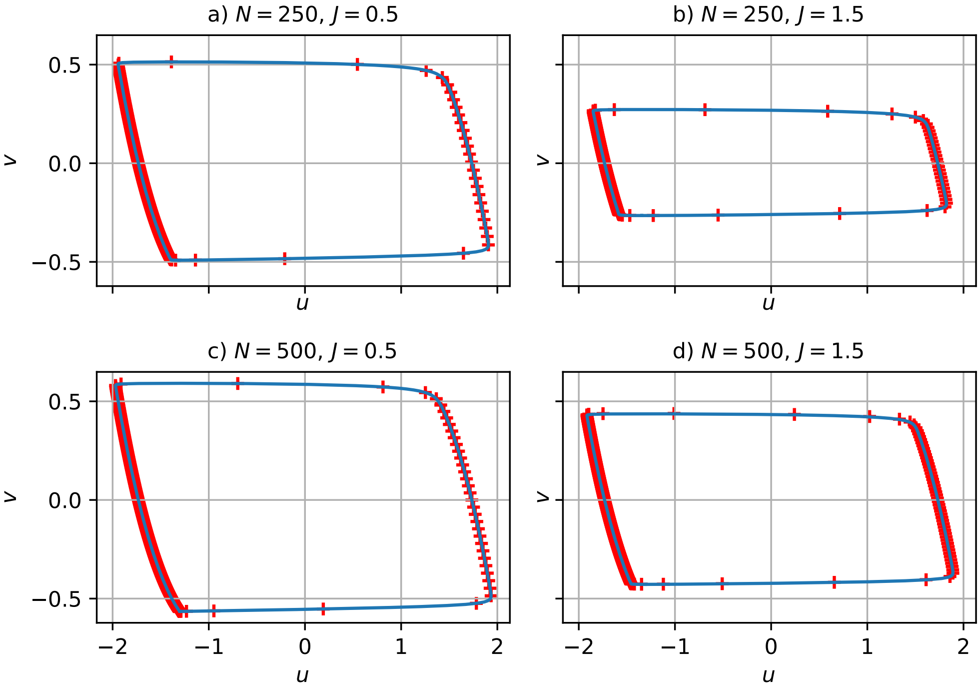

Figure 2.7: Examples of the limit cycles of the delayed equation (continuous blue line), and the chain sites (red crosses). Notice how the cycle area decreases with larger couplings and increases with the number of neurons in the chain.

the area from a) → b) or from c) → d) can be justified by remembering that when J is changed at fixed system size in the chain, the equivalent delay of the DDE is influenced as well, through the dependence of T on J, therefore in the phase diagram of Fig. 2.5 the equivalent displacement to an increase of J in the chain is a diagonal motion to the right and down. We use a Gaussian external stimulus for the delay differential equation and we let the system relax to the attractive periodic solution, when it exists. In both cases the periodic solution is a stable attractive state of the dynamics with a defined stability basin. The numerical integration of the delay differential equation has been performed using the RADAR5 [35–37] integration algorithm, which is specifically built to integrate delay differential equation with a stiffness character and even algebraic differential equations. In Table 2.2 we report the numerical values of the two sides of eq. (2.10) obtained for the values of the coupling J and N of Fig. 2.7, in these simulations the stiffness parameter ε is fixed at 10^{-2}. We observe a reasonable accord between the r.h.s. and the l.h.s. of Eq. (2.10) in the considered cases. The likely source of the small differences observed in some cases reasonably lies in the different attractivity of the solutions between the DDE and the unidirectional chain, i.e. in a different rate of convergence to the limit cycle in the two cases.

N	J	$T-\tau$	T/N
250	0.5	0.0134	0.0139
250	1.5	0.0057	0.0060
500	0.5	0.0125	0.0119
500	1.5	0.0053	0.0053

Table 2.2: Values of the phase difference between two consecutive chain sites and the corresponding gap between the DDE solution period and the delay. The value of τ used to compute the second quantity is the equivalent delay as calculated via eq. (2.10). All reported digits have been found to be stable across three orders of magnitude of tolerance of the integrator.

On both sides of Eq. (2.10) there is an implicit dependence, via T, on the coupling strength J, therefore we can check their scaling versus the coupling. In Fig. 2.8 we show the quantity T/N dependence on J, this amounts to the time it takes for the wave to travel from a site to the following one. We observe that all system sizes superimpose on each other for most of the plot, while for $N = 100$ and $N = 325$ we observe a deviation from the power law behaviour immediately before the disappearance of the wave solution. This can be interpreted as a slowdown of the wave due to the fact that its front is beginning to

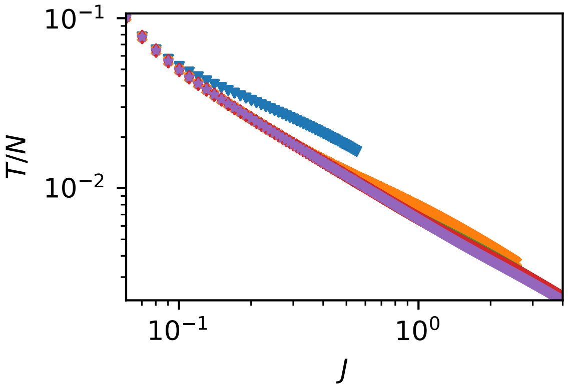

Figure 2.8: Dependence of the T/N site-to-site propagation delay on the coupling strength J for several values of chain size N. The values of N with the corresponding symbols are 100 blue triangles, 325 orange crosses, 550 green dots, 725 red diamonds and 1000 purple stars.

encounter neurons earlier and earlier into their refractory phase.

We proceed similarly for the Delay Differential Equation, this time fixing τ while varying J. In Fig. 2.9 we plot $T - \tau$, the analogous quantity to T/N for the delay system, which in this case can be interpreted as the advance of the delay w.r.t. the final period of the solution. Also in this case we observe a power law behaviour, this time with exponents ≈ -1.

2.3.4 | Stiffness Dependence

In the whole of the preceding part of the chapter we kept $\varepsilon = 10^{-2}$ fixed but in principle the properties of the self-consistent wave/limit cycle solution should depend on it, since it represents the reaction timescale of the system, setting the time of $\mathcal{O}(\varepsilon)$ that it takes for the system to jump from a nullcline to the other, and therefore to react whenever a sufficiently strong and sharp input is provided. From the discussion of paragraph 2.3.1 we expect that decreasing ε in the chain system (2.6) will have a similar effect on the global properties of the solution as increasing J. On a single node the two scalings remain distinguishable, as decreasing ε forces the single node dynamics to adhere more closely to the nullclines, while the J scaling has no such effect. Indeed we observed in simulations that depending on the size of the system, there exists an inferior critical ε below which the wave solution disappears in the same way as it does for too large J, i.e. by becoming too fast and colliding with neurons that

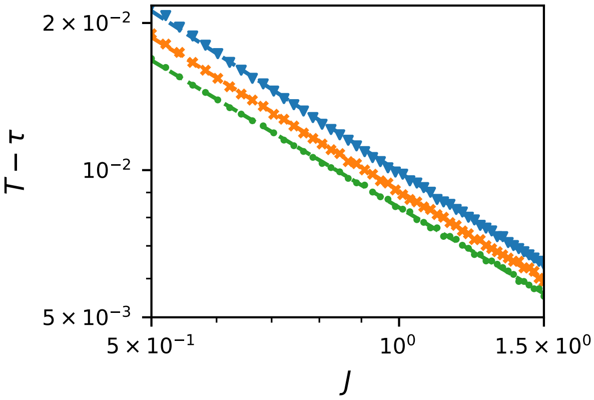

Figure 2.9: Dependence of the $T - \tau$ gap on the coupling strength J for several values of the delay τ. The values of τ with the corresponding symbols are 1 blue triangles, 1.5 orange crosses and 2 green dots. The dashed lines in corresponding colours are power law fits, all yielding an exponent ≈ -1.

are still too refractory. In accord with the picture proposed for J, the critical ε decreases when the size of the system is increased, as larger rings make it easier to accommodate faster waves. This behaviour is strikingly similar to what is observed in traffic models such as [69], where albeit originating from an explicit delay term, a too short reaction time causes the wave solution to destabilize and disappear. When studying the DDE, instead, we observe no disappearance of the solution for small $\varepsilon \approx 10^{-12}$. This property makes it easier to study the dependence e.g. of T on ε, and indeed we can study the l.h.s. of (2.10) $T - \tau$ at fixed τ and J by varying ε. We do so by performing extensive simulations, reported in Fig. 2.10. Consistently with what we expect, we observe a power law behaviour with a positive ≈ 1.14 exponent in function of ε.

2.4 | Conclusion

In this chapter we have discussed the properties of the traveling wave solutions that appear in directed loops of excitable dynamical systems, which mimic the properties of biological neurons. By means of extensive and accurate simulations, which were performed with methods suited to the intrinsic stiffness of the system at hand, we were able to find evidence that the self-consistent periodic wave that appears in such models does not arise as a consequence of a Hopf bifurcation of the system's fixed point, which remains stable and that it is a phe-

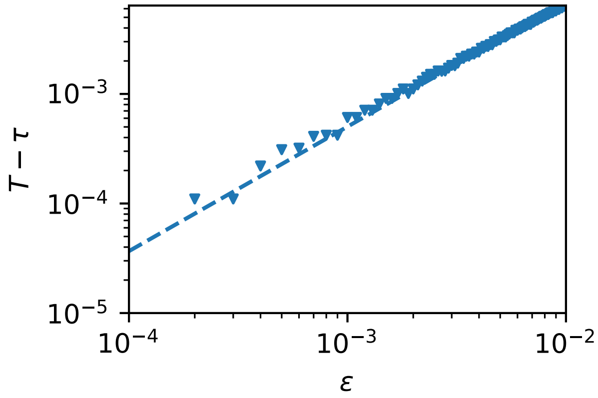

FIGURE 2.10: $T - \tau$ gap dependence on the value on the stiffness parameter ε, for the Delay differential equation. The coupling and the delay were fixed at values $J = 1.5$, $\tau = 1$. The dashed line is a power law fit, yielding an exponent ≈ 1.14.

nomenon without a natural length scale. More specifically for the trend of the wave speed an explanation has been proposed in terms of the system nonlinearity and proof has been found that the wave formation is a consequence of the balanced interplay between the discrete nature of the system and the finite reaction timescale ε. We show that evidence supporting these arguments can be obtained by examining the mechanism by which the wave disappears for large coupling values and that an increase in the coupling is to an extent equivalent to a reduction of the reaction timescale. This kind of interplay is similar to what is observed e.g. in traffic models [69], hinting to a possible degree of universality. In addition, we are able to formulate an analogue setting in terms of a single neuron Delay Differential Equation, which admits a stable limit cycle solution for a certain set of parameters if and only if the chain admits a self-consistent wave, and from which the self-consistent periodic solution can be easily interpolated. The mapping of systems and solutions is bidirectional so that given the parameters of the DDE or of the chain, and the solution period, one is able to calculate the parameters of the equivalent system. The DDEs constructed through this procedure display a perfect correspondence of solutions with the chain. The attraction basins, on the other hand, are observed to be different between the chain and the DDE, as it is expected since they are global features of the system. Similarly, the dissipation rate of solutions approaching the self-consistent periodic solution/limit cycle is found to greatly differ between the two systems, the chain being much quicker in relaxing to the self-consistent solution than the DDE to the limit cycle. Furthermore, the mapping to an infinite dimensional system such as a DDE could in principle open up new approaches to the study of the chain solution based on this analogy.

Appendices

2.5 | Numerical details

We gather in this appendix some details concerning technical aspects of the simulations performed for this chapter. The simulations of the chain (2.6) were performed through the Radau method routines [39] provided by the Scipy package [94], with the initial perturbation being a Gaussian pulse in the fast variable parameterized as follows

$$\begin{aligned} u_n(0) &= -a + Ae^{-(n-\mu_N)^2/2\sigma_N^2} \\ v_n(0) &= a - a^3/3 \end{aligned} \tag{2.18}$$

with $\mu_N = N/2$, $\sigma_N = 10^{-2}N$, $A = 2$. The integrator was set to operate with a relative and an absolute tolerance of 10^{-4}, and an initial timestep of 10^{-6}. All the speed and period values reported in Figures 2.2, 2.3, 2.4 and 2.8 were calculated as follows. First the maximum of the wave profile, corresponding to the rising wave front was located for each integration timestep. Then the location values were mapped to a monotonically nondecreasing time series by accounting for the periodicity of the system, and thus adding an N for each revolution around the ring. Finally, the monotonic time series trend has been fitted with a line versus time, so to obtain the wave speed as the angular coefficient. To perform the linear regression Scipy [94] routines were used. All the aforementioned simulations had a duration of 25 time units, which has been deemed sufficient to let the transients relax in the chain systems.

The simulations for the Delay Differential Equation (2.11) were all performed with the RADAR5 [35–37] integrator. Both the relative and absolute tolerance of the integrator were set at 10^{-12}, and the initial step size to 10^{-6}. In Figures 2.5 and 2.6 the system was simulated for a time of 30τ, the area of the limit cycle being calculated from the average of the cycles present in the final 30% of the trajectory. The detection and separation of cycles has been performed by means of a Poincaré section in the form of a vertical line through the fixed point. The calculation of areas has been performed via the well-known Surveyor's formula. In both Fig. 2.9 and Fig. 2.10, the simulation duration was of 100τ for each instance of the system, the reason for the longer runs being the attempt to mitigate the effect of transients finer measurements. Periods were calculated here as well by means of Poincaré section.

For Fig. 2.7 there was again a need for mitigation of transients so that a total duration of 80 time units was selected for both the chain and the DDE simulations. The isolation of the DDE limit cycle has been performed via Poincaré section. Initial pulses were of the form (2.18) with $A = 2.5$ for the chain and of the form (2.17) with $A = 12.5$ for the DDE. The reason for the larger pulse in the DDE is that from our studies the delayed system appears much more dissipative than the chain, so that even if a stable limit cycle exists, a too weak initial pulse could be unable to push the system onto it.

2.6 | The RADAR5 integration algorithm

All the simulations involving DDEs in this chapter and in the rest of this thesis, have been performed using the RADAR5 integration algorithm [35–37], by Nicola Guglielmi and Ernst Hairer. The algorithm is designed for the solution of initial value problems of the form

$$\begin{aligned} M\dot{\mathbf{y}}(t) &= \mathbf{f}\,(t, \mathbf{y}(t), \mathbf{y}(\alpha_1(t, \mathbf{y}(t))), \ldots, \mathbf{y}(\alpha_m(t, \mathbf{y}(t)))) \\ \mathbf{y}(t_0) &= \mathbf{y}_0, \quad \mathbf{y}(t) = \mathbf{g}(t) \text{ for } t < t_0 \end{aligned} \tag{2.19}$$

where the real state variables $\mathbf{y}$ are arranged in a d dimensional vector, M is a $d \times d$ dimensional real matrix, and we use the notation $\alpha_i(t, \mathbf{y}(t)) \leq t$ to indicate that the value of the equation vector field can depend also on the state at a different time along the system orbit, and that the amount of delay or advancement can in principle be time and state dependent. Many problems can be cast in this form. For example, the matrix M could arise from the discretization of a time-delayed Partial Differential Equation. The algorithm, in particular, does not need to invert M, therefore avoiding the disruption of its sparsity pattern, which can lead to problems due to small denominators or in general increase the numerical overhead of the computation, in the case for example of very large systems. M can also be singular, thus making the algorithm able to solve also Differential-Algebraic problems. A class of equations, solvable by the algorithm, is that of *singularly perturbed problems*, i.e. those problems where the mass matrix takes the form

$$M = \begin{pmatrix} I & 0 \\ 0 & \varepsilon I \end{pmatrix} \tag{2.20}$$

with $\varepsilon \ll 1$, which is clearly the case for the FitzHugh-Nagumo system. These equations form an important class of so called *stiff* problems.

A clear definition of a stiff problem is difficult to give, as an equation is stiff in a strict sense only in relationship to a given algorithm. Nevertheless in general a problem is referred to as stiff, if one or more algorithms yield numerically unstable solutions to it, unless a very small integration step is set. Singularly perturbed problems, in particular, are stiff with respect to *explicit* integration algorithms due to the separation of timescales, that can cause an exponential magnification of approximation errors for fixed step schemes, or a convergence of the step for variable step ones. Numerical integration schemes can be categorized as explicit or explicit, depending on how the calculation of the advanced state of the system is effected.

- In an *explicit scheme*, the state at a future time is calculated purely as a function of the present state and parameters, and of the system's trajectory in the case of DDEs. Schematically, for a single delay τ

  $$\mathbf{y}(t + \Delta t) = \mathbf{F}(\mathbf{y}(t), \mathbf{y}(t - \tau)) \tag{2.21}$$

  The construction and choice of the form of $\mathbf{F}$ is an integral part of the algorithm design process and must be adapted to possible special requirements of the problem one is considering. Generally, these methods the least computationally expensive, as an integration step requires a single functional evaluation, up to the implementation of variable step control strategies.

- In an *implicit scheme* the evolved state at a future time is found by solving an equation, that in general can be nonlinear, depending on the features of the system. Using the same notation of the previous example, we can outline the procedure involved in performing an integration step as

  $$G(\mathbf{y}(t + \Delta t), \mathbf{y}(t), \mathbf{y}(t - \tau)) = 0 \tag{2.22}$$

  As in the previous case, the choice of G is a fundamental part of the algorithm design. A step of this type of algorithms is more costly, as it requires solving (2.22) in a general way, via numerical root finding methods.

The suitability of one or the other type of scheme depends on the problem one is solving. When one is confronting stiff problems, implicit algorithms are more useful than explicit ones, as the additional time complexity entailed in the execution of numerical root finding routines for each step is often more convenient than the abnormally small step that would be required by using a fixed step explicit algorithm. RADAR5 is an implicit scheme, making it suited to the solution of stiff and singularly perturbed Delay Differential Problems. The algorithm itself is based on Radau methods, which are a family of fully implicit Runge-Kutta methods. In particular, the code on which RADAR5 is built originates from the well known previously developed routines RADAU-II [95].

3 | A simple model for delay stabilization of nonlinear dissipative systems

3.1 | Introduction

The presence of delay is ubiquitous in the description of natural phenomena, and especially when one is considering coarse-grained mesoscopic descriptions of complex systems delays can make their appearance quite naturally in physical models. A typical source of delay can be found, for example, whenever information exchange processes are modeled. Suppose e.g. that one is studying a physical system that modifies its current state in function of the state itself. If processing the state information involves a series of tasks which take a significant amount of time with respect to the typical timescales on which the system itself is operating, the function at a given time will depend on the state the system had when the processing began, thus introducing an explicitly delayed effect in the process. Some famous examples of this type of configuration can be found in biological systems such as erythrocyte homeostasis, where the production of healthy red blood cells by the bone marrow can take up to days since the detection of a low hematocrit. To model this feature of the blood-bone marrow system, the well-known Mackey-Glass model [63] includes an explicit delay in the term representing the synthesis rate of new cells. Chemical systems can also display delayed effects [27], due to finite time transport phenomena or finite time reactions, in particular when complex processes with intermediate byproducts are considered. Delayed effects are also typical of technological applications, where systems are engineered to achieve specific tasks or functions through carefully designed feedback mechanisms, in such applications the processing time between state sensing and feedback actuation can have relevant dynamical effects [91]. From a mathematical point of view if one starts with a system modeled by an Ordinary Differential Equation (ODE) and introduces delay, a Delay Differential Equation (DDE) is obtained. A DDE is formally a substantially different object: it is an infinite dimensional dynamical system where a function should be provided as the initial condition. Among the manifestations of the irreversible nature of time evolution in a DDE we should account for the fact that the phase flow is no longer a group, but rather a monoid, since in general it may not be possible to construct the inverse for a time-evolution transformation. Analogously, in the ODE phase space, the DDE orbits may have intersections, as the existence and uniqueness theorem is lifted to a functional space. In general the introduction of delay can have dramatic effects on the qualitative dynamics of a system, generating various types of chaotic and pre-chaotic behaviour such as period doubling and intermittences in otherwise regular systems [96], inducing bifurcation, or, conversely to the first point, stabilize regular orbits in chaotic systems [8, 81, 82, 90].

In the previous chapter we have shown numerically that dynamical steady states in a chain of excitable neurons correspond to limit cycles in an effective DDE, which shares the non-delayed dynamics with the chain sites but has the inter-site coupling term replaced with a delayed feedback. Additionally, we have gathered numerical evidence that the bifurcation by which these limit cycles are stabilized is a saddle-node bifurcation of limit cycles, whereby a pair of closed one-dimensional structures in phase space are created, one stable and one unstable, without altering the stability of the global fixed point of the system, and thus giving rise to a multistable configuration where the system orbit goes toward either the stable cycle or the fixed point depending on the features of the initial impulse.

Inspired by the theory of normal forms for dynamical systems in the vicinity of attractors [16], in this chapter we formulate a simplified model for the stabilization induced by a delayed feedback in nonlinear dissipative systems. Starting from an intuition gained in the study of the excitable FitzHugh-Nagumo system, which spends a long time in the neighbourhood of the u nullcline during its evolution towards the fixed point, we identify the presence of such a privileged locus, in an average sense, as one of the key ingredients for this type of bifurcation. By building a model with this feature directly in normal coordinates, we are able to identify a further requirement, the skewness of the delayed term coupling, as we are able to prove that diagonal feedback terms are unable to stabilize limit cycles. Thanks to a couple very simple insights obtained from numerical simulations, we are able to introduce an *ansatz* for the solution that allows us to apply an averaging principle and some techniques from adiabatic theory, which allow us to reconstruct the equation of the invariant manifolds for small values of the delay coupling. Using this approach we are also able to reconstruct analytically the limit cycle stability region in parameter space, and draw analytical bifurcation diagrams showing the dependence of the limit cycle area as a function of the system parameters. To gain some insight on the reason underlying the relative simplicity of the system's stationary dynamics, despite the formally infinite dimension of the dynamical system, we perform a perturbative expansion in terms of the difference between the natural period of the system and the feedback delay, showing that at the first perturbative orders the dynamical phase transition appears to be planar. The foremost contribution in literature to the understanding of the effects of the introduction of an explicit delay feedback in nonlinear systems is credited to Pyragas [81, 82], who formalized the problem in terms of control theory for chaotic systems, where unstable periodic orbits of arbitrary periods can be stabilized by a delayed feedback that vanishes once the orbit is achieved. This approach has also been adapted to study the synchronization of networks of delayed systems that do not necessarily exhibit chaotic behavior [59]. While the Pyragas control scheme maintains validity in a broad number of cases due to its generality, it assumes that the period of the stabilized orbit will be equal to the delay time of the feedback, an assumption that is justified in chaotic systems displaying dense power spectra. Our approach shows that the stabilization of quasi-invariant orbits in regular systems revolves entirely around the existence of a small but finite difference between the orbit period and the delay, which the system can exploit to balance the dissipation, in an averaged sense, over a full revolution along the cycle. We conclude by applying the developed method to the FitzHugh-Nagumo system in a spiraling regime where we are able to construct the normal coordinates in proximity of the fixed point, confirming the findings obtained on the simplified model. As a byproduct we collect significative evidence of higher order effects in the dissipation landscape of the FitzHugh-Nagumo neuron, which could provide an explanation for the bifurcation observed in the use cases from the previous chapter, when combined with a different set of normal coordinates which, at the time of writing, the author was unable to find.

3.2 | Normal form for isolated almost invariant orbits and model definition

The aim of this chapter is the formulation of a simple model that captures all the relevant features of a delay-induced bifurcation of limit cycles in systems that exhibit a nonlinear dissipation. To do so, we first construct a normal form approach to systems that exhibit isolated almost invariant orbits. In particular our approach to normal forms is based on their usage in perturbation theory [17], within which they are used as a starting point to approximate more complicated systems in the neighbourhood of an orbit or a domain of interest for the properties one is interested in studying.

A feature of the FitzHugh-Nagumo model is that the orbits spend a long time, of order $\mathcal{O}(1)$ in the slow timescale, in the vicinity of the external branches of the u nullcline, which is the locus in phase space where the time derivative of u vanishes. This is a general aspect of the model dynamics for $\varepsilon \ll 1$, as it is observed both for the stable limit cycle present in the system for $|a| < 1$ and for the dissipative orbit of the $|a| > 1$ case. In particular in this latter case we can refer to the external nullcline branches as to an almost invariant orbit, since the system spends a long time in their vicinity, apart from the time of order $\mathcal{O}(\varepsilon)$ which it takes to jump from the right to the left one, eventually approaching the fixed point which lies on the nullcline itself. Even though our inspiration for the model that follows was this aspect of the FitzHugh-Nagumo system, similar phenomena are quite general, as many nonlinear systems of interest show quasi invariant structures in phase space, so that our discussion is valid in general near any quasi invariant structure of a dynamical system. In the vicinity of an elliptical point of a nonlinear dynamical system, a system of normalized coordinates can be introduced, called Birkhoff coordinates [16], in which closed orbits are mapped into circles on which the system moves with a constant velocity, casting the dynamical system in the form of a rotator. The same type of transformation can be introduced near an attractive point, mapping dissipative orbits that fall on the point to spirals of an underdamped rotator, governed by the standard equations

$$\begin{aligned} \dot{q} &= \omega p - \mu q \\ \dot{p} &= -\omega q - \mu p. \end{aligned} \tag{3.1}$$

where $\omega > 0$ and $\mu > 0$ are respectively the imaginary part and the magnitude of the real part of the original system's linearization in a neighbourhood of the fixed point. In this context, (3.1) is referred to as a *normal form* for the original system in the neighbourhood of the fixed point.

In our case, we assume that by setting the origin of the normal coordinates within the region delimited by the quasi invariant orbit, the orbit itself is cast into a quasi invariant circle of radius $\sqrt{2\bar{I}}$ with $\bar{I}$ the value of the geometrical action on the circle. Now, for consistency with the previous assumptions and to encode the privileged nature of the quasi invariant orbit in phase space, we modify the system by making the dissipation term nonlinear,but dependent only on the geometrical action of the system, turning (3.1) into

$$\begin{aligned} \dot{q} &= \omega p - \gamma(q, p)\, q \\ \dot{p} &= -\omega q - \gamma(q, p)\, p, \end{aligned} \tag{3.2}$$

where γ is the nonlinear dissipation which we set to

$$\gamma(q,\, p) = \left(\frac{q^2+p^2}{2} - \bar{I}\right)^2 + \mu = \left(I(q,\, p) - \bar{I}\right)^2 + \mu \quad \bar{I} > 0$$

where I is the system's geometrical action, and μ and ω are the magnitudes of the real and imaginary part of the eigenvalues of the original system, linearized in the vicinity of the quasi invariant orbit. Notice that, because of the quasi invariance, i.e. the fact that the original system spends a long time near the quasi invariant orbit, we can assume $\mu \ll 1$. This way, the simplified system reduces to a normal form approximating the original system in the vicinity of the quasi invariant orbit only in the vicinity of the quasi invariant circle to which the latter was mapped.

3.3 | Bifurcation study

3.3.1 | Self-consistent linearization and conditions on the feedback coupling

The dynamical effects of the introduction of a feedback in a dynamical systems can depend greatly on the type of coupling that is implemented. Letting $X = (x, y)$ denote the state vector of a dynamical system and $f(X)$ the system's right hand side in absence of feedback, we will focus on feedback terms that enter the system equations in the form

$$\dot{X} = f(X) + \varepsilon B\left(X_\tau - X\right),$$

where we denote with the subscript τ the term $X_\tau = X(t-\tau)$, $\varepsilon > 0$ a coupling strength and B is a two by two coupling matrix with binary entries that can be either 0 or 1. In this context, we distinguish two types of coupling:

- *Diagonal*, where the matrix B is chosen to be either of the following

  $$\Pi_x = \begin{pmatrix} 1 & 0 \\ 0 & 0 \end{pmatrix}, \quad \Pi_y = \begin{pmatrix} 0 & 0 \\ 0 & 1 \end{pmatrix},$$

  i.e. a projector on one of the two dynamical variables subspace,

- *Skew*, where the matrix is chosen among

  $$\Pi_{xy} = \begin{pmatrix} 0 & 0 \\ 1 & 0 \end{pmatrix}, \quad \Pi_{yx} = \begin{pmatrix} 0 & 1 \\ 0 & 0 \end{pmatrix},$$

  so that there is a mixing of the coordinates in the feedback term.

In general we can prove that the only feedback able to stabilize a quasi invariant orbit is of the *skew* type. To prove this, let us consider a system that has already been linearized in the vicinity of the quasi invariant orbit, taking the form of a damped oscillator, its equation will read

$$\begin{aligned} \dot{x} &= y \\ \dot{y} &= -\omega_0^2 x - \mu_0 y \end{aligned} \tag{3.3}$$

where the subscript 0 indicates that the frequency and dissipation factor refer to the system in its original coordinates. Provided that the system is underdamped, we can cast it into normal coordinates via a transformation in the form

$$T = \begin{pmatrix} t & 0 \\ s & t^{-1} \end{pmatrix},$$

which will map the x, y coordinates to the normal coordinates q, p and where the free parameters are only two since the transformation is determined up to a basis change and the mapping must be area preserving. In order to correspond to its definition, T must solve the equation

$$\begin{pmatrix} 0 & 1 \\ -\omega_0^2 & -\mu \end{pmatrix} \begin{pmatrix} t & 0 \\ s & t^{-1} \end{pmatrix} = \begin{pmatrix} t & 0 \\ s & t^{-1} \end{pmatrix} \begin{pmatrix} -\mu & \omega \\ -\omega & -\mu \end{pmatrix}, \tag{3.4}$$

where the frequency ω is the imaginary part of the eigenvalues of (3.3) and μ is just a scaled counterpart of μ_0

$$\mu = \frac{\mu_0}{2}, \quad \omega = \frac{\sqrt{4\omega_0^2 - \mu_0}}{2} \tag{3.5}$$

so that the transformation maps (3.3) to the standard form of a damped rotator. Solving (3.4) we get the matrix parameter values

$$t^2 = \frac{1}{\omega}, \quad s = -\frac{\mu}{\sqrt{\omega}}.$$

If the considered system has a diagonal feedback term, which we take without loss of generality to be in the y coordinate, the mapping of the equations between the different sets of coordinates will be

$$\begin{gathered} \dot{X} = \begin{pmatrix} 0 & 1 \\ -\omega_0^2 & -\mu \end{pmatrix} X + \varepsilon \Pi_y (X_\tau - X) \\ \Downarrow \\ \dot{Q} = \begin{pmatrix} -\mu & \omega \\ -\omega & -\mu \end{pmatrix} Q + \varepsilon T \Pi_y T^{-1} (Q_\tau - Q), \end{gathered} \tag{3.6}$$

Where we have used the notation $Q = (q, p)$ and the explicit form of the projector in the new coordinates is

$$T\Pi_y T^{-1} = \begin{pmatrix} 0 & 0 \\ -\mu/\omega & 1 \end{pmatrix}. \tag{3.7}$$

Searching for a solution to the lower equation in (3.6) in the form

$$\begin{pmatrix} q(t) \\ p(t) \end{pmatrix} = \begin{pmatrix} q_0 \\ p_0 \end{pmatrix} \exp(\lambda t)$$

we obtain the self-consistent secular equation

$$\begin{aligned} &\det \begin{pmatrix} \lambda + \mu & -\omega \\ \omega + \frac{\varepsilon\mu}{\omega}\left(e^{-\lambda\tau} - 1\right) & \lambda + \mu - \varepsilon\left(e^{-\lambda\tau} - 1\right) \end{pmatrix} \\ &= \lambda^2 + 2\mu\lambda + \mu^2 + \omega^2 - \varepsilon\lambda\left(e^{-\lambda\tau} - 1\right). \end{aligned} \tag{3.8}$$

The birth of a repulsive structure between the quasi invariant orbit and the origin is detected in the linearized system as a change of stability of the origin, i.e. a purely imaginary exponent $\lambda = i\Omega$. Setting this condition into (3.8) and separating real and imaginary part, we obtain for the latter

$$\frac{2\mu}{\varepsilon} = \cos\Omega\tau - 1, \tag{3.9}$$

which has no solution for positive ε. If, conversely, we perform the same calculation for a skew system, we will observe simply a scaling of the coupling of a factor ω^{-1}, further remaking that the translation into normal coordinates is well posed only for a system with nonzero imaginary part of its eigenvalues. These findings enable us to state that in systems that are approximated in the vicinity of the quasi invariant orbit by an underdamped oscillator, said orbit *cannot* be stabilized by a diagonal feedback. An analogous calculation shows that also the introduction of a diagonal feedback in a system that is already in normal coordinates is unable to stabilize the orbit. For these reasons, in the following we will consider a system with skew feedback, in particular one where the q variable is fed into the p dynamical equation without loss of generality.

With these considerations in mind we propose as a normal form for a delay induced bifurcation of limit cycles in nonlinearly dissipative systems the model

$$\begin{aligned} \dot{q} &= \omega p - \gamma(q, p)q \\ \dot{p} &= -\omega q - \gamma(q, p)p + \varepsilon(q_\tau - q) \end{aligned} \tag{3.10}$$

where ε is the feedback coupling strength and $\gamma(q, p)$ is the previously introduced nonlinear dissipation factor, in the form

$$\gamma(q, p) = \left(\frac{q^2 + p^2}{2} - \bar{I}\right)^2 + \mu = \left(I(q, p) - \bar{I}\right)^2 + \mu \quad \bar{I}, \mu > 0$$

where we take $\mu \ll 1, \bar{I} = \mathcal{O}(1)$, and we have introduced the geometrical action

$$I(q, p) = \frac{q^2 + p^2}{2}.$$

The dynamical variables are taken to be evaluated at time t, the present time, if no subscripts are present, while we use the notation

$$q_\tau = q(t - \tau), \quad p_\tau = p(t - \tau)$$

for the delayed variables, notating as τ the feedback delay.

We study the system with the same self consistent linearized approach that has been used previously to rule out diagonal feedback configurations. In proximity of the quasi invariant circle we can approximate (3.10) by

$$\begin{aligned} \dot{q} &= \omega p - \mu q \\ \dot{p} &= -\omega q - \mu p + \varepsilon\left(q_\tau - q\right) \end{aligned} \tag{3.11}$$

so that the system is locally linear. By looking for a solution to (3.11) in the form

$$\begin{pmatrix} q(t) \\ p(t) \end{pmatrix} = \begin{pmatrix} q_0 \\ p_0 \end{pmatrix} \exp(\lambda t)$$

we can write the eigenvalue equation as

$$\begin{aligned} \det\left(\lambda I - A(\lambda)\right) &= \det\begin{pmatrix} \lambda + \mu & -\omega \\ \omega - \varepsilon\left(e^{\lambda(t-\tau)} - 1\right) & \lambda + \mu \end{pmatrix} \\ &= \lambda^2 + 2\mu\lambda + \mu^2 + \omega^2 - \varepsilon\omega\left(e^{-\lambda\tau} - 1\right) = 0. \end{aligned} \tag{3.12}$$

While in a linear system the existence of a closed orbit is granted only for an exactly vanishing real part of the eigenvalues, i.e. at the point where the eigenvalues lie exactly on the imaginary axis, this may not be the case for nonlinear systems. Indeed in systems such as the one currently under study, the increase of the dissipation coefficient for larger and larger values of I, grants that even for a system that is locally expanding in the vicinity of the quasi invariant orbit, such expansion will be balanced by the dissipation. This can also be argued for in topological terms: since the point at infinity must remain repulsive because of its diverging dissipation value, the birth of an expanding circular region wrapping around the origin warrants the birth of an attractive structure around itself. Substituting $\lambda \mapsto i\Omega$ at the critical point and separating the real and imaginary part equations we obtain respectively

$$\begin{aligned} \frac{\omega^2 + \mu^2 - \Omega^2}{\varepsilon\omega} &= \cos\Omega\tau - 1 \\ 2\mu\Omega &= -\varepsilon\omega\sin\Omega\tau. \end{aligned} \tag{3.13}$$

We reparameterise the delay τ by setting

$$\Omega\tau = 2\pi - \Omega\Delta,$$

where we define Δ as the *delay advancement*, i.e. the amount of time by which the feedback delay is shorter than the period of the orbit. With this definition we can recast the previous equations as

$$\begin{aligned} \frac{\omega^2 + \mu^2 - \Omega^2}{\varepsilon\omega} &= \cos\Omega\Delta - 1 \\ 2\mu\Omega &= \varepsilon\omega\sin\Omega\Delta. \end{aligned} \tag{3.14}$$

Since in numerical simulations we observe the critical value of Δ to be small, we can expand these equations to leading order and combine them to obtain

$$\Delta_c = \frac{2\mu}{\varepsilon\omega} \tag{3.15}$$

$$\Omega_c^2 = \frac{\omega^2 + \mu^2}{1 - 2\mu^2/\varepsilon\omega} \tag{3.16}$$

which are respectively lower critical value of the advancement for the appearance of an orbit and the correction to the natural frequency of the system at the critical point. Within our hypotheses $\mu \ll 1$, ε, $\omega = \mathcal{O}(1)$ we see that the correction to the frequency is relatively small, with the contribution due to the feedback amounting to the $-2\mu^2/\varepsilon\omega$ term in the denominator. The behaviour of the dominant frequency of the orbits at the critical point is therefore dominated by that of the original frequency ω.

If we are interested in the behaviour of the eigenvalues for choices of parameters close to, but beyond, the critical point we can trace back to (3.12) and set

$$\lambda = \Lambda + i\Omega, \quad \Lambda \ll 1$$

keeping only contributions at first order in Δ and Λ we get

$$\Lambda = \frac{\varepsilon\omega\Delta - 2\mu}{2\left(1 + \pi\varepsilon\Delta\right)} \tag{3.17}$$

for the scaling of the real part near the transition point, and

$$\Omega^2 = \omega^2 + \mu^2 + \frac{2\pi\varepsilon^2\omega\Delta - (2\mu - \varepsilon\omega\Delta)^2}{2(1+\pi\varepsilon\Delta)} \tag{3.18}$$

for the correction to the frequency in a neighbourhood of the transition point, so that the behaviour is once more dominated by the original frequency ω. A first test of the accuracy of this approach can be performed by fixing a value μ and checking that for fixed ε we have a stable solution only for $\Delta > \Delta_c$, and analogously fixing a Δ and varying ε in order to move the critical value Δ_c above or below the former. The results of such an experiment are shown in Fig.3.1, where we observe that a limit cycle is born for $\Delta > \Delta_c$, around the quasi invariant orbit. Moreover, we can see that the main effect on the shape of the solution of the ε value is to affect the eccentricity of the orbit, which for low values is quite circular. By looking at the system trajectories in the time domain, we can gain additional insight. When the cycle is stabilized an example of the typical behaviour is shown in Fig.3.2. The coordinate and the momentum exhibit out of phase sinusoidal oscillation, corresponding to a detuned version of the typical solution of a conservative harmonic oscillator, with frequency close to ω, the frequency of the normal form. Because of this, the action appears to oscillate sinusoidally with double the frequency of the coordinates with a small amplitude.

3.3.2 | Poincaré map and bifurcation diagrams

A saddle node bifurcation of limit cycles in a differential equation corresponds to a saddle node bifurcation of fixed points in its Poincaré map. For this reason, to detect the saddle node transition that gives birth to the stable limit cycle that we observe, we aim to reconstruct the Poincaré map, approximately if necessary, and qualify its fixed points. To do so we write the dynamics of the action from the dynamical equations of the system, and get

$$\dot{I} = -2\gamma(I)I + \varepsilon p\,(q_T - q)\,. \tag{3.19}$$

Due to the delay, we have a term in the equation that still depends on the coordinates, which we would like to remove in order to obtain a one-dimensional dynamical system that specifies the dynamics of the action in terms only of the action itself. Guided by the results of numerical simulations, we make the following *pseudo-elliptical ansatz*[1]

$$q(t) = \sqrt{2I}\sin(\Omega t - \alpha/2)\,, \quad p(t) = \sqrt{2I}\cos(\Omega t + \alpha/2)\,,$$

---

[1] The curve used in the pseudo-elliptical ansatz is actually a special case of a *Rhodonea of Grandi*, but we use the term pseudo-elliptical due to its resemblance to an ellipse for $\alpha \ll 1$.

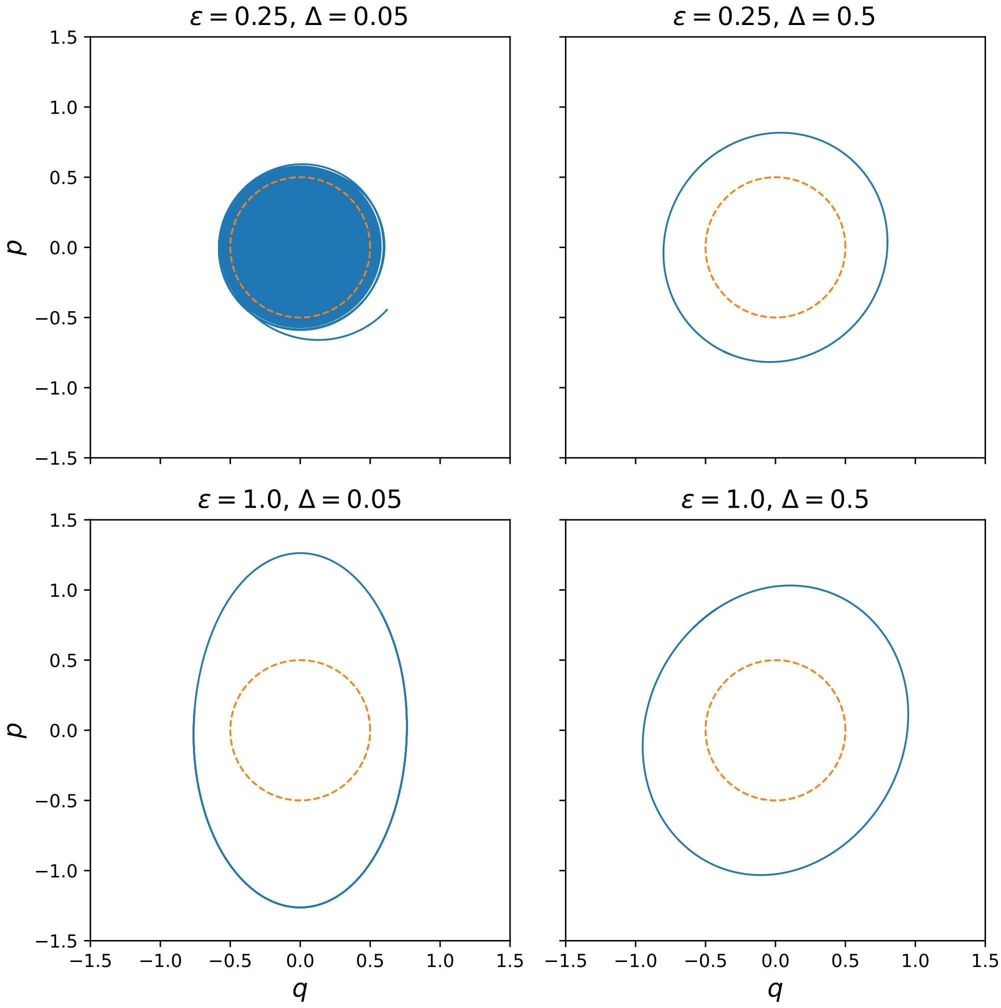

Figure 3.1: Orbits of the system for parameter choices that yield qualitatively different result. The value of the base dissipation is $\mu = 10^{-2}$. The dashed orange line marks the quasi invariant circle $I(q, p) = \bar{I} = 1/8$.

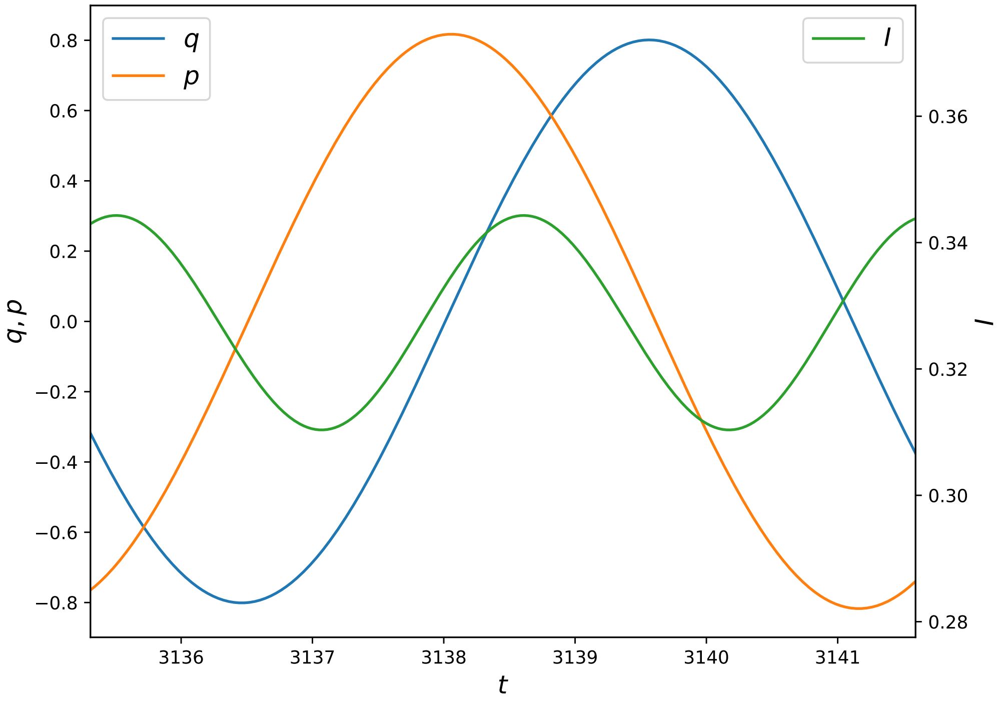

Figure 3.2: Representation in the time domain over a window $2\pi/\omega$ of the trajectory of the simplified system (3.10), for a choice of parameters $\mu = 10^{-2}$, $\varepsilon = 0.25$, $\Delta = 0.5$, corresponding to the top right quadrant of Fig.3.1. Coordinate values are read on the left, action values on the right axis. The system has been evolved for a time interval of $500 \times 2\pi/\omega$ units in order to dissipate transients.

and noticing that the fluctuation in the action along such a solution is

$$\frac{q^2+p^2}{2} = I\left(1-\sin\alpha\sin 2\Omega t\right),$$

we immediately reparameterize

$$q(t) = \sqrt{2I\left(1-\sin\alpha\sin 2\Omega t\right)}\,\sin\Omega t, \quad p(t) = \sqrt{2I\left(1-\sin\alpha\sin 2\Omega t\right)}\,\cos\Omega t,$$

so to have an expression for the position and momentum in terms of a rotation multiplied by an oscillating action. This allows us to rewrite the action dynamics (3.19), yielding the form

$$\begin{aligned}\dot{I} = &-2I\left(1-\sin\alpha\sin 2\Omega t\right)\left[\mu+\left(I(1-\sin\alpha\sin 2\Omega t)-\bar{I}\right)^2\right] \\ &+2\varepsilon I\left(1-\sin\alpha\sin 2\Omega t\right)\cos\Omega t\left(\sin\Omega(t-\tau)-\sin\Omega t\right).\end{aligned} \tag{3.20}$$

Provided we are considering motion in a region of phase space relatively close to the quasi invariant circle of minimal dissipation, i.e. where we can assume $\mu+(I-\bar{I})^2 \ll \Omega$, so that we can treat I as a constant on time intervals of order μ^{-1}, we can average (3.20) over a period $\Omega/2\pi$ [7], or equivalently along one revolution around the origin, and get

$$\begin{aligned}\frac{2\pi}{\Omega}\left(I_{n+1}-I_n\right) = -2&\left[\mu+\left(I_n-\bar{I}\right)^2+I_n\sin^2\alpha\left(\frac{3}{2}I_n-\bar{I}\right)\right]I_n \\ &+\varepsilon\left(\sin\alpha\sin^2\left(\frac{\Omega\tau}{2}\right)-\sin\Omega\tau\right)I_n,\end{aligned} \tag{3.21}$$

where by I_n we indicate the average action during the n-th revolution around the origin. The meaning of (3.21) is analogous to that of a Poincaré map, but in an averaged sense, in the fact that it is a discrete dynamical system that maps the average action during the n-th revolution to that during the $n+1$-th, with the important advantage with respect to the other descriptions of dynamical system (3.10) that the dynamics is no longer delayed, so that to determine the average action at the next iteration of the map only the previous value is needed. Despite this dimensionality reduction the information about the effect of the explicit delay in the original system is preserved, since τ remains as a parameter.

Fixed points of the map (3.21) correspond by definition to closed one-dimensional invariant manifolds in the phase space of (3.10). From these considerations it is easy to recover the equation for the attractors in phase space

$$\frac{\varepsilon}{2}\left[\sin\alpha\sin^2\frac{\Omega\tau}{2}-\sin\Omega T\right] = \mu+\left(I-\bar{I}\right)^2+I\sin^2\alpha\left(3I-2\bar{I}\right), \tag{3.22}$$

which for the time being is underdetermined, since it is a single equation for two variables I and α. To better compare it to the previous results we recast the terms containing the delay τ in terms of the delay advancement $\Delta = 2\pi/\Omega - \tau$, which yields

$$\frac{\varepsilon}{2}\left[\sin\alpha\sin^2\frac{\Omega\Delta}{2} + \sin\Omega\Delta\right] = \mu + \left(I - \bar{I}\right)^2 + I\sin^2\alpha\left(3I - 2\bar{I}\right). \tag{3.23}$$

The geometrical interpretation of the parameter α is linked to the pseudo-eccentricity of the pseudo-elliptical orbit, i.e. the quantity governing the amount by which the orbit deviates from a circle. Since from numerical evidence we expect that close to the critical point the orbit will be scarcely eccentric and well approximated by a circle, we can set in first approximation $\alpha = 0$ in (3.23), simplifying the equation to

$$\varepsilon\sin\Omega\Delta = 2\mu + 2\left(I - \bar{I}\right)^2. \tag{3.24}$$

At the critical point the stable and unstable limit cycle coalesce, defining an invariant manifold with saddle node-like stability, i.e. attractive from one side and repulsive on the other. This allows us to define the critical point of the bifurcation as the point where (3.24), interpreted as an equation for I, admits two degenerate real roots $I_\pm = \bar{I}$. Imposing this condition we get the following expression for the critical advancement

$$\Delta_c = \frac{1}{\Omega}\arcsin\frac{2\mu}{\varepsilon} \tag{3.25}$$

where Ω at this point remains undetermined, but in light of the findings of the previous sections can be approximated near the transition as $\Omega \approx \omega$. If, in addition to this, we expand the sinus in (3.24) for small Δ we recover the familiar expression of the previous sections

$$\Delta_c = \frac{1}{\Omega}\arcsin\frac{2\mu}{\varepsilon} \quad \longrightarrow \quad \Delta_c = \frac{2\mu}{\varepsilon\omega}.$$

By solving for I in (3.24) we can also find the equation for the action values of the circular approximants to the invariant manifolds

$$I_\pm = \bar{I} \pm \sqrt{\frac{\varepsilon\Omega}{2}\left(\frac{\sin\Omega\Delta}{\Omega} - \Delta_c\right)} \tag{3.26}$$

which can simplified as well for $\Delta \ll 1$

$$I_\pm = \bar{I} \pm \sqrt{\frac{\varepsilon\omega}{2}\left(\Delta - \Delta_c\right)}. \tag{3.27}$$

Since they originate from a saddle node bifurcation, and both the origin and the point at infinity do not change their stability, we expect the innermost cycle to be an unstable one and the outermost to be stable. By linearising the map near the fixed points $I_\pm$, working with $\alpha = 0$, we find the Lyapunov exponent in a neighbourhood of the fixed points

$$\Lambda_\pm = 4\left(\bar{I} - I_\pm\right) I_\pm$$

thus confirming the intuition that I_- is repulsive and I_+ attractive and providing grounds to expect a multiattractive behaviour, depending on the initial value of the action $I(t_0) = I_0$. Indeed, in general, we expect to find that most of the orbits with $I_0 > I_+$ will end up on the stable attractor from outside, that most of those that start with $I_0 < I_-$ will end up on the fixed point, and that in the region $I_- < I_0 < I_+$ we can find orbits that are attracted by the stable attractor from inside. The statement is difficult to make in a broader and more rigorous sense due to the fact that technically the initial condition for a DDE is a function, and depending on how it is taken, some orbits with $I_0 > I_+$ could go to the fixed point, or in general not adhere to the description we have just furnished. Nonetheless, the reported behaviour was found in the great majority of simulations that were performed. An example of the multiattractive behaviour can be observed in Fig. 3.3.

To test the validity of (3.25) we perform extensive simulations. The first set of results is displayed in Figures 3.4, 3.5, 3.6, 3.7 and 3.8 containing phase diagrams built from simulations and the transition line predicted by (3.25). The general trend we observe is an increase in the minimal coupling strength required to stabilize the orbit for higher dissipations, which is expected from the previously developed expressions and reasonable from a physical point of view, as it corresponds to the gain that the system can exploit to recovery the effect of the dissipation. On the other hand we observe a limited displacement of the stable region along the Δ axis as, despite the tendency of the region to become narrower for higher values of μ, the value of Δ for which the minimal ε value is able to stabilize the cycle does not move significantly, except for large values of μ. As far as the accord with the analytical transition line is concerned, it is observed to be good for the lowest dissipation values up to $\mu = 1 \times 10^{-2}$, while for higher values the prediction worsens, as it can be expected from results originating in an adiabatic approach. It is interesting to note although, that for $\mu = 5 \times 10{-}2$, even though for the upper critical values of Δ the prediction is quite lacking, the approximation remains reasonably good for the lower critical value. For the highest dissipation value that was tested, $\mu = 10^{-1}$, the prediction has already deteriorated much more. This is likely due to the loss of applicability of the adiabatic approach on the one hand, and of the $\alpha = 0$

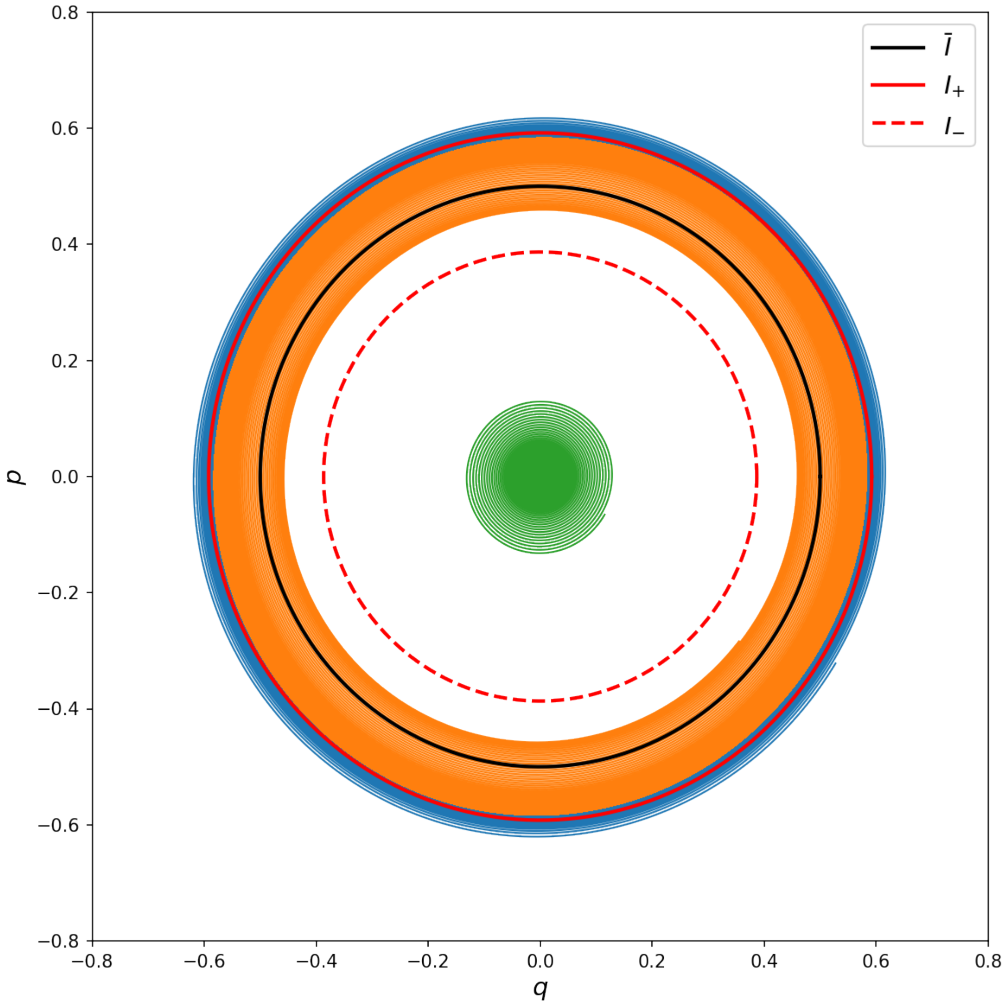

FIGURE 3.3: Three trajectories of the simplified system: with $I_0 > I_+$ (blue), with $I_- < I_0 < I_+$ (orange) and $I_0 < I_-$ (green). The continuous and dashed red lines represent respectively the circular approximants to the stable and unstable invariant manifolds. The solid black line marks the almost invariant orbit. The system parameters were taken $\varepsilon = 0.25,\ \mu = 10^{-2},\ \Delta = 10^{-1},\ \omega = 1,\ \bar{I} = 0.125$.

approximation on the other. The findings of this final section allow us to construct an analytical approximation to the bifurcation diagram of the original dynamical system, which allows to test the goodness of our prediction of the attractor location in phase space, in terms of its corresponding action value. The bifurcation diagram is displayed in Fig.3.9, where we observe a very good accordance between the predicted value and the simulated one at the onset of

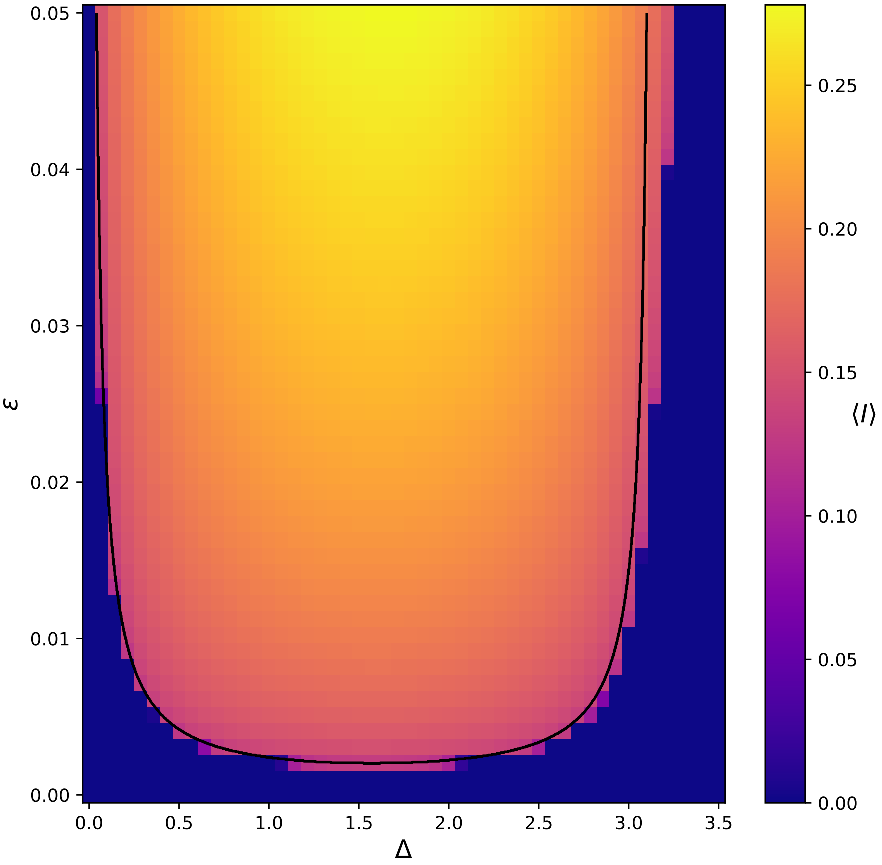

FIGURE 3.4: Phase diagram for the simplified system (3.10) with parameters $\mu = 10^{-3}$, $\omega = 1$, $\bar{I} = 0.125$. Colour scale represents the stable cycle action from simulations, the black line is the critical line predicted by (3.25).

the bifurcation for small Δ and μ (blue and orange plots), while there is a small but noticeable undershoot at the upper critical value. For larger values of μ (green plot) we are overestimating also the action at the cycle appearance. As a general trend the prediction gets worse whenever the observed pseudoeccentricity, corresponding to the vertical width of the shaded area, gets larger. This behaviour is quite expected, as our analytical formulae were all obtained in the approximation $\alpha = 0$, which ceases to be accurate when the orbit is remarkably not circular anymore.

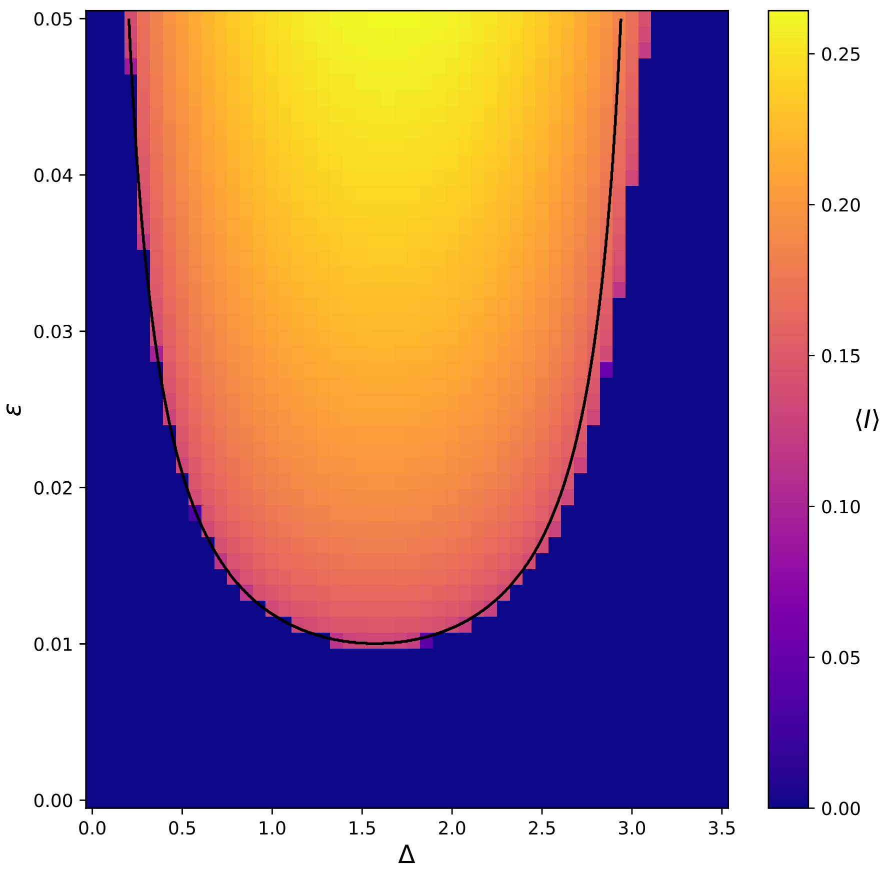

Figure 3.5: Phase diagram for the simplified system (3.10) with parameters $\mu = 5 \times 10^{-3}$, $\omega = 1$, $\bar{I} = 0.125$. Colour scale represents the stable cycle action from simulations, the black line is the critical line predicted by (3.25).

3.3.3 | Advancement perturbative expansion

An interesting feature of the system, observed in numerical simulations, is that despite the formally infinite dimensionality the system displays a very simple dynamics. To try to make sense of this aspect we pose the question of whether we can construct, perturbatively, planar dynamical systems that undergo the same transition, i.e. that stabilize a cycle for a critical value of Δ, equal to the one obtained in the previous section. From (3.25) we know that at

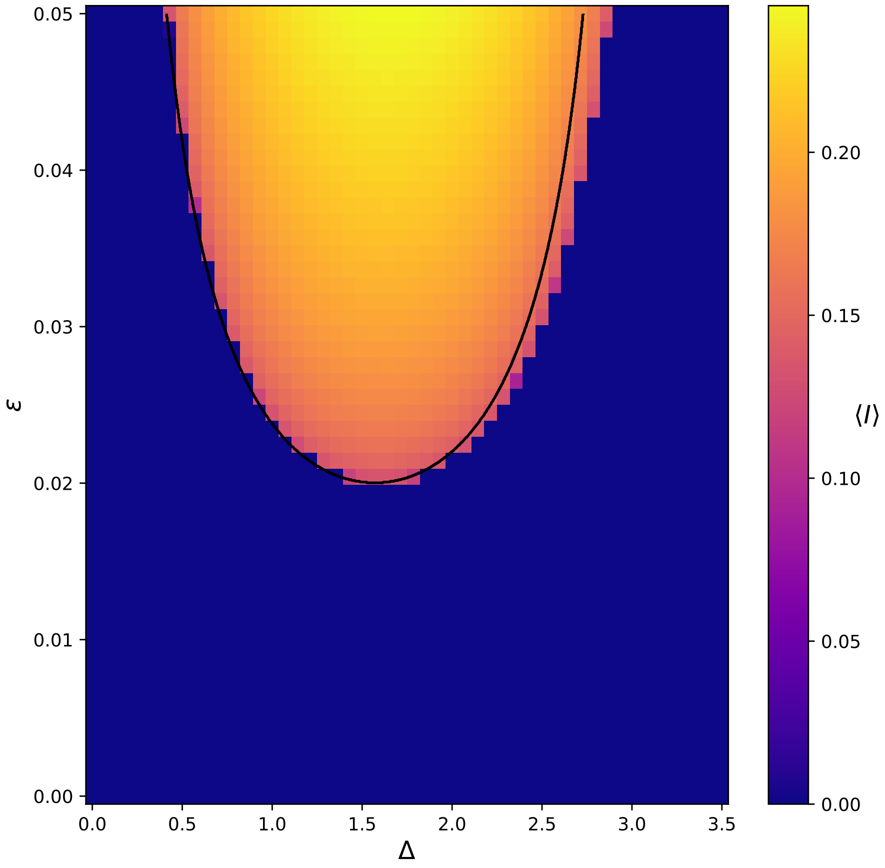

Figure 3.6: Phase diagram for the simplified system (3.10) with parameters $\mu = 10^{-2}$, $\omega = 1$, $\bar{I} = 0.125$. Colour scale represents the stable cycle action from simulations, the black line is the critical line predicted by (3.25).

the critical point, the stable orbit will lie onto the circle of minimal dissipation, corresponding to the stabilization of the quasi invariant orbit. For this reason, we neglect the nonlinear dissipation, keeping only the linear contribution from the normal form in the vicinity of the almost invariant orbit

$$\gamma(I) \approx \mu. \tag{3.28}$$

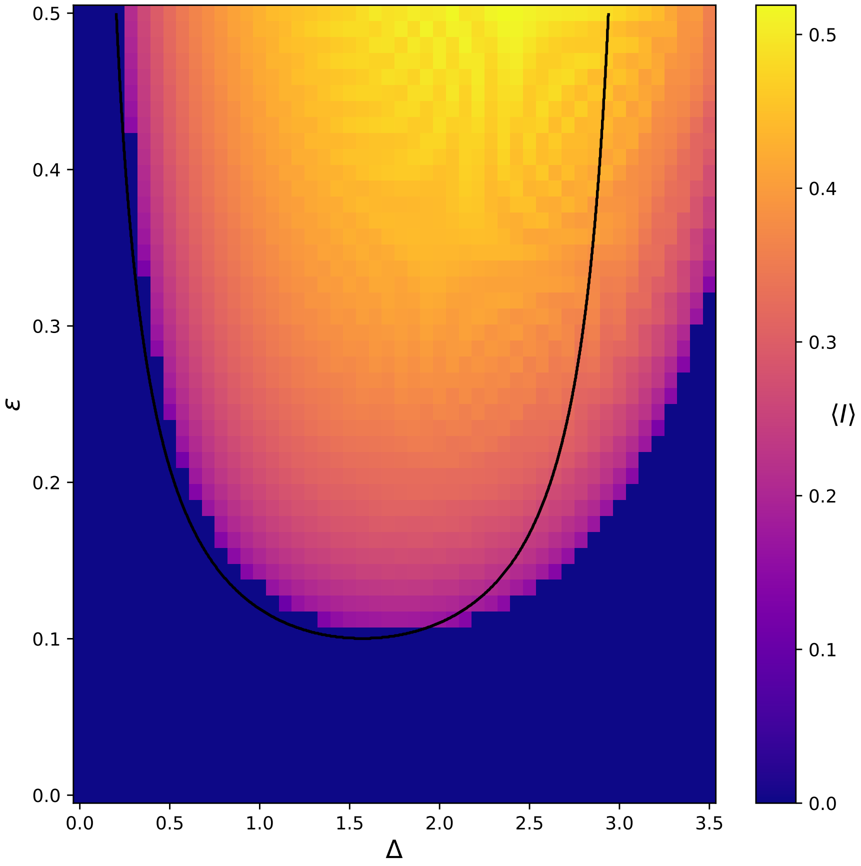

Figure 3.7: Phase diagram for the simplified system (3.10) with parameters $\mu = 5\times10^{-2}$, $\omega = 1$, $\bar{I} = 0.125$. Colour scale represents the stable cycle action from simulations, the black line is the critical line predicted by (3.25).

The equation then reads

$$\begin{aligned}\dot{q} &= \omega p - \mu q\\ \dot{p} &= -\omega q - \mu p + \varepsilon(q_\tau - q),\end{aligned} \tag{3.29}$$

From our previous treatment of the system in Section 3.3.1, we know that the dominant contribution to the frequency of the stabilized orbit near the transition point is of order ω. Our idea is then to expand the feedback term in a series of the deviation between the delay and the, approximate, period of the

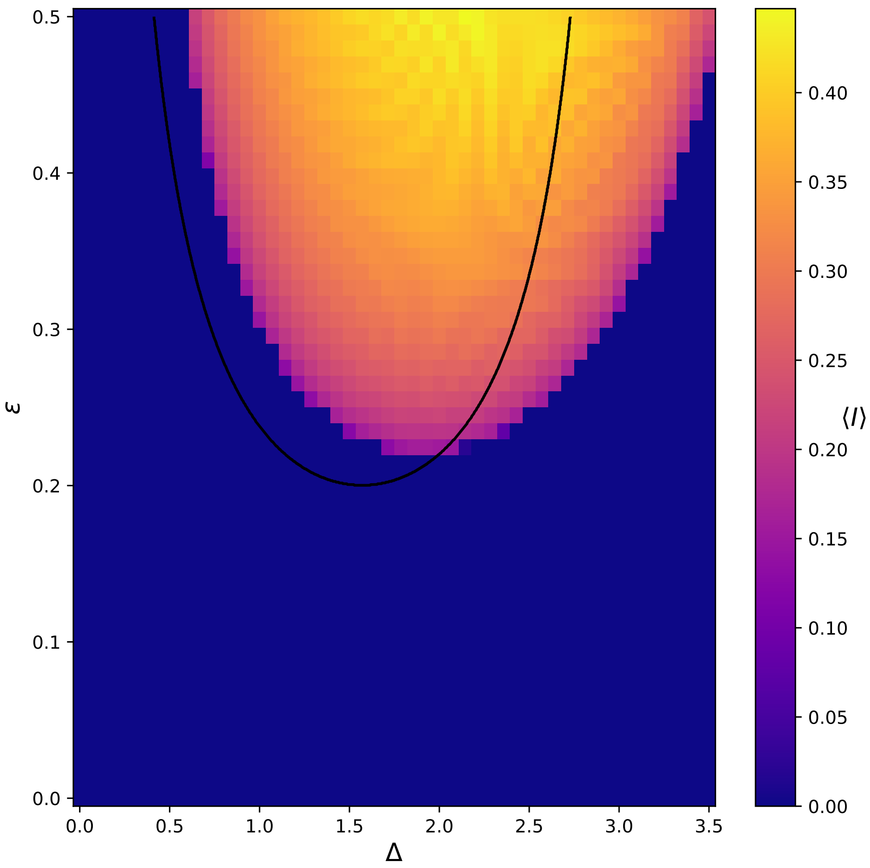

FIGURE 3.8: Phase diagram for the simplified system (3.10) with parameters $\mu = 10^{-1}$, $\omega = 1$, $\bar{I} = 0.125$. Colour scale represents the stable cycle action from simulations, the black line is the critical line predicted by (3.25).

orbit $\frac{2\pi}{\omega}$. The formal expansion reads

$$\Delta q \equiv q_\tau - q = \sum_{n=0}^{\infty} \frac{1}{n!} \frac{\mathrm{d}^n q}{\mathrm{d}t^n}\bigg|_{t+\frac{2\pi}{\omega}} \left(\frac{2\pi}{\omega} - \tau\right)^n - q \equiv \sum_{n=1}^{\infty} \frac{\mathrm{d}^n q}{\mathrm{d}t^n} \frac{\Delta}{n!}. \tag{3.30}$$

where in this Section we define $\Delta = 2\pi/\omega - \tau$, in accord with the approximation $\Omega \approx \omega$.

With these definitions, truncations of (3.30) to any finite order will furnish ODE approximations to (3.10) with polynomial a polynomial dependence on

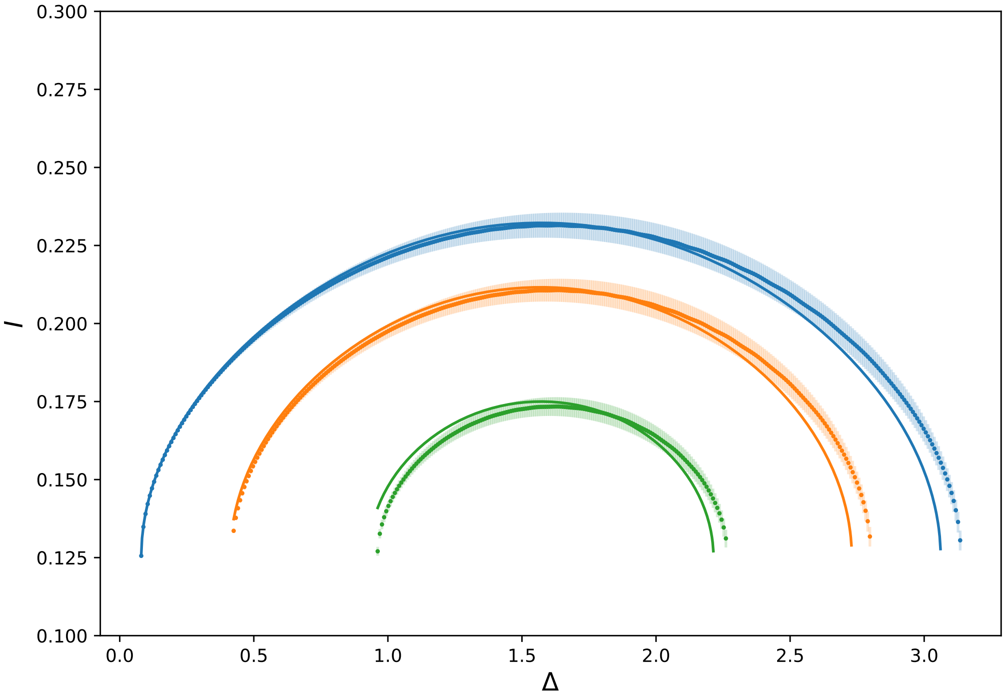

Figure 3.9: Bifurcation diagram for the system (3.10) for different values of the linear dissipation: $\mu = 10^{-3}$ (blue), $\mu = 5 \times 10^{-3}$ (orange) and $\mu = 10^{-2}$ (green). Solid lines mark the analytical value of the action on the attractor. Dots mark the averages from simulations, shaded areas indicate the oscillation of the action on the attractor. The other system parameters were fixed at $\varepsilon = 0.025,\ \bar{I} = 0.125,\ \omega = 1$.

Δ in the system matrix. We will consider the first two perturbative orders.

I order

At the first order the expansion (3.30) reduces to

$$\Delta q = (\omega p - \mu q)\Delta$$

so that the linearised system becomes

$$\begin{pmatrix} \dot{q} \\ \dot{p} \end{pmatrix} = \begin{pmatrix} -\mu & \omega \\ -\omega - \varepsilon\Delta\mu & -\mu + \varepsilon\Delta\omega \end{pmatrix} \begin{pmatrix} q \\ p \end{pmatrix} \equiv A_1(\Delta) \begin{pmatrix} q \\ p \end{pmatrix}, \tag{3.31}$$

where we have denoted the matrix of the planar approximant of first order with $A_1(\Delta)$. The stability of the origin is dictated by the eigenvalues of the matrix, which can be expressed in terms of its trace and determinant:

$$\begin{aligned} \operatorname{Tr} A_1(\Delta) &= -2\mu + \varepsilon \Delta_T \omega \\ \det A_1(\Delta) &= \mu^2 + \omega^2 > 0 \\ \lambda_\pm &= \frac{1}{2}\left(\operatorname{Tr} A_1(\Delta) \pm \sqrt{(\operatorname{Tr} A_1(\Delta))^2 - 4 \det A_1(\Delta)}\right). \end{aligned} \tag{3.32}$$

At the critical point, the birth of a stable cycle is signaled by the presence of a pair of purely imaginary eigenvalues. Since the system parameters are real, the condition for this to happen is that the trace must vanish and the determinant be positive. Since $\det A_1(\Delta)$ is positive by construction, the stability of the system is determined entirely by the sign of the trace. By imposing a vanishing trace condition we obtain the expression for the critical delay deviation at first order

$$\Delta_1^* = \frac{2\mu}{\varepsilon\omega}. \tag{3.33}$$

Interestingly we find $\Delta_1^* = \Delta_c$, so that the first order approximant finds the exact same transition point as the adiabatic methods or the self consistent linearization. Analyzing the signs of the eigenvalues under a change of value of the parameters we are able to find two unilaterally unlimited sets on the Δ where the cycle is stable. These are for $\Delta < 2(\mu - \sqrt{\mu^2 + \omega^2})/(\varepsilon\omega)$ and for $\Delta > 2\mu/(\varepsilon\omega)$. One could argue that negative values for Δ could be mapped to positive values near $2\pi/\omega$ due to the the periodicity of the stable orbit but we have not investigated further this line, as it is likely that the other limit is simply an unphysical solution. Remapping (3.33) for delays through the definition of Δ we get

$$\tau_1^* \leq 2\frac{\pi\varepsilon - \mu}{\varepsilon\omega}, \tag{3.34}$$

which is the delay below which we expect a stable orbit to be found.

II order

At the second order the expansion (3.30) reduces to

$$\Delta q = (\omega p - \mu q)\Delta + \frac{\Delta^2}{2}\left(-\omega^2 q - 2\omega\mu p + \omega\varepsilon\Delta q + \mu^2 q\right)$$

Notice that we could also solve this as an equation for Δq, but we are now choosing to neglect the Δq in the expansion as it is a higher order term in Δ_T. The linearized system becomes

$$\begin{pmatrix} \dot q \\ \dot p \end{pmatrix} = \begin{pmatrix} -\mu & \omega \\ -\omega + \varepsilon\left[\frac{\Delta^2}{2}\left(\mu^2 - \omega^2\right) - \mu\Delta\right] & -\mu + \varepsilon\omega\left[\Delta - \mu\Delta^2\right] \end{pmatrix} \begin{pmatrix} q \\ p \end{pmatrix} \equiv A_2(\Delta) \begin{pmatrix} q \\ p \end{pmatrix}. \tag{3.35}$$

The trace and determinant read

$$\begin{aligned} \operatorname{Tr} A_2(\Delta) &= -2\mu + \varepsilon\omega\Delta - \varepsilon\mu\omega\Delta^2 \\ \det A_2(\Delta) &= \left(\mu^2 + \omega^2\right)\left(1 + \frac{\varepsilon\omega\Delta^2}{2}\right) > 0 \end{aligned} \tag{3.36}$$

By the same argument used to obtain (3.33) we can determine this time a segment where a positive real part is obtained

$$\frac{1 - \sqrt{1 - 8\mu^2/\varepsilon\omega}}{2\mu} \le \Delta \le \frac{1 + \sqrt{1 - 8\mu^2/\varepsilon\omega}}{2\mu} \tag{3.37}$$

which for $\mu \ll 1$ can be approximated

$$\frac{2\mu}{\varepsilon\omega} \le \Delta \le \frac{1}{\mu} - \frac{2\mu}{\varepsilon\omega} \tag{3.38}$$

thus recovering the same result that is obtained at first order and via the full solution for the left limit. A comparison of the right limit with that specified by (3.25) may not be meaningful, in particular since for $\mu \ll 1$ we obtain in the perturbative expansion a small denominator. The remarkable fact that both perturbative expansions in the limit of small μ match the value from (3.25) could be interpreted as a piece of evidence that, at least at its onset, the delay induced limit cycle bifurcation is actually a planar phenomenon, regardless of the potentially infinite dimensionality of the full dynamics. We remark though that what has been found in this Section can be considered only a hint, as a full proof of planarity of the transition would require to prove convergence of the planar approximants order by order, for example by an iterative construction of the spectral perturbation to a given order given by the addition of the next one.

3.4 | Connection to the FitzHugh-Nagumo system

While the model proposed in this chapter is not usually considered *per se* as representing any specific physical phenomenon, it was formulated to represent a large class of models in a simplified way. In this section we intend to trace back our steps to the model that inspired this approach, to check to what extent the assumptions that we made on the necessary properties for the transition to be observed are actually met in the original systems. We consider the FitzHugh-Nagumo model for neural excitability, parameterizing time in the fast timescale, and insert a delayed feedback in the fast variable

$$\begin{aligned} \dot{u} &= u - \frac{u^3}{3} - v + J\left(u_\tau - u\right) \\ \dot{v} &= \varepsilon\left(u + a\right), \end{aligned} \tag{3.39}$$

where the parameters a and ε have the usual meaning considered in the rest of this work, respectively of a dynamical parameter and a timescale separation. We use the notation $u_\tau = u(t - \tau)$ for the delayed term and assume that in absence of subscripts the variables are considered at time t. We start by reverting the Liénard transformation [62], we reobtain a second order ODE

$$\ddot{u} - (1 - u^2)\dot{u} + \varepsilon\left(u + a\right) = 0. \tag{3.40}$$

From this form of the equation we recover the close relationship between the FitzHugh-Nagumo model and the Van Der Pol oscillator: indeed the former corresponds to the latter in presence of a constant forcing of magnitude εa, which displaces the fixed point from the origin to $u^* = -a$. We translate the fixed point to the origin and return to a bidimensional system by performing the coordinate transformation

$$x = u + a, \quad y = \dot{x},$$

so to obtain an equation in the centered coordinates

$$\begin{aligned} \dot{x} &= y \\ \dot{y} &= \left(1 - a^2 + 2ax - x^2\right)y - \varepsilon x. \end{aligned} \tag{3.41}$$

It is straightforward to observe that (3.41) admits a stable fixed point in the origin, in the neighbourhood of which its linear approximation has eigenvalues

$$\lambda_\pm = \frac{1}{2}\left(1 - a^2 \pm \sqrt{\left(1 - a^2\right)^2 - 4\varepsilon}\right), \tag{3.42}$$

so that for $|a| > 1$ the fixed point is attractive. The value of ε from this point of view regulates only the spiraling, for $\varepsilon > (1 - a^2)^2/4$, or otherwise overdamped nature of the motion towards the fixed point. From this observation we can draw the conclusion that for a diagonal feedback like the one we are considering, in the spiraling regime we cannot have any stabilization as the system is effectively a damped harmonic oscillator. Nonetheless, let us carry on with the calculation, in order to explore whether at least we can find a quasi invariant orbit by casting the system in normal coordinates. The transformation matrix T mapping the normalized coordinates back to the centered ones can be searched for in the form

$$T = \begin{pmatrix} t & 0 \\ s & t^{-1} \end{pmatrix},$$

as we already observed in the general case. For the FitzHugh-Nagumo neuron, the defining equation of T reads

$$\begin{pmatrix} 0 & 1 \\ -\varepsilon & 1 - a^2 \end{pmatrix} \begin{pmatrix} t & 0 \\ s & t^{-1} \end{pmatrix} = \begin{pmatrix} t & 0 \\ s & t^{-1} \end{pmatrix} \begin{pmatrix} -\mu & \omega \\ -\omega & -\mu \end{pmatrix}, \tag{3.43}$$

where the linear dissipation coefficient μ and the frequency ω are respectively the magnitude of the real part and the imaginary part of the eigenvalues defined in (3.42)

$$\mu = \frac{a^2 - 1}{2}, \quad \omega = \frac{\sqrt{4\varepsilon - (1 - a^2)^2}}{2} \tag{3.44}$$

so that the transformation casts the linear part of (3.41) to the standard form of a damped rotator. Since for the above transformation to be well defined the system eigenvalues in the vicinity of the fixed point must be complex and conjugate, the following discussion will consider only the spiraling case $\varepsilon > (1 - a^2)^2/4$. Solving (3.43) yields the transformation matrix parameters

$$t^2 = \frac{1}{\omega}, \quad s = -\frac{\mu}{\sqrt{\omega}}.$$

As expected, these parameters become singular as the system transitions from the underdamped to the overdamped regime, signaling the failure of the coordinate transformation. When the mapping from the normalized coordinates q, p to the centered coordinates x, y is well defined, it reads

$$\begin{pmatrix} x \\ y \end{pmatrix} = \begin{pmatrix} \omega^{-1/2} & 0 \\ -\mu\omega^{-1/2} & \omega^{1/2} \end{pmatrix} \begin{pmatrix} q \\ p \end{pmatrix}. \tag{3.45}$$

The delayed feedback term in (3.39) translates into (3.41) as a term $J\Pi_y\,(X_\tau - X)$, with

$$\Pi_y = \begin{pmatrix} 0 & 0 \\ 0 & 1 \end{pmatrix}, \quad X = \begin{pmatrix} x \\ y \end{pmatrix},$$

respectively the projector on the y component and the bidimensional vector collecting the two centered coordinates. As the system is moved to Birkhoff coordinates, the linear part of (3.41) is cast to a standard damped rotator and the feedback term is transformed via a standard matrix basis change

$$J\Pi_y\,(X_\tau - X) \mapsto JT^{-1}\Pi_y T\,(Q_\tau - Q) = \begin{pmatrix} 0 & 0 \\ -\mu/\omega & 1 \end{pmatrix} \begin{pmatrix} q_\tau - q \\ p_\tau - p \end{pmatrix},$$

where analogously to the previous notation we have introduced $Q = (q, p)$ for the vector of normalized coordinates. From the form of the y subspace projector in normalized coordinates it is evident that any diagonal y feedback term originally present in the equation is mapped to a mixed term in normal coordinates, of the form that will cause cancellations in the secular equation that forbid the stabilization of the cycle, as observed in Section 3.3.1.
To check for the existence of a quasi invariant orbit, we study the action dynamics, and search for a minimum of the action dissipation. The point of minimum will mark the action value of the quasi invariant circle corresponding to the almost invariant orbit mapped in normal coordinates. To build the averaged Poincaré map in the action variable we write down the full system (3.39) in normal coordinates, in the absence of feedback

$$\begin{aligned} \dot{q} &= \omega p - \mu q \\ \dot{p} &= -\omega q - \mu p + \left(\frac{2aq}{\sqrt{\omega}} - \frac{q^2}{\omega}\right)\left(\sqrt{\omega}p - \frac{\mu q}{\sqrt{\omega}}\right). \end{aligned} \tag{3.46}$$

The equation for the evolution of the action is obtained from this one via a direct calculation, and reads

$$\dot{I} = -2\mu I - \frac{2a\mu}{\omega}q^2p + 2aqp^2 + \frac{\mu}{\omega^{3/2}}q^3p - \frac{q^2p^2}{\sqrt{\omega}}. \tag{3.47}$$

To study the dynamics of the action, and look for a quasi invariant circle we first try to build the Poincaré map in a quasi-adiabatic approximation. The quasi-adiabatic approximation [7] consists in approximating the nonlinear action dissipation on the system orbits with its linear part, on times shorter than the order $\omega\mu^{-1}$, whenever the timescale of the dissipation is much longer than that of the rotation motion, i.e. if $\mu/\omega \ll 1$. We implement the quasi-adiabatic approximation via an *ansatz* for the solution in the form

$$q(t) = \sqrt{2I}e^{-\mu t}\cos\omega t, \quad p(t) = -\sqrt{2I}e^{-\mu t}\sin\omega t,$$

where we can see that the factor $e^{-\mu t}$ implements an exponential shrinking of the areas over one revolution, dominated by the linear part of the system dissipation. We remark that due to the noninvariance of the nonlinear dissipation term in (3.47) under exchange of the coordinates, the rotation direction one chooses in the ansatz for the construction of the map matters. Indeed the rotation must be chosen coherently with what is observed in the full nonlinear system. In our case, the orbits of the original FitzHugh-Nagumo system revolve around the fixed point in a counterclockwise direction, but one must observed that in passing from the $u,\ v$ variables in (3.39) to the centered variables $x,\ y$ in

(3.41) we have reversed the rotation into a clockwise one, so that in normal coordinates we must integrate in a clockwise direction. Furthermore, the choice of the initial condition, i.e. of the Poincaré section, for the construction of the map can yield quantitative, but not qualitative differences in the map itself. For this reason we select, without loss of generality, an initial condition resting on the q axis, due to the better interpretability of the final map expression. Substituting this form for the solution into (3.47) and averaging over a period $T = 2\pi/\omega$, we recover the averaged Poincaré map for the FitzHugh-Nagumo system in the vicinity of its fixed point in a quasi adiabatic approximation

$$\frac{I_{n+1} - I_n}{T} = -\left[2\mu - \frac{12\sqrt{2}a\mu^2}{9\mu^2 + \omega^2} I_n^{1/2} + \frac{8\mu^2 + \omega^2}{2\sqrt{\omega}\left(4\mu^2 + \omega^2\right)} I_n\right] I_n \tag{3.48}$$

$$= -\gamma_I\left(I_n\right) I_n. \tag{3.49}$$

The function γ_I, within square brackets in the first row, is the average action dissipation over one revolution. Treating it as a second-degree polynomial of the square root of the action, to check for the existence of a minimum we must check for the sign of the coefficient multiplying the I term, i.e. the quadratic term with respect to $\sqrt{I}$. This term in the present case is

$$\frac{1}{2}\frac{\partial^2 \gamma_I}{\partial \sqrt{I}^2} = \frac{8\mu^2 + \omega^2}{2\sqrt{\omega}\left(4\mu^2 + \omega^2\right)}, \tag{3.50}$$

which is a real and positive function for positive arguments, so that the quadratic function of the square root is upwards concave and it always has a minimum. Checking that the minimal dissipation value is also positive entails solving a quadratic inequality with quite unwieldy parameters, therefore we check explicitly the shape of the function by evaluating it numerically. We set $\varepsilon = 1$ and using typical values of a we plot γ_I in Figure 3.10. We observe that for all choices of $a > 1$ the γ_I function admits a minimum for positive I, while for the Hopf bifurcation point $a = 1$ the function is a straight line, so that the only minimum coincides with a root in $I = 0$. For the largest choice of a, that is $a = 1.4$, we observe that the function crosses the x axis, a behaviour that in general signals the appearance of an unstable and a stable fixed point, but in this case is due to higher-order effects. To check this we can compute the Poincaré map in the adiabatic approximation, i.e. taking the action to be exactly constant on times of order ω/μ. The map in this approximation coincides at the fixed points with the full Poincaré map of the system, so that any physical closed orbits of the full system would be detected already in this simpler approximation. We implement the adiabatic approximation with the choice of solution

$$q(t) = \sqrt{2I}\sin\omega t, \quad p(t) = \sqrt{2I}\cos\omega t.$$

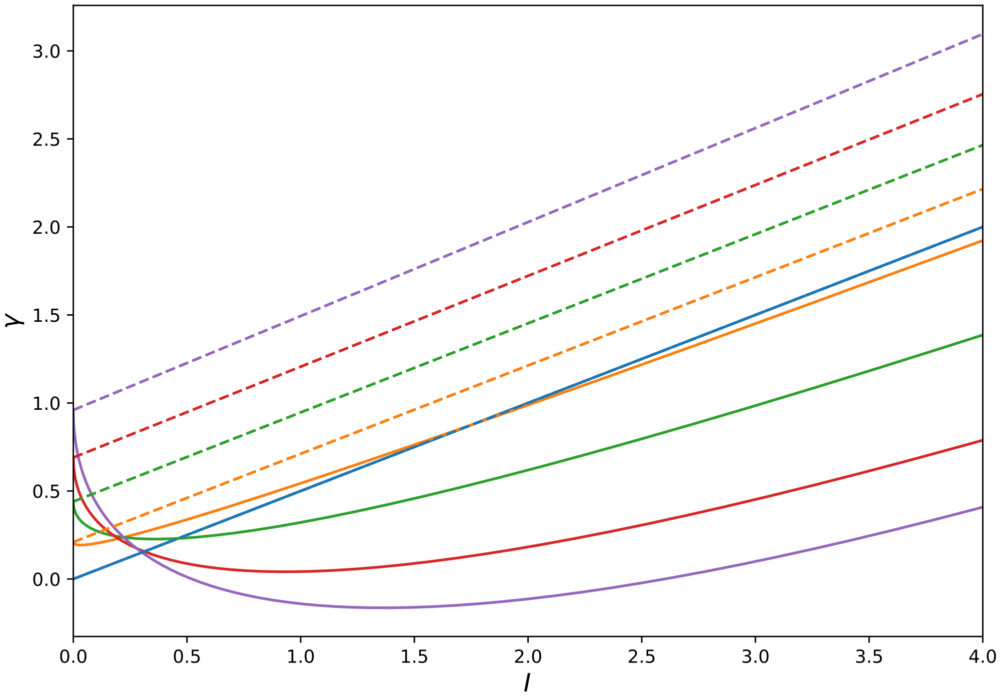

Figure 3.10: Plot of the γ_I^A (dashed lines) and γ_I (solid lines) functions for some typical values of the dynamical parameter a, $a = 1$ (blue), $a = 1.1$ (orange), $a = 1.2$ (green), $a = 1.3$ (red) and $a = 1.4$ (purple). The timescale separation is fixed at $\varepsilon = 1$ throughout to ensure the well-posedness of transformation (3.45).

Substituting it into (3.47) and averaging over a period $T = 2\pi/\omega$ we get the map

$$\frac{I_{n+1} - I_n}{T} = -\left(2\mu + \frac{1}{2\sqrt{\omega}} I_n\right) I_n = -I_n \gamma(I_n)_I^A, \tag{3.51}$$

so that isolating the nonlinear dissipation function $\gamma_I^A(I)$ that multiplies $-I_n$ in the adiabatic approximation it reads

$$\gamma_I^A(I) = 2\mu + \frac{1}{2\sqrt{\omega}} I \tag{3.52}$$

which has the shape of a straight line and is always positive, so that no minimum of the dissipation exists, apart from the origin. If the roots of γ_I, observed in Fig. 3.10 for $a = 1.4$ were physical, they should also be roots of γ_I^A, but the latter function admits none, except for the degenerate case $a = 1$, where the two approximations coincide. From this comparison, and from numerical simulations, we conclude that for larger values of a higher order terms become more relevant and introduce unphysical equilibria in (3.48), yet leave the convexity unmodified.

Since for values of $a \approx 1.3$ the dissipation function γ_I appears to have a well defined minimum for a positive I, we check qualitatively with simulations whether a skew feedback is able to stabilize a cycle, in the underdamped regime with $\varepsilon > (1 - a^2)^2/4$. We consider the equation

$$\begin{aligned} \varepsilon \dot{u} &= u - \frac{u^3}{3} - v + J\,(v_\tau - v) \\ \dot{v} &= u + a, \end{aligned} \tag{3.53}$$

which differs from (3.39) only in the coupling scheme. The initial condition, a function $(u_0(t), v_0(t)) : [-\tau, 0] \to \mathbb{R}^2$, in this case is provided in the shape of a Gaussian pulse centered on the fixed point, in the form

$$\begin{aligned} u_0(t) &= -a \\ v_0(t) &= \frac{a^3}{3} - a + \frac{A}{\sqrt{2\pi}\sigma} e^{-(t-\tau/2)^2/\sigma^2}, \end{aligned}$$

Performing some simulations with $a = 1.3$, $\varepsilon = 0.5$, $\tau = 4.5$, $J = 1$, $\sigma = 5 \times 10^{-2}$, two examples of which are represented in 3.11, we can observe that depending on the magnitude of A we can either end up on a limit cycle or back on the fixed point, a behaviour corresponding to that observed in the simplified model (3.10) in Fig.3.3. An important difference with respect to the simplified model, although, is that the limit cycle in (3.53) does not wrap around the fixed point, a feature that carries over to the system in the overdamped regime as we have extensively observed in the previous chapter.

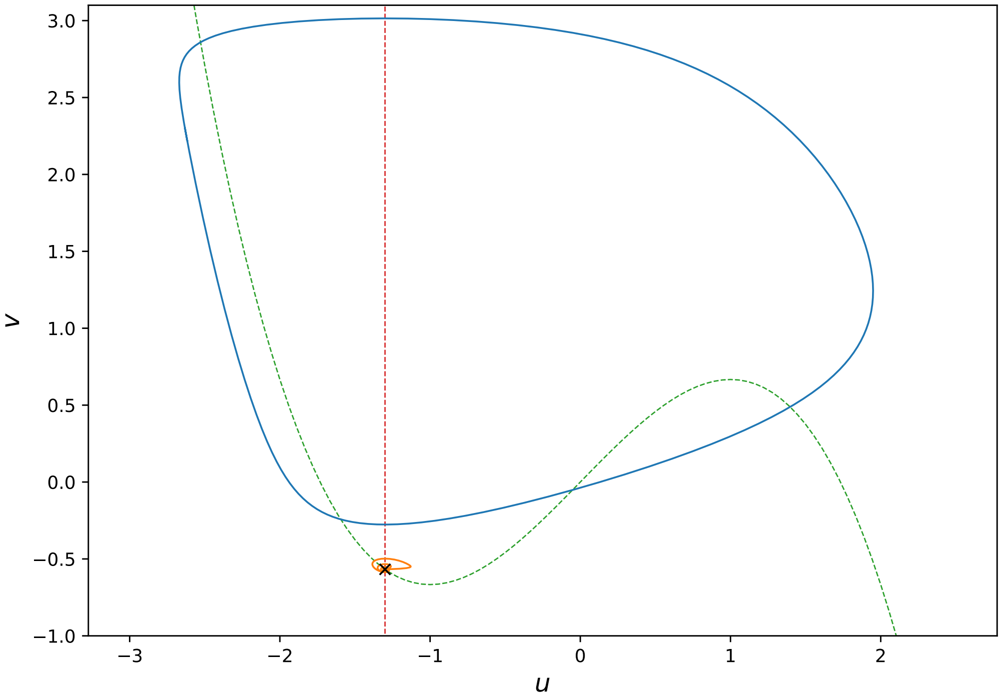

Figure 3.11: Two trajectories for the FitzHugh-Nagumo system with skew delayed feedback. Limit cycle (blue line) obtained for a magnitude of the initial pulse $A = 1$, dissipative orbit (orange) for a magnitude $A = 10^{-1}$. The remaining parameters were set to $\varepsilon = 0.5,\ a = 1.3,\ J = 1,\ \tau = 4.5$. Width of the initial pulse $\sigma = 5 \times 10^{-2}$. The dashed lines are the nullclines of the u variable (green) and v variable (red).

3.5 | Connection to networked systems

Since in the previous chapter we introduced Delay Differential Equations as effective models for directed loops of dynamical systems, we would like to trace back our steps to that setting, in order to find out what dynamical behaviours can emerge when we consider a directed loop of simplified systems. In particular we concern ourselves with the types of state that can emerge in a chain of systems like (3.10), and their similarity to stationary states of the DDE. We consider the system

$$\begin{aligned}\dot{q}_n &= \omega p_n - \gamma(q_n, p_n) q_n \\ \dot{p}_n &= -\omega q_n - \gamma(q_n, p_n) p_n + \varepsilon\left(q_{n-1} - q_n\right),\end{aligned} \tag{3.54}$$

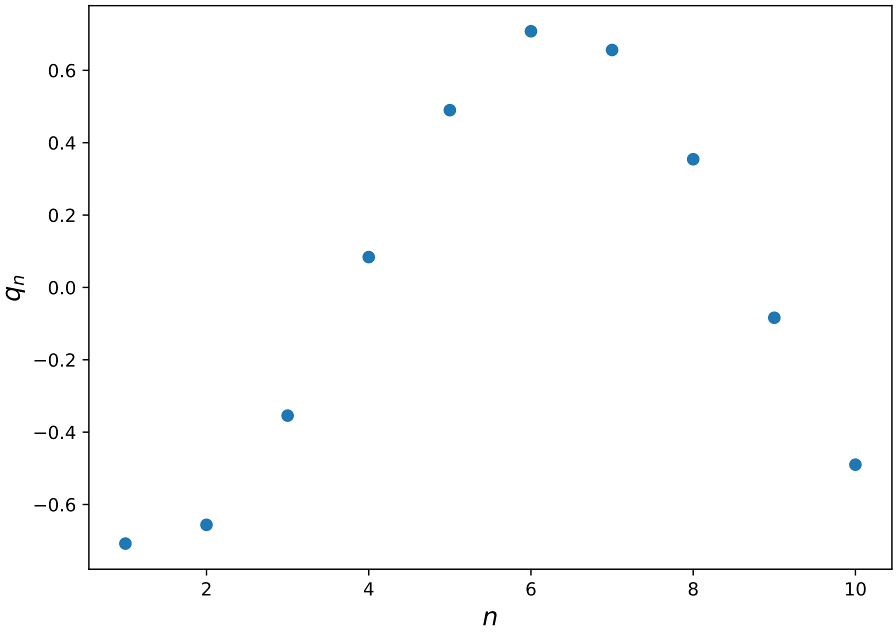

Figure 3.12: Oscillating stationary state for the nonlinear oscillators chain. For each oscillator only the q variable is displayed. Single system parameters were taken to be identical between different nodes, and set to $\omega = 1$, $\mu = 10^{-2}$, $\varepsilon = 10^{-1}$. The chain size is $N = 10$.

where the nonlinear dissipation depends only on the node's dynamical variables through the action, in the usual form

$$\gamma(q_n, p_n) = \mu + \left(\frac{q_n^2 + p_n^2}{2} - \bar{I}\right)^2 ,$$

and the index n runs from 1 to N, the size of the system, and we identify $N + 1 = 1$, implementing periodic boundary conditions. By performing simulations, we see that such a system can express stationary states analogous to those of the simplified nonlinear oscillator (3.10) with delay. For example, considering a chain of $N = 10$ nodes, we can see that an oscillating stationary state exists, of which we display a snapshot in Fig. 3.12. Plotting the coordinates of all the chain nodes at the same time in phase space, we get Fig. 3.13, showing that the systems likely interpolate the trajectory of a DDE, analogously to what was seen in the previous chapter for the FitzHugh-Nagumo unidirectional chain. An important difference with the FitzHugh-Nagumo chain rests in the

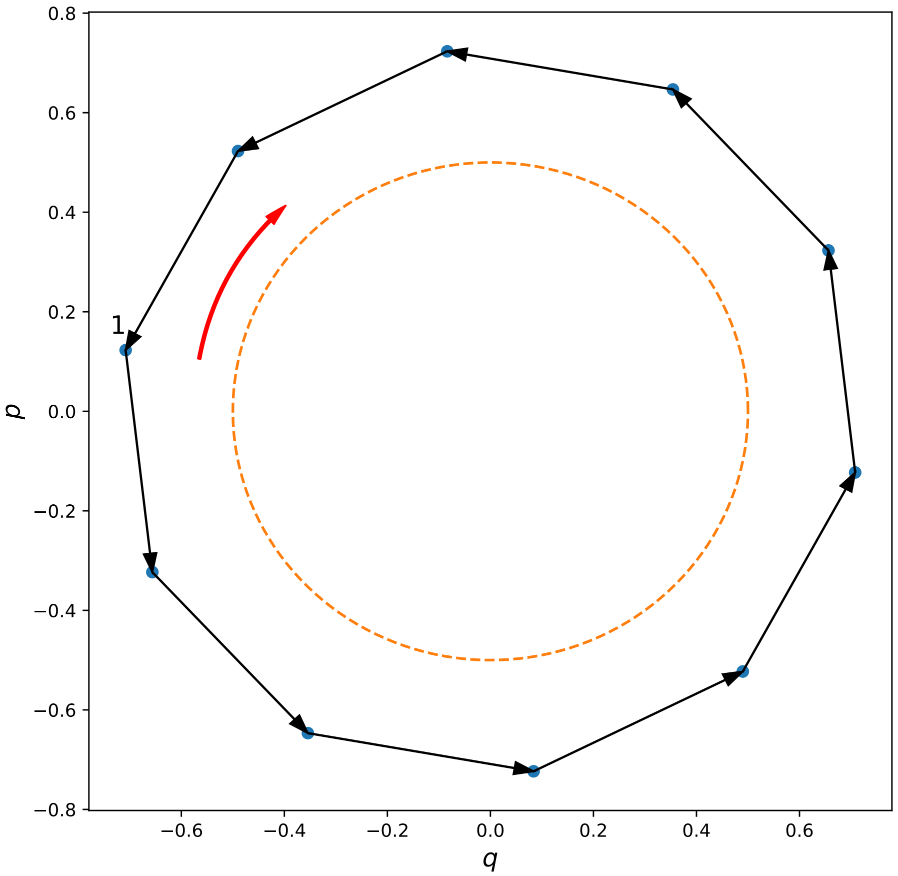

Figure 3.13: Depiction in phase space of the states of the nodes of the nonlinear oscillator chain for the same collective state and system parameters of Fig. 3.12. The black arrows mark the directionality of couplings, pointing from the driver to the driven node, the number one marks chain site number 1, to allow comparisons with Fig. 3.12. The red arrow points in the systems rotation direction. The dashed orange circle marks the quasi invariant circle for the node dynamics.

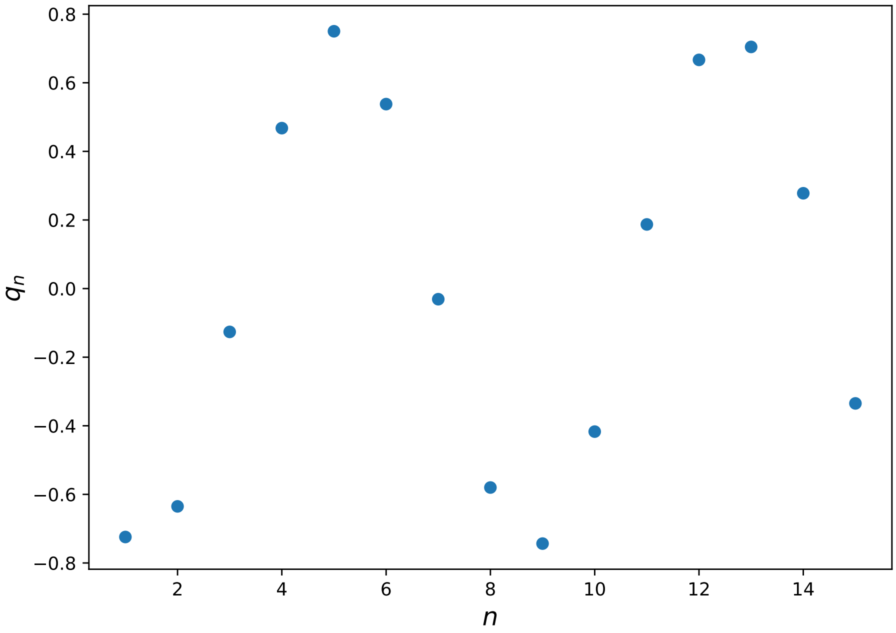

Figure 3.14: Snapshot of the chain for the same single node parameters of 3.12. The chain size has been changed to $N = 15$, so that the system displays 2 oscillations along the whole chain.

fact that while the neurons have no natural period, so that a scaling of the solution period $T \propto N$ is observed, the simplified nonlinear oscillators have one. This means that considering the same choice of single system parameters of Figures 3.12 and 3.13 but changing the number of nodes we expect to observe compromise stationary states displaying different numbers of full oscillations along the length of the chain. Some examples of this behaviour are displayed in Figures 3.14 and 3.15. From the performed simulations, we expect the number of oscillations to be determined by an interaction of the single systems properties and the chain size, although further investigation is required to determine this analytically. In addition, more complicated states including long transients and beats have been observed and require further study, in particular in regard to their link to states of the delayed system.

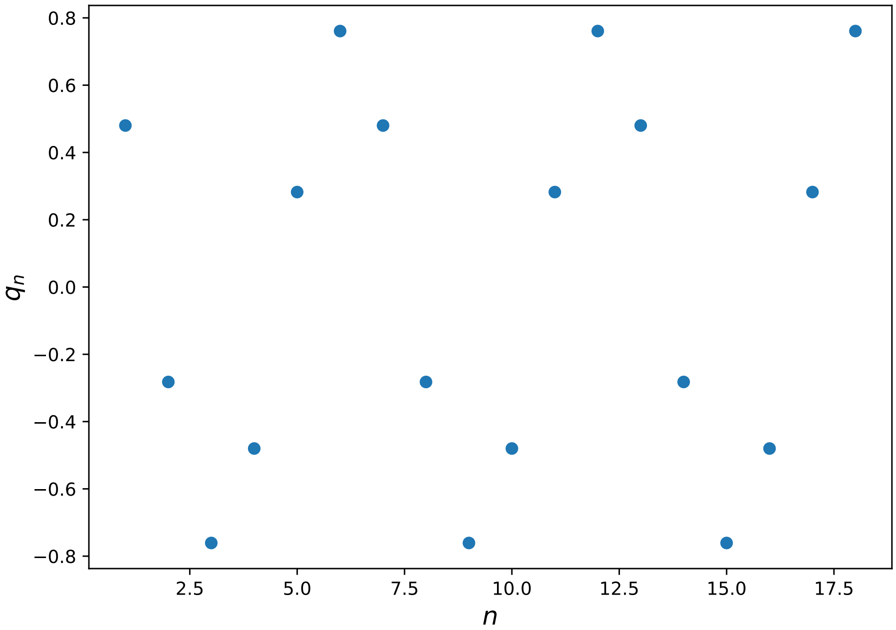

FIGURE 3.15: Snapshot of the chain for the same single node parameters of 3.12. The chain size has been changed to $N = 18$, so that the system displays 3 oscillations along the whole chain.

3.6 | Conclusion

In this chapter we have formulated a simplified model to capture the essential features of delay induced saddle point bifurcations of limit cycles. By working with a normal coordinate model in standard form we are able to address a great number of problems with a unified approach, as our model essentially represents a whole class of systems that exhibit quasi invariant orbits, i.e. have a one dimensional locus in phase space that is privileged during the system's time evolution. Indeed, provided that a system of such features can be set in normal coordinates, it will reduce into the system we have considered at least in the vicinity of the quasi invariant manifold. From this point of view the proposed model could be regarded in itself as a normal form for the limit cycle stabilizing transition. A necessary condition is formulated with respect to the feedback coupling scheme, which is required to be skew, i.e. to mix the coordinates, since diagonal feedbacks are shown not be able to stabilize the quasi invariant orbit due to cancellations. The bifurcation diagram is drawn using an averaging argument to approximate the location of attractors thanks to an ansatz on the shape of the stable solutions. Furthermore, constructing planar approximations to the full delayed dynamics, we are able to show that at the two lowest perturbative orders the stabilization transition is planar, so that no role is played by the infinite dimensionality of the system, a typical behaviour of complex systems, observed ubiquitously in applications. Retracing the steps to the original problem of the stabilization of an orbit in the FitzHugh-Nagumo system, we show that the system possesses a quasi invariant orbit by building the dissipation function for its averaged Poincaré map in normal coordinates, so that despite being unable to explicitly construct normal coordinates for the $\varepsilon \ll 1$ case, we suppose that the underlying mechanism should be the same as that we are able to observe explicitly in a case with ε not too small and for a skew feedback. In particular we conjecture that the necessary skewness is introduced during the transformation to a set of normal coordinates centered within the limit cycle of the $\varepsilon \ll 1$ case, through a variable change which is generally different from the standard one considered in the chapter. Finally, we show that in a unidirectional chain of such simplified systems, states can exist that are reminiscent of the correspondent DDE. Despite this, in the chain system, also more complex states are observed, requiring a more careful examination.

Possible prosecutions of this research would mainly entail extending this analysis to systems that do not express an intrinsic oscillatory dynamics, but are very close to doing so in the sense that a minimal periodic perturbation can create one. These systems have a strong dependence of the expressed period on the feedback delay, like in the excitable FitzHugh-Nagumo neuron, and cover many examples relevant in Complex Systems Physics. From a more technical point of view, a relevant step will be the more careful analysis of the pseudo-elliptical ansatz used to construct the averaged Poincaré map, in order to determine the dependence of the pseudoeccentricity on the system parameters, possibly through an approach based on the comparison of equivalent Poincaré maps. In the perturbative treatment, a full proof of planarity would require to extend our considerations, which were made at the first two orders, to an arbitrary order of perturbation, which generally can be attained via a recursive or inductive approach. A full comprehension of the unidirectional chain dynamics should go through the independent analytical characterization of the system, so that an explicit comparison of the solutions and of the bifurcations can be performed, in particular with regard to the mentioned complicated states observed in the extended system.

Appendices

3.7 | Generality of the skewness condition

In the chapter we have stated that in system (3.10) the feedback term can be taken to feed $q_\tau - q$ into p without loss of generality. We show in this appendix that choosing a skew coupling with $p_\tau - p$ feeding into q produces an analogous bifurcation. Let us consider, in analogy with (3.10), the following DDE

$$\begin{aligned} \dot{q} &= \omega p - \gamma(q,p)q + \varepsilon\left(p_\tau - p\right) \\ \dot{p} &= -\omega q - \gamma(q,p)p, \end{aligned} \tag{3.55}$$

where the nonlinear dissipation γ is taken in the same form of (3.10).In a neighbourhood of $\bar{I}$ the system reduces to a linear one

$$\begin{aligned} \dot{q} &= \omega p - \mu q + \varepsilon\left(p_\tau - p\right) \\ \dot{p} &= -\omega q - \mu p, \end{aligned} \tag{3.56}$$

so that we can study its local stability properties with a self-consistent secular equation, which we write by looking for a solution to (3.56) in an exponential form and imposing a vanishing determinant. We get

$$\begin{aligned} \det\left(\lambda I - A(\lambda)\right) &= \det\begin{pmatrix} \lambda + \mu & -\omega - \varepsilon\left(e^{\lambda(t-\tau)} - 1\right) \\ \omega & \lambda + \mu \end{pmatrix} \\ &= \lambda^2 + 2\mu\lambda + \mu^2 + \omega^2 + \varepsilon\omega\left(e^{-\lambda\tau} - 1\right) = 0. \end{aligned} \tag{3.57}$$

Setting $\lambda = i\Omega$ at the bifurcation point, and separating into real and imaginary part we get

$$\begin{aligned} \frac{\omega^2 + \mu^2 - \Omega^2}{\varepsilon\omega} &= 1 - \cos\Omega\tau \\ 2\mu\Omega &= \varepsilon\omega \sin\Omega\tau . \end{aligned} \tag{3.58}$$

We introduce the delay advancement consistently with what was done in Sec. 3.3.1in order to compare straightforwardly the two results.

$$\Omega\tau = 2\pi - \Omega\Delta,$$

The previous equations become

$$\begin{aligned} \frac{\omega^2 + \mu^2 - \Omega^2}{\varepsilon\omega} &= 1 - \cos\Omega\Delta \\ 2\mu\Omega &= -\varepsilon\omega \sin\Omega\Delta. \end{aligned} \tag{3.59}$$

Expanding at leading order we find the critical values

$$\Delta_{c(p)} = -\frac{2\mu}{\varepsilon\omega} \tag{3.60}$$

$$\Omega^2_{c(p)} = \frac{\omega^2 + \mu^2}{1 + 2\mu^2/\varepsilon\omega}. \tag{3.61}$$

A comparison with those obtained in Sec. 3.3.1 shows the relationship

$$\begin{aligned} \Delta_{c(p)} &= -\Delta_c \\ \Omega^2_{c(p)} &= \frac{\varepsilon\omega - 2\mu^2}{\varepsilon\omega + 2\mu^2}\Omega^2_c , \end{aligned}$$

so that we can map one bifurcation into the other with a reversal of the coupling strength $\varepsilon \rightarrow -\varepsilon$.

4 | Inter-spike time and firing rate estimates for a noisy FitzHugh-Nagumo neuron

4.1 | Introduction

The available models for neural excitability are mainly formulated in terms of highly nonlinear differential equations [46, 48] or nonlinear maps [87], in order to replicate the rich and complicated behaviour of membrane potentials in neural cells. Despite being unavoidable, this nonlinearity can make such models quite difficult to study and interpret, especially when they are considered in a networked context, which is the natural setting required by neuroscientific applications. Furthermore, whenever one is considering real world applications, or the effect of randomly fluctuating inputs, a degree of stochasticity has to be included in the model, which can have a highly nontrivial interplay with the nonlinear dynamics. Considering in particular the FitzHugh-Nagumo neuron, which so far has been our model of reference for neural phenomena, the inclusion of noise collocates the problem in the branch of stochastic analysis concerned with the study of stochastic slow-fast systems. This matter has been investigated in recent years due to its wide range of applications, that spans further than neural systems into problems from solid state physics and climatology, with some important formal contributions given in [12, 13], and a specific approach to the FitzHugh-Nagumo neuron [14]. The results in the first two works apply to the FitzHugh-Nagumo neuron in a qualitative sense, so that depending on the temperature value two phases are distinguished, of rare versus frequent firing. In [14], a topological approach is formulated, based on the number of windings that the orbit completes around the fixed point between two firing events. In neither case an inter-event time distribution is derived, which is the first aim of the present chapter.

We derive an expression for the inter-event time distribution based on an adaptation of Kramers escape rate theory to systems with an event-triggered slow modulation of the potential wells. While the approach is derived from first principles, the expression is found to match simulation values only upon regression on the rate parameter, supposedly due to the emergence of correlations as a side effect of the interdependence between the evolution of the two variables. The relevance of this distribution rests in the fact that, together with its average, i.e. the reciprocal of the firing rate, it represents one of the most easily measurable quantities in actual neuroscientific measurement campaigns. The second problem addressed in this chapter is the formulation of a simplified discrete model that can reliably reproduce the statistics of a noisy FitzHugh-Nagumo neuron. This is done by interpolating discretely the rate function obtained by the previous analysis and turning it into a suitable transition probability for a binary system with states interpreted as firing or non-firing events. We then develop a minimal coupling scheme to allow the implementation of dynamical networks, and discuss its applicability. The latter is in principle the end goal of the whole chapter, as the formulation of a simple and interpretable yet realistic model for dynamical neural networks can pave the way to new theoretical and numerical approaches to information theoretical investigation of neural phenomena at the micro and mesoscale. Indeed, despite some contributions [51, 84], even the core concept of channel capacity remains to be fully elucidated with respect to neural communication mechanisms, especially if one tries to move beyond a purely descriptive statistical point of view, an important step in the exploration of neural encoding strategies.

4.2 | The Stochastic FitzHugh-Nagumo model

We consider a FitzHugh-Nagumo neuron under the effect of an additive white noise

$$\begin{aligned} \dot{u} &= u - \frac{u^3}{3} - v + \sqrt{2T}\xi \\ \dot{v} &= \varepsilon(u + a) \end{aligned} \tag{4.1}$$

with ξ a white noise with zero mean and autocorrelation given by

$$\langle \xi(t)\xi(t+\tau)\rangle = \delta(\tau),$$

u the fast variable, v the slow variable and a a dynamical parameter. The separation of timescales is determined by the factor ε which specifies that the evolution timescale of the slow variable is ε^{-1} times slower than that of the fast one. Notice that (4.1) as it is written, corresponds to a unit choice for time where the fast dynamics is observed on a scale $\mathcal{O}(1)$ and the slow one on a scale

$\mathcal{O}(\varepsilon^{-1})$. For this reason, (4.1) will be referred to as the equation in the *fast time*. In order to find the correct transformation to slow time units, i.e. such that u evolves in time $\mathcal{O}(\varepsilon)$ and v in time $\mathcal{O}(1)$, we first write down (4.1) in the form of a Stochastic Differential Equation

$$\begin{aligned} \mathrm{d}u &= \left(u - \frac{u^3}{3} - v\right) \mathrm{d}t + \sqrt{2T}\,\mathrm{d}W_t \\ \mathrm{d}v &= (u + a)\,\varepsilon \mathrm{d}t, \end{aligned} \tag{4.2}$$

where the separation between the stochastic and deterministic terms is made more clear, and $\mathrm{d}W_t$ is the differential of a Wiener process, i.e. an uncorrelated Gaussian random noise with mean and variance given by

$$\langle \mathrm{d}W_t \rangle = 0, \quad \langle \mathrm{d}W_t^2 \rangle = \mathrm{d}t.$$

so that the overall variance of the noise term will be $2T\mathrm{d}t$, which has the same order ε^0 of the deterministic evolution of the variable to which it is applied. When one performs the scaling $t \mapsto \varepsilon^{-1}t$, to pass from fast to slow time units, the naif transformation of (4.2) would be

$$\begin{aligned} \mathrm{d}u &= \left(u - \frac{u^3}{3} - v\right) \frac{\mathrm{d}t}{\varepsilon} + \frac{\sqrt{2T}}{\varepsilon}\mathrm{d}W_t \\ \mathrm{d}v &= (u + a)\,\mathrm{d}t, \end{aligned} \tag{4.3}$$

but this would yield a scaling of the overall variance $2T\varepsilon^{-2}\mathrm{d}t$. For consistency therefore the temperature must be scaled according to $T \mapsto \varepsilon T$ when one switches time scale. The overall scaling therefore reads

$$\begin{aligned} t &\mapsto \varepsilon^{-1}t \\ T &\mapsto \varepsilon T, \end{aligned} \tag{4.4}$$

For ease of usage we can also map back this scaling on the original equation with the white noise (4.1), obtaining

$$\begin{aligned} \varepsilon\dot{u} &= u - \frac{u^3}{3} - v + \sqrt{2\varepsilon T}\xi \\ \dot{v} &= u + a, \end{aligned} \tag{4.5}$$

which will be referred to as the equation in *slow time*. Regardless of the chosen time scale, the equation admits a fixed point at $T = 0$ in $(u^*, v^*) = (-a, a^3/3 - a)$, which is stable for $|a| > 1$ and unstable for $|a| < 1$, since at the point $|a| = 1$ the system undergoes a Hopf bifurcation. Through the usage of a stochastic Runge-Kutta method of order 4 we can simulate the system (4.1) and compute several quantities of interest. The most relevant in real-world neuroscientific field measurements is the inter-spike interval (ISI) distribution, i.e. the probability distribution of the time elapsed between subsequent firings of the neuron. An equivalent quantity, more common in physics, would be the firing rate, i.e. the rate with which units transition from the quiescent to the firing state, which clearly corresponds to the inverse of the ISI, at least on average. As it can be expected, running simulations for different values (Fig.4.1) of temperature we can see that higher temperatures correspond to higher rates, and correspondingly lower ISI. The relationship between the rate and the temperature is not trivial though, because for very high temperatures the rates begins to grow more and more slowly, representing the point at which the noise starts to interact with the refractoriness of the system.

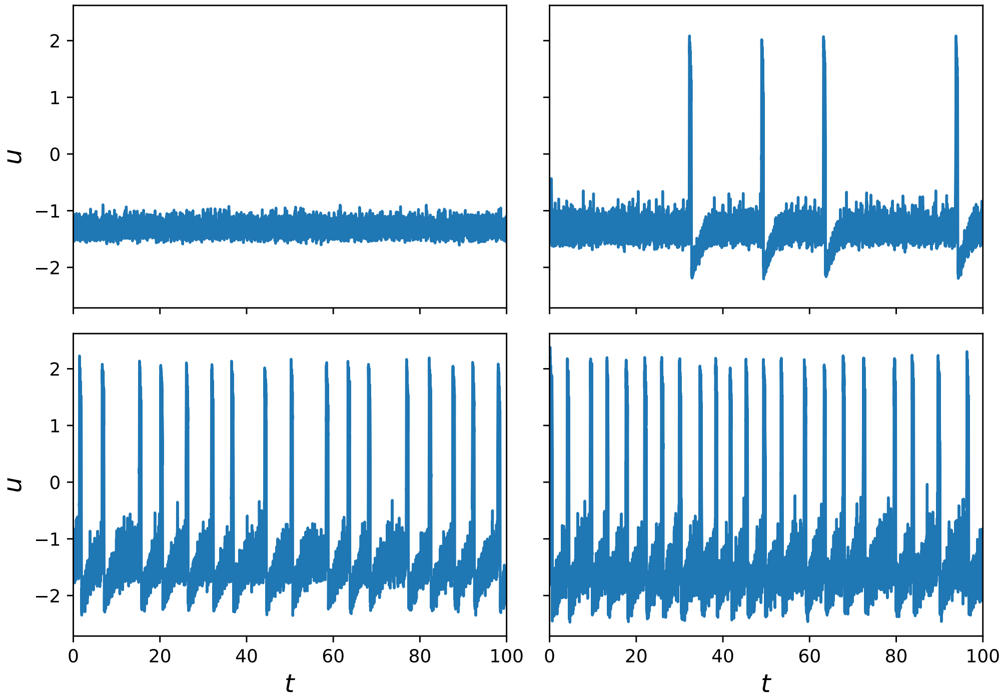

Figure 4.1: Time series of the u variable for the noisy FitzHugh-Nagumo neuron (4.5). Noise temperatures are set to the following values from top to bottom and from left to right: $T = 5 \times 10^{-3}$, $T = 10^{-2}$, $T = 2.5 \times 10^{-2}$, $T = 5 \times 10^{-2}$. The other parameters are set to $a = 1.3$, $\varepsilon = 10^{-2}$.

4.3 | Estimation of the firing rate and of the Interspike Interval distributions

To try and understand analytically the dependence of the firing rate on the system temperature, we try to approach the problem using the framework of the Kramers escape rate problem [55]. Such framework is concerned with analytically estimating the rate with which a particle trapped on one side of a generic double well potential and subject to a white noise, will jump to the other well, or more precisely with the estimation of the current with which an ensemble of point particles injected into one of the wells transitions to the other under the action of the noise.
A generic unidimensional Smoluchowski equation for a particle moving overdampedly under the effect of a potential $V(x)$ and an uncorrelated white noise ξ with temperature T reads

$$\dot{x} = -\frac{\mathrm{d}V}{\mathrm{d}x} + \sqrt{2T}\xi, \tag{4.6}$$

where x denotes the position of the particle. The Kramers problem can be formulated e.g. if we take $V(x)$ in the shape

$$V(x) = \frac{ax^4}{4} + \frac{bx^3}{3} - \frac{cx^2}{2},$$

which is a classical asymmetrical double well potential, which becomes symmetrical for $b = 0$. In general it admits three critical points

$$x_\pm = \frac{-b \pm \sqrt{b^2 + 4c}}{2}, \qquad x_0 = 0,$$

where $x_\pm$ are stable equilibrium points for the dynamics (4.6) and x_0 is an unstable point marking the maximum of the potential barrier separating the two wells. Let us consider an ensemble of particles with dynamics ruled by (4.6), that are inserted in the system in the vicinity of x_- at thermal equilibrium. The Kramers formula for the average rate at which they will cross over to x_+ is given by

$$k_{-\to+} = \frac{\omega_0\omega_-}{2\pi} e^{-\beta\Delta V}, \tag{4.7}$$

where $\beta = 1/T$ is the usual inverse of the temperature used in Statistical Physics, ΔV is the height of the potential barrier

$$\Delta V = V(x_0) - V(x_-),$$

and ω_-, ω_0 are the values of the potential function curvature at x_- and x_0, i.e.

$$\omega_- = \sqrt{\left|\frac{\mathrm{d}^2V}{\mathrm{d}x^2}(x_-)\right|}, \quad \omega_0 = \sqrt{\left|\frac{\mathrm{d}^2V}{\mathrm{d}x^2}(x_0)\right|}, \quad \frac{\mathrm{d}^2V}{\mathrm{d}x^2} = 3ax^2 + 3bx - c.$$

From (4.7) we understand that the Kramers approach provides a correction based on the curvature of the potential at the critical points to the exponential Arrhenius factor. The transition rate is exponentially suppressed by the barrier height, with respect to which the temperature acts as a scaling, so that transition is facilitated for higher temperatures.

4.3.1 | Kramers approach for a frozen FitzHugh Nagumo neuron

Our first step towards an approach based on Kramers theory to the FitzHugh-Nagumo neuron will be the study of the fast dynamics of a unit in the $\varepsilon \to 0$ limit. By considering the equation in fast time (4.1), and taking the limit we obtain the following Smoluchowski equation

$$\dot{u} = u - \frac{u^3}{3} - v + \sqrt{2T}\xi, \tag{4.8}$$

where it is important to notice that the equation for the v dynamics in (4.1) becomes just $\dot{v} = 0$ in the limit, and so v enters (4.8) not as a dynamical variable but as a parameter, its value needing to be fixed a priori, possibly depending on the point during the full system (4.1) orbit at which the limit is considered to be taken. In (4.8) we can interpret the force term as originating from a unidimensional potential that reads

$$V_1(u;v) = \frac{u^4}{12} - \frac{u^2}{2} + vu, \tag{4.9}$$

plotted in Fig. 4.2, with a purely parametric dependence on v, so that in no circumstance it can be considered a potential for the full system. Nonetheless, these considerations allow us to treat the fast dynamics of the neuron in the limit of an infinitely slow v dynamics, as that of a point particle in a double well defined by potential (4.9) under the action of a noise. We refer to this system in the $\varepsilon \to 0$ as to the *frozen* neuron, as we are effectively freezing the slow dynamics and only considering the effects of noise on the fast one.
By setting $v = v^*$ we are studying, up to the effect of the slow dynamics that we would have for positive ε, the mean escape rate for a FitzHugh-Nagumo neuron resting at the fixed point in presence of noise. Notice that this is a

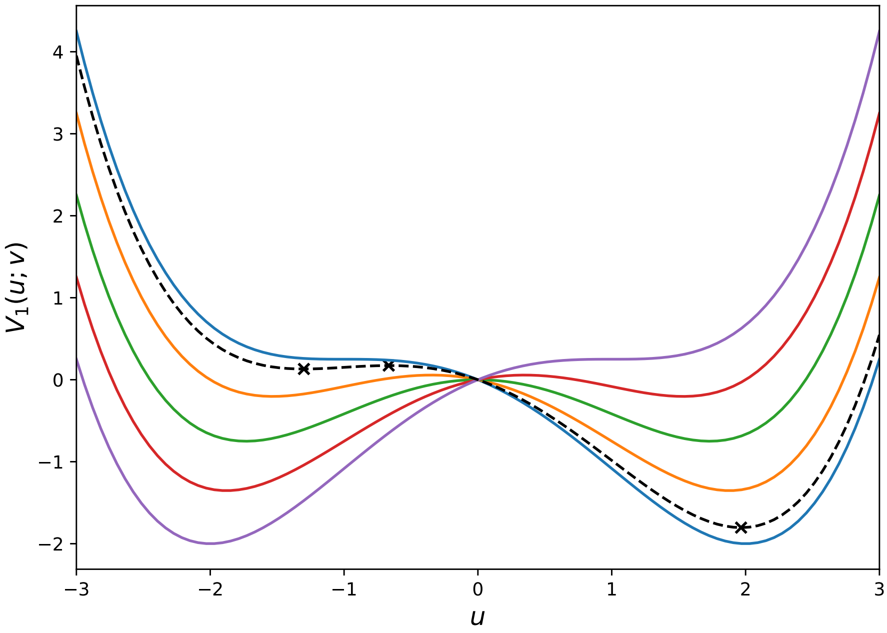

FIGURE 4.2: Potential for the fast variable dynamics at fixed values of $v = -2/3$ (blue), $v = -1/3$ (orange), $v = 0$ (green), $v = 1/3$ (red), $v = 2/3$ (purple). Dashed line is for v^*. Crosses mark potential values at the critical points for $v = v^*$, from left to right u_-, u_0, u_+.

different quantity with respect to the firing rate of the full unit that we aim to compute, as the former quantity refers to the activation rate for a single neuron under the action of noise, i.e. accounts for the full firing dynamics and refractoriness of the neuron, while in the frozen case we are considering an ensemble of noisy neurons resting in the vicinity of the fixed point, which represents the physiological resting state. From a different perspective, if we want to look at the frozen system as to a single neuron, we could view it as a neuron that is immediately reset to the physiological resting state as soon as it fires, skipping the refractoriness and the whole action potential dynamics. Keeping these considerations in mind, we can write straightforwardly the Kramers rate expression for the frozen neuron at the fixed point. The search for the critical points of $V_1(u;v)$ requires the solution of the cubic equation

$$\frac{\partial V_1}{\partial u} = \frac{u^3}{3} - u + v = 0, \tag{4.10}$$

which can be written via the Cardanic formulae or the Viète trigonometric form.

The critical points of (4.7) have then in general a parametric dependence on the value of v. Due to the form of the problem, we notice that equation (4.10) for the critical points of the potential is equivalent to the defining equation of the full system's (4.1) u nullcline, so that the value of v assumes the meaning of the ordinate at which a horizontal line intersects the nullcline, individuating 1, 2 or 3 intersection points. In particular, since in the present case we are considering the neuron at the fixed point, we are considering $v = v^* = a^3/3 - a$, so that the critical point u_-, i.e. the potential minimum of the left well, coincides by construction with the full system's global fixed point, allowing us to factor it out and find the two additional fixed points through the solution of a quadratic equation, ending up with

$$u_- = -a, \quad u_0 = \frac{a}{2} - \sqrt{3}\sqrt{1 - \frac{a^2}{4}}, \quad u_+ = \frac{a}{2} + \sqrt{3}\sqrt{1 - \frac{a^2}{4}}. \tag{4.11}$$

Analogously, the left well depth is in general a function of v

$$\Delta V_1(v) = V_1(u_0(v)) - V_1(u_-(v)), \tag{4.12}$$

that with the choice of $v = v^*$ becomes a function only of the system's dynamical parameter a

$$\Delta V_1^*(a) = \Delta V_1(v^*(a)) = \frac{3}{8}a^4 - \frac{3}{4}a^2 - \frac{1}{8}\left(a^3 - 4a\right)\sqrt{12 - 3a^2} - \frac{3}{4}. \tag{4.13}$$

If we expand the potential $V_1(u, v)$ in the vicinity of a generic equilibrium point u_{eq} we get

$$V(u) = V(u_{eq}) + \frac{1}{2}(u_{eq}^2 - 1)(u - u_{eq})^2 + \mathcal{O}\left((u - u_{eq})^3\right),$$

so that equilibria with $\left|u_{eq}\right| < 1$ are maxima of V_1 and thus unstable, and equilibria with $\left|u_{eq}\right| > 1$ are stable. From this expression we can obtain the general form for the potential's curvature at an equilibrium point, which is

$$\omega(u_{eq}) = \sqrt{\left|u_{eq}^2 - 1\right|}. \tag{4.14}$$

At this point we have all the necessary elements to write down (4.7) for the frozen FitzHugh-Nagumo neuron in the vicinity of the fixed point, which gives

$$\sigma(a, T) = \frac{\omega_0(a)\omega_-(a)}{2\pi} e^{-\beta \Delta V_1^*(a)}, \tag{4.15}$$

where the explicit values of the curvatures are given by

$$\omega_- = \sqrt{a^2 - 1}, \qquad \omega_0 = \sqrt{\left| 2 - \sqrt{3}\sqrt{1 - \frac{a^2}{4}}a - \frac{a^2}{2} \right|}. \tag{4.16}$$

We can already test (4.15) with simulations, provided we take into account in the simulation setup of the features of the approximation in which we are working. Using a Runge-Kutta algorithm of order 4 adapted to Stochastic Differential Equations, we simulate equation (4.8) for particles with initial conditions drawn according to the equilibrium Boltzmann distribution in the left well

$$u(0) \propto \exp\Big(-\beta\omega_-^2(u(0) - u_-)^2/2\Big).$$

For each temperature value we integrate the equation several times, in an event based approach, stopping the integration once a certain target value is reached, signalling exit from the left well. The target value is set on the right inflexion point of the potential, i.e. at $u = 1$, where the slope is maximal, and thus the probability of re-crossing the barrier backwards at the next timestep minimal, in order to minimize miscounts. Moreover, a maximum time of integration is set in order to avoid infinite loops, corresponding to the minimal rate measurable in the experiment. The results are collected in Figure 4.3. A very good accord is observed roughly until $T = 2.5 \times 10^{-2}$. Above this value the theoretical value remains well within the error bars at all times, but larger deviations are observed. Another quantity of interest in this type of system is the inter-event time, or Inter-Spike Interval for neurons. For the frozen system this is distributed according to an exponential distribution, as is typical for Poisson processes of constant rate, i.e. following

$$\rho(t, \beta) = \sigma(\beta)e^{-\sigma(\beta)t}, \tag{4.17}$$

which has its maximum in $t = 0$, i.e. immediately after the system has fired, which is an expected unphysical aspect with respect to the full FitzHugh-Nagumo system, as we are neglecting the part of the dynamics responsible for the refractoriness.

4.3.2 | Dependence on the time of last firing as an adiabatic potential modulation

Comparing the frozen system Kramers rate with the full system simulation data in Fig.4.4, we find a mismatch, indeed the theoretical rate for the frozen system in general overestimates the one obtained via numerical experiments.

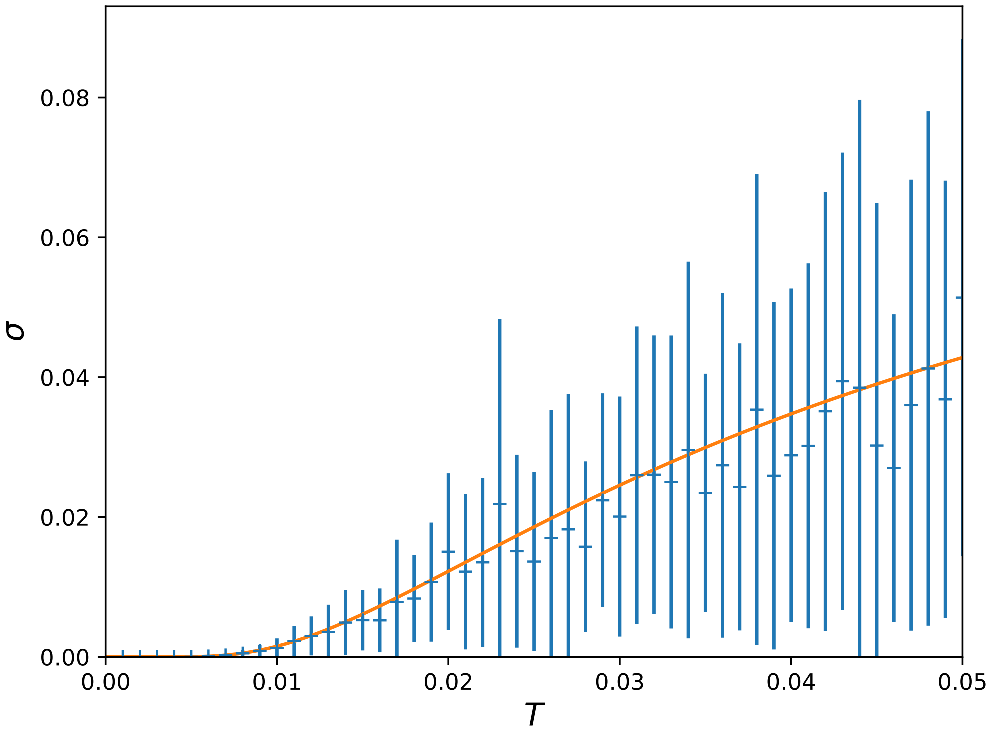

Figure 4.3: Escape rate, measured in fast time, for the FitzHugh-Nagumo neuron at the global fixed point in the limit $\varepsilon \to 0$. The system dynamical parameter was set at $a = 1.3$. For each value of T the escape time was averaged over 50 measurements, error bars mark the standard deviation, showing a relevant amount of fluctuations for higher rates. The orange line is the Kramers prediction given by (4.15).

This is expected, since as the temperature is increased, the frozen system has no impediment in decreasing the time between firing events, which follows the exponential distribution typical of a Poisson process. This is not the case in the full FitzHugh-Nagumo system, where the full dynamics implements a refractoriness that suppresses too short interspike times. In this sense we can say that in the full system the rate at which the neuron fires, or equivalently the mean escape time, has a dependence on the time that has elapsed since the last activation. Starting from this intuition we intend to build towards a more suited form for the inter event time distribution, by accounting for the full system dynamics as a slow modulation of the well parameters. From this distribution it is then possible in principle to obtain the mean escape time, which is the reciprocal of the rate, as its average value.

To gain some insight into ways of modelling the full system dynamics role in

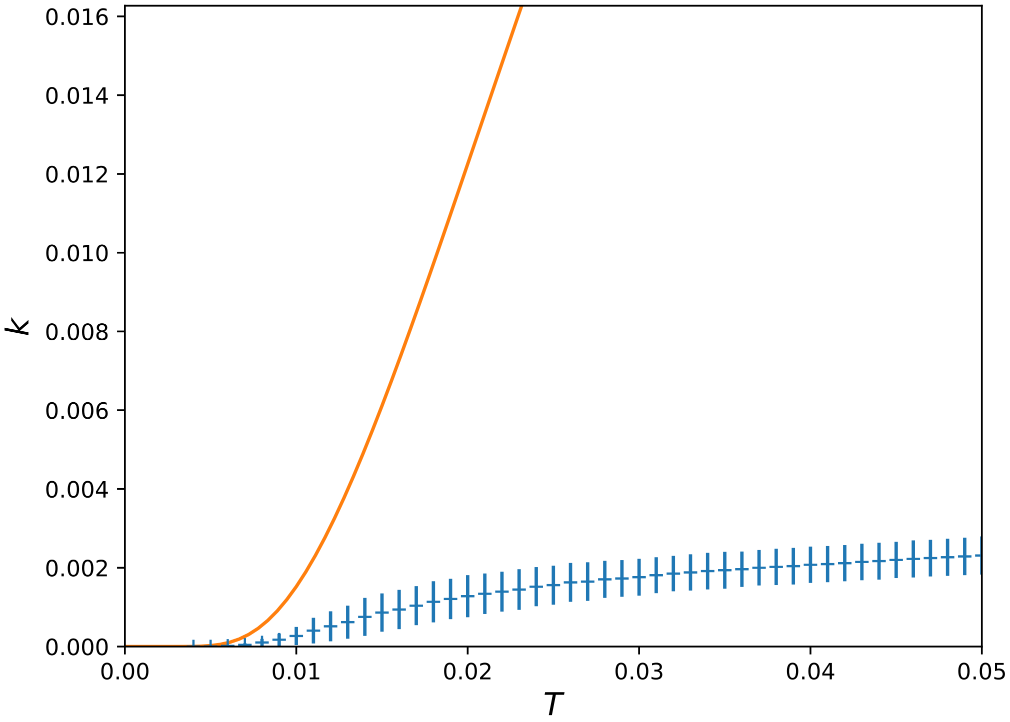

FIGURE 4.4: Firing rate in fast time for the full system (4.1) as a function of the temperature. The rate is measured by evolving the system for 2.5×10^4 time units and calculating the reciprocal of the average inter-spike time. Error bars are obtained by propagating the standard deviation of the inter-spike time on the firing rate calculated from its average. The orange line marks the same Kramers prediction of Fig.(4.3).

influencing the noise-induced activation rate, it is a good idea to consider the system in the slow timescale and in the $\varepsilon \to 0$ limit. We start by casting (4.1) into slow time via the scaling (4.4), which yields

$$\begin{aligned} \varepsilon\dot{u} &= u - \frac{u^3}{3} - v + \sqrt{2\varepsilon T}\,\xi \\ \dot{v} &= u + a. \end{aligned} \tag{4.18}$$

In the limit $\varepsilon \to 0$ the first equation becomes an algebraic equation, which plays the role of a constraint that links u and v at any given time during the system evolution. We get therefore a Differential Algebraic Equation (DAE), that reads

$$\begin{aligned} v &= u - \frac{u^3}{3} \\ \dot{v} &= u + a. \end{aligned} \tag{4.19}$$

Since the inversion of the algebraic equation in (4.19) is not in general a uniquely defined operation, as $u(v)$ can take up to three values depending on the choice of v, we can reduce the DAE to an ODE only by confining the problem on a single branch of the cubic nullcline. We can do this in terms of any of the two dynamical variables, choosing u we get

$$\dot{u} = \frac{u + a}{1 - u^2}, \tag{4.20}$$

while if we choose v we must parameterize the cubic equation solutions. We can do this using Viète's trigonometric form, from which we obtain

$$\dot{v} = 2\cos\left[\frac{1}{3}\arccos\left(-\frac{3v}{2}\right) - \frac{2\pi k}{3}\right] + a \quad \text{with}\, k = 0,\ 1,\ 2, \tag{4.21}$$

and choosing the value of k selects the branch of the cubic on which we are considering the motion to take place, going from right to left for growing k. Let us consider a system as it has just jumped away from the fixed point, in the limit it will be on the right branch of the u nullcline, at a location $(u_-(v^*), v^*)$. At this point, the system starts climbing the right branch on a solution to either (4.20) or equivalently (4.21) with $k = 0$. Once the value $v = 2/3$ is reached, corresponding to the right maximum of the u nullcline, the coalescence and subsequent disappearance of roots $u_0(v)$, $u_+(v)$ leaves only $(u_-(2/3),\ 2/3)$ as an admissible location for the system, so that the system jumps back to the left branch of the u nullcline, through a discontinuity in the solution in the $\varepsilon \to 0$ limit or in a time $\mathcal{O}(\varepsilon)$ to a vicinity of the point for $0 < \varepsilon \ll 1$. Once the system is on the left nullcline branch, it resumes moving on a solution

to (4.20) or (4.21) with $k = 2$ towards the global fixed point. If we assume these considerations to hold sufficiently accurately also for $0 < \varepsilon \ll 1$, we expect to be able to model the effect of the slow dynamics on the firing rate as a slow variation of v in the Kramers rate expression, noticeable on times $\mathcal{O}\left(\varepsilon^{-1}\right)$ in the fast timescale. Since the firing event is defined as a jump from the left to the right nullcline branch, or equivalently from the left to right well of $V_1(u; v)$, during the time spent traversing the right branch we set the transition probability to 0.
We write in general the v dependent Kramers rate as

$$k(v) = \Pi(v)A(v), \tag{4.22}$$

with

$$\Pi(v) = \frac{\omega_0(v)\omega_-(v)}{2\pi}, \quad A(v) = e^{-\beta\Delta V_1(v)}, \tag{4.23}$$

which are respectively the Kramers curvature-dependent correction prefactor and the exponential Arrhenius factor for a certain value of v. The two terms play quite a different role in the definition of the Kramers rate. The value of the Arrhenius factor $A(v)$ is dependent on the product of the depth of the left potential well $\Delta V_1(v)$ and the inverse temperature β so that the typical scales on which Kramers escape rate theory is considered to be reliable are those for which $\beta\Delta V > 1$, in order to consider small rates. From this consideration, and plotting the potential well depth $\Delta V_1(v)$ in Fig.4.5, we see that the β range for which we expect to obtain a reasonable result in a neighbourhood of the fixed point, starts around $\beta \geq 10$ if we are considering values of a in the range $1 < a < \sqrt{3}$ so to have values of $v^* < 0$ and an attractive fixed point. These features reflect in the plots of $A(v)$, which shows an almost exponential decreasing trend for increasing v, with a rate proportional to β, so that for β not too small the activation of the neuron is exponentially suppressed proportionally to the vertical distance from the fixed point $v - v^*$. On the other hand $\Pi(v)$ is by construction a limited concave function, defined on the $[-2/3, 2/3]$ interval, plotted in Fig.4.7. Its two roles in this context can be interpreted as a correction which becomes relevant in the vicinity of the fixed point on the one hand, and a cutoff that suppresses the transition rate for values of v for which the two wells of the potential are not defined in the first place, i.e. for $v \notin]-2/3, 2/3[$.

Supported by these considerations, we approximate linearly (4.22) in the neighbourhood of v^*, obtaining

$$k(\Delta v) = \Pi(v^*) \exp\left(-\beta\Delta V_1(v^*) - \beta \left.\frac{\mathrm{d}V_1}{\mathrm{d}v}\right|_{v^*} \Delta v\right), \tag{4.24}$$

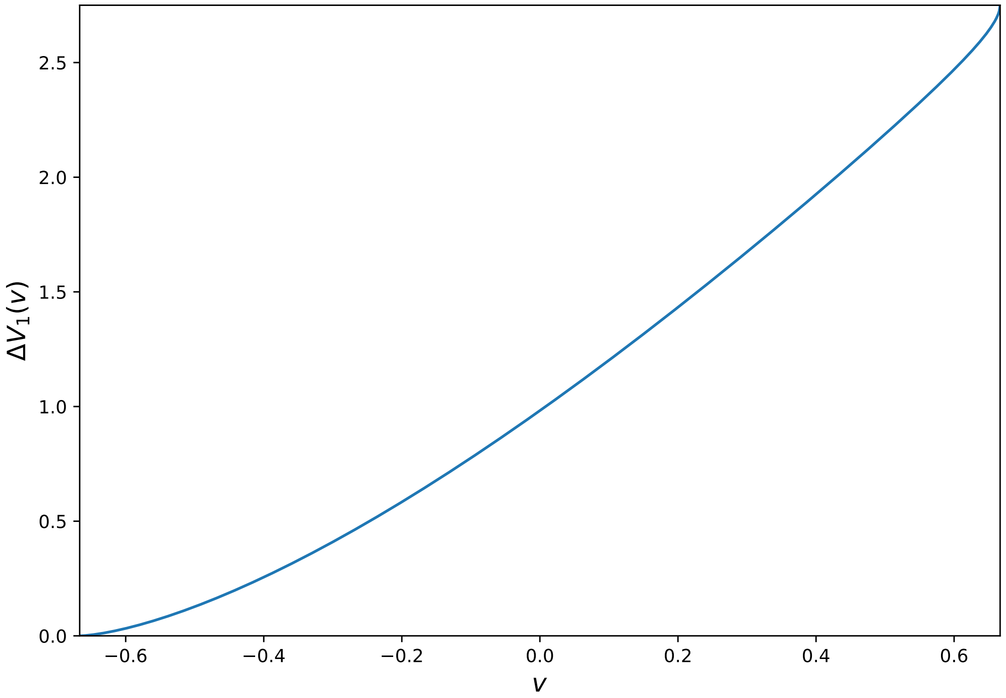

FIGURE 4.5: Plot of the left well depth $\Delta V_1(v)$ as a function of the slow variable v.

where we have set $\Delta v = v - v^*$ the vertical distance to the fixed point and the prefactor has not been expanded since its role becomes relevant only near the fixed point, being exponentially suppressed by the Arrhenius factor elsewhere, and due to its concave shape, because of which a linear approximation near the fixed point would rapidly loose accuracy with Δv. The total derivative of the well depth with respect to v expands to

$$\begin{aligned} \left.\frac{\mathrm{d}\Delta V_1}{\mathrm{d}v}\right|_{v^*} &= \frac{\mathrm{d}}{\mathrm{d}v}\left.\Big[V_1(u_0;v) - V_1(u_-;v)\Big]\right|_{v^*} \\ &= \left.\frac{\partial V_1}{\partial u}\right|_{u_0,v^*}\left.\frac{\partial u_0}{\partial v}\right|_{v^*} - \left.\frac{\partial V_1}{\partial u}\right|_{u_-,v^*}\left.\frac{\partial u_-}{\partial v}\right|_{v^*} + \left.\frac{\partial V_1}{\partial v}\right|_{u_0,v*} - \left.\frac{\partial V_1}{\partial v}\right|_{u_-,v^*} \\ &= u_0(v^*) - u_-(v^*), \end{aligned} \tag{4.25}$$

where the first two terms in the second row vanish at the fixed point, since u_0 and u_- are by construction critical points of the potential. Interestingly we get a term which is proportional to the well spatial width, intended as the distance between the bottom of the well and the top of the barrier separating the two wells. Therefore we have derived for the v dependent rate in the vicinity of the

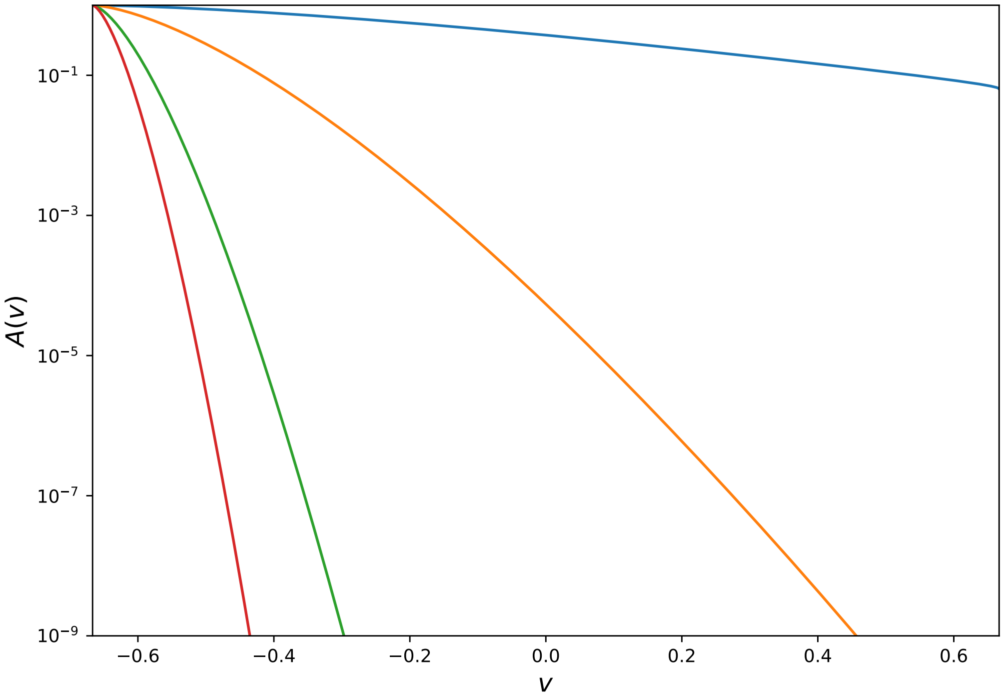

FIGURE 4.6: Plot of the $A(v)$ Arrhenius factor for the FitzHugh-Nagumo system for several values of $\beta = 1$ (blue), $\beta = 10$ (orange), $\beta = 50$ (green) and $\beta = 100$ (red). $A(v)$ values are in a logarithmic scale.

global fixed point the following approximation

$$k(\Delta v) = \sigma\ (\beta)\, e^{-\beta \Delta u \Delta v}, \tag{4.26}$$

where we denoted $\Delta u = u_0(v^*) - u_-(v^*)$ the well width and indicated with σ the rate for the frozen system, as defined in (4.15). To recover the evolution of k over time, in terms of the time since the last activation of the neuron, we must specify now the value of Δv as a function of time. In principle both (4.20) and (4.21) are integrable by separation of variables, but their solutions cannot be inverted and cast as $u(t)$ or $v(t)$, so that their explicit solutions have little use for our purposes. On the other hand, due to the aforementioned exponential suppression of the rate away from the fixed point, we expect the actual dynamics of v to matter only in the vicinity of $v*$. Additionally, the Hartman-Grobman theorem [34, 41] grants that in the vicinity of a hyperbolic fixed point, the orbits a system of nonlinear differential equations are qualitatively equivalent to those of a linear one, which is mapped to the former up to a nonlinear transformation of coordinates. Assuming that the part of the v trajectory that is relevant

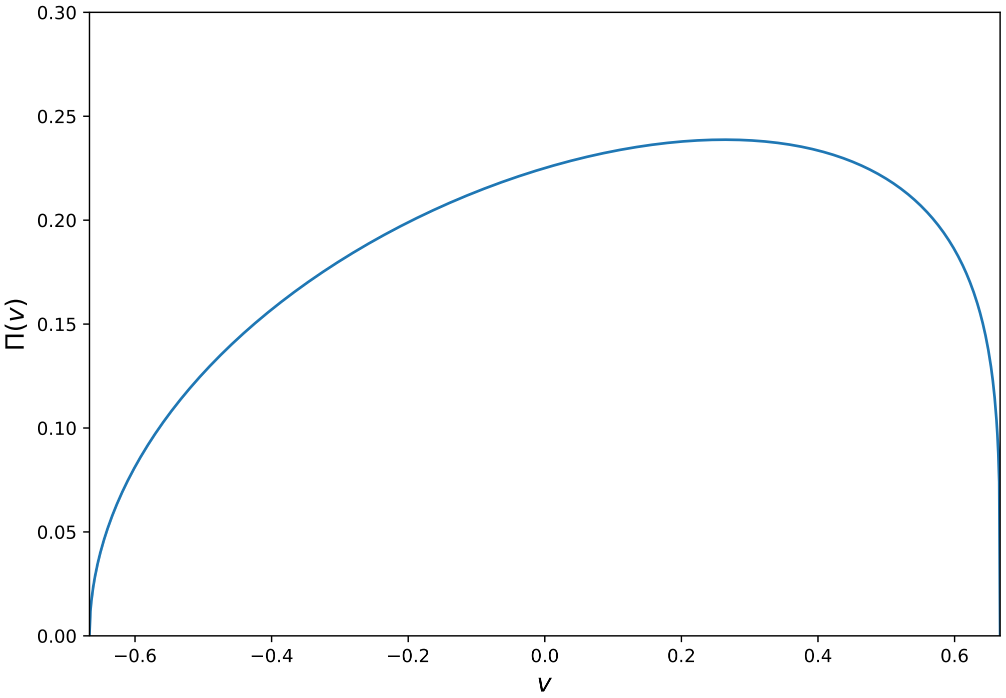

Figure 4.7: Plot of the $\Pi(v)$ function for the FitzHugh-Nagumo system.

for our problem lies in the neighbourhood where the theorem applies, we can reduce the dynamics to its linearization near the fixed point. The linearized dynamics in terms of the displacement $\Delta v = v - v^*$ is given by the v dynamics equation for the FitzHugh-Nagumo neuron, which in fast time reads

$$\frac{\mathrm{d}\Delta v}{\mathrm{d}t} = \varepsilon\,(u + a)\,, \tag{4.27}$$

which can be expressed as follows by approximating the motion as constrained on the nullcline (i.e. in a limit $\varepsilon \to 0$)

$$\frac{\mathrm{d}\Delta v}{\mathrm{d}t} = \varepsilon\,(u - u_-(v^*)) = \varepsilon\,\left.\frac{\mathrm{d}u}{\mathrm{d}v}\right|_{\varepsilon\to 0} \Delta v, \tag{4.28}$$

where the derivative of u with respect to v on the nullcline $\mathrm{d}u/\mathrm{d}v|_{\varepsilon\to 0}$ can be obtained by deriving implicitly with respect to v the algebraic equation in (4.19). Eventually one gets

$$\frac{\mathrm{d}\Delta v}{\mathrm{d}t} = \frac{\varepsilon\Delta v}{1 - a^2}, \tag{4.29}$$

which is solved by the exponential trajectory

$$\Delta v(t) = \Delta v_0 e^{-\varepsilon\lambda t}, \tag{4.30}$$

where we denote $\lambda = 1/(a^2 - 1)$ the trend of the exponential up to a factor ε which makes the trend correctly vanishes in the $\varepsilon \to 0$ limit, and $0 < \Delta v_0 \leq 2/3 - v^*$ the initial condition on the v displacement at the instant at which we begin to approximate the system as a slowly modulated double well. In this respect several choices can be made, of which we will discuss a few. Setting $\Delta v_0 = 2/3 - v^*$ amounts to treating the system as a slowly modulated double well for the whole extent of its motion on the left branch of the nullcline, after having treated the motion on the right branch as well described by the system in the limit $\varepsilon \to 0$, i.e. by the differential algebraic noiseless system (4.19). This would introduce in principle a discontinuity in the rate function, that jumps from an identical 0 during the motion on the right branch to an exponentially small but positive value on the left. Furthermore, in this approach we are neglecting the possible effect of the noise in accelerating the return to the left nullcline branch with respect to the description obtained in the $\varepsilon \to 0$ limit, in a sense over determining the system with respect to the effects of noise. Another possible choice is to carry Δv_0 into the exponent as a term $\tau_0 = \log \Delta v_0$, letting it assume the role of a time translation used as a free parameter to be estimated from data through a regression procedure. This choice has the side effect of yielding very small yet positive firing rates even for $t = 0$, i.e. for the time of the preceding activation itself, which in principle is unphysical, but can be considered still a very good approximation since the unphysical rates are exponentially low. Another drawback of this choice is that, despite allowing us to fit the distribution of interevent times, by definition it does not allow us to build a rate function as a function of the temperature for the full FitzHugh-Nagumo system, unless we find a way to fit τ_0 independently of the choice of temperature. The advantage of this more phenomenological choice, though, is to make fewer assumptions on the dynamics on the right branch and of the transition from the right to the left branch in presence of noise, which is a desirable feature. We will proceed in the following with the second choice.

In light of the previously elucidated findings we can write the firing rate in function of the time t since the last activation of the neuron

$$k(t, \beta) = \sigma(\beta) \exp\Big(-e^{-\varepsilon\lambda t + \tau}\Big), \tag{4.31}$$

where we have introduced

$$\tau = \tau_0 + \tau_1, \quad \tau_0 = \log \Delta v_0, \quad \tau_1 = \log \beta \Delta u. \tag{4.32}$$

so to explicitly separate the time translation component that must be fitted τ_0 from that which we know from first principles τ_1. The functional form of (4.31) takes the name of *Gompertz curve* and can be considered as a logistic curve with varying slope. To simplify the expression we approximate it by bringing the outermost exponential to denominator and expanding it in a power series to first order, obtaining

$$k(t,\beta) = \frac{\sigma(\beta)}{1+e^{-\varepsilon\lambda t+\tau}} = \frac{\sigma(\beta)}{2}\left[1+\tanh\frac{1}{2}(\varepsilon\lambda t-\tau)\right], \tag{4.33}$$

which as expected approximates the shape between the two plateaus in the much simpler form of a hyperbolic tangent, see Fig. 4.8 for a comparison.

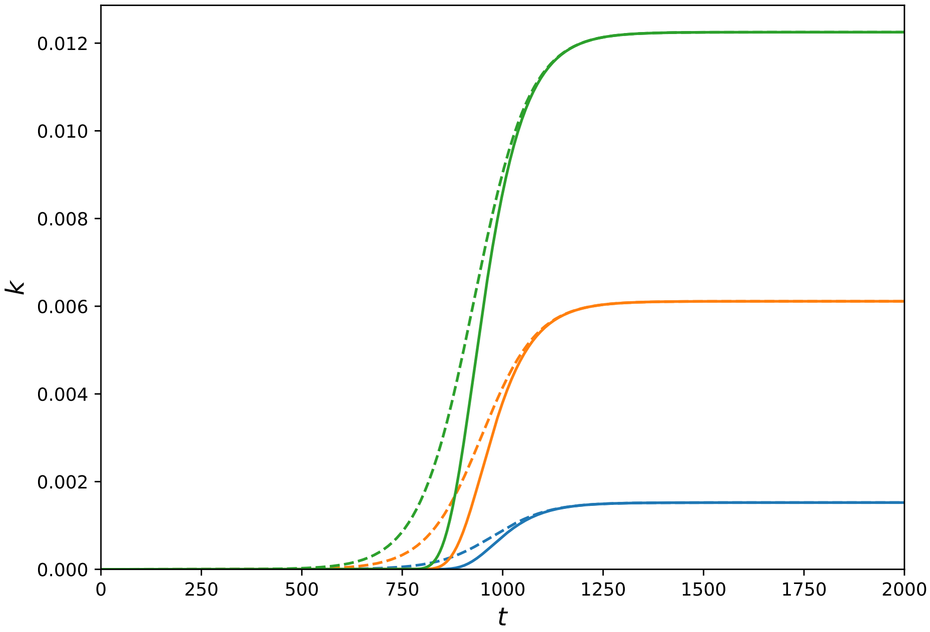

FIGURE 4.8: Comparison of the full Gompertzian curves (solid lines) and the approximated logistic curves (dashed lines) for $T = 1\times10^{-2}$ (blue), $T = 1.5\times10^{-2}$ (orange) and $T = 2\times10^{-2}$ (green). The value of the regression parameter has been set to $\tau_0 = 0$ for plotting. The dynamical parameter was set to $a = 1.3$. Time is expressed in the fast time scale.

Expression (4.33), once τ_0 is provided, gives an approximation to the firing probability per unit time of a FitzHugh-Nagumo neuron, a time t after its preceding activation. This is in principle not a simple function to measure in experiments or simulations as operatively it defines the number of neurons per unit time that fire after a time t after having fired at time 0, over an infinite population where each neuron that fires is immediately removed from the population. A much more practical and useful time is the Inter-Spike Interval (ISI) distribution $\rho(t, \beta)$, i.e. the probability density of measuring a certain time t between two neural spikes produced by the cell. Such a quantity can be related to the rate $k(t, \beta)$ by introducing the negative cumulative function of the ISI distribution

$$\bar{F}(t, \beta) = \int_t^\infty \mathrm{d}t' \rho(t', \beta). \tag{4.34}$$

Indeed by discretizing the $[0, t]$ interval into N parts of equal duration t/N we can write an N-dependent approximation $\bar{F}_N$ to the negative cumulative as

$$\bar{F}_N(t, \beta) = \prod_{n=0}^{N} \left(1 - \frac{nt}{N} k\left(nt/N, \beta\right)\right). \tag{4.35}$$

By taking logarithms on both sides we get

$$\begin{aligned} \log \bar{F}_N(t, \beta) &= \sum_{n=0}^{N} \log \left(1 - \frac{nt}{N} k\left(nt/N, \beta\right)\right) \\ &\approx - \sum_{n=0}^{N} \frac{nt}{N} k\left(nt/N, \beta\right), \end{aligned} \tag{4.36}$$

where we have expanded $\log(1 - x) \approx -x$. In the limit $N \longrightarrow \infty$ we expect that $\bar{F}_N$ will tend to $\bar{F}$, and by definition of Riemann integral we can transform the summation into an integral, getting

$$\log \bar{F}(t, \beta) = \lim_{N \to \infty} \log \bar{F}_N(t, \beta) = - \int_0^t \mathrm{d}t' k(t', \beta). \tag{4.37}$$

Integrating and exponentiating the result we get the negative cumulative function

$$\bar{F}(t, \beta) = \exp\left(- \int_0^t \mathrm{d}t' k(t', \beta)\right) = \cosh^{\frac{\sigma}{\varepsilon\lambda}}\left(\tau/2\right) \frac{e^{-\frac{\sigma}{2}t}}{\cosh^{\frac{\sigma}{\varepsilon\lambda}} \frac{1}{2}\left(\varepsilon\lambda t - \tau\right)}. \tag{4.38}$$

The ISI probability density function is by definition the derivative of (4.38) with respect to time, with a sign reversal

$$\rho(t, \beta) = -\frac{\partial \bar{F}}{\partial t} = \frac{\sigma}{2} \cosh^{\frac{\sigma}{\varepsilon\lambda}}\left(\tau/2\right) \frac{e^{-\frac{\sigma}{2}t}\left(1 + \tanh \frac{1}{2}\left(\varepsilon\lambda t - \tau\right)\right)}{\cosh^{\frac{\sigma}{\varepsilon\lambda}} \frac{1}{2}\left(\varepsilon\lambda t - \tau\right)}. \tag{4.39}$$

To ensure that ρ is well defined as a continuous probability measure we must check for normalization over its domain $[0, \infty[$. We can verify this easily through the limits of $\bar{F}$, which are

$$\lim_{t\to 0} \bar{F}(t, \beta) = 1, \quad \lim_{t\to\infty} \bar{F}(t, \beta) = 0,$$

thus ensuring the correct normalization of ρ. The shape of (4.39) correctly reflects the properties we expect from a neuron in presence of noise, as firing is suppressed for small t values by the hyperbolic tangent. A peak is then reached, marking the modal firing time, and for large times we can approximate the full expression to

$$\rho(t, \beta) \approx \rho^{\infty}(t, \beta) = (2\cosh(\tau/2))^{\frac{\sigma}{\varepsilon\lambda}} \; \sigma e^{-\sigma t + \frac{\sigma\tau}{2\varepsilon\lambda}} \approx \sigma e^{-\sigma\left(t - \frac{\tau}{\varepsilon\lambda}\right)}, \qquad (4.40)$$

in which the last approximation holds for $\tau \ll 1$. The information carried by this expression is that once the refractoriness has faded, the neuron is essentially well approximated again by the frozen system, and ρ recovers the Poisson process exponential distribution up to a scaling factor.

We make a consideration on timescales before proceeding, since up to now we have worked in the fast timescale. Indeed our usage of the $\varepsilon \to 0$ limit has until now been that of an approximation, so that nothing forbids to look at the rate function (4.33) or at the ISI distribution (4.39) in the slow timescale. Changing from fast to slow time is equivalent to performing a scaling

$$\begin{aligned} \lambda &\mapsto \lambda/\varepsilon \\ \sigma &\mapsto \sigma/\varepsilon, \end{aligned}$$

which can be derived by propagating the scaling (4.4) on the unidimensional potential and on the temperature through all the subsequent calculations. In slow time, and defining the frozen rate in slow time $\sigma' = \sigma/\varepsilon$, (4.33) and (4.39) read respectively

$$k(t, \beta) = \frac{\sigma'}{2}\left[1 + \tanh\frac{1}{2}(\lambda t - \tau)\right], \qquad (4.41)$$

$$\rho(t, \beta) = \frac{\sigma'}{2}\cosh^{\frac{\sigma'}{\lambda}}(\tau/2)\,\frac{e^{-\frac{\sigma'}{2}t}\left(1 + \tanh\frac{1}{2}(\lambda t - \tau)\right)}{\cosh^{\frac{\sigma'}{\lambda}}\frac{1}{2}(\lambda t - \tau)}. \qquad (4.42)$$

Plotting expression (4.39) in Fig.4.9 for several values of $T = \beta^{-1}$ we confirm the described shape, and as expected we get more and more peaked functions for higher T, with the peak receding closer and closer to the origin. The exponential rate of the right tail, being governed by the frozen system rate σ, is

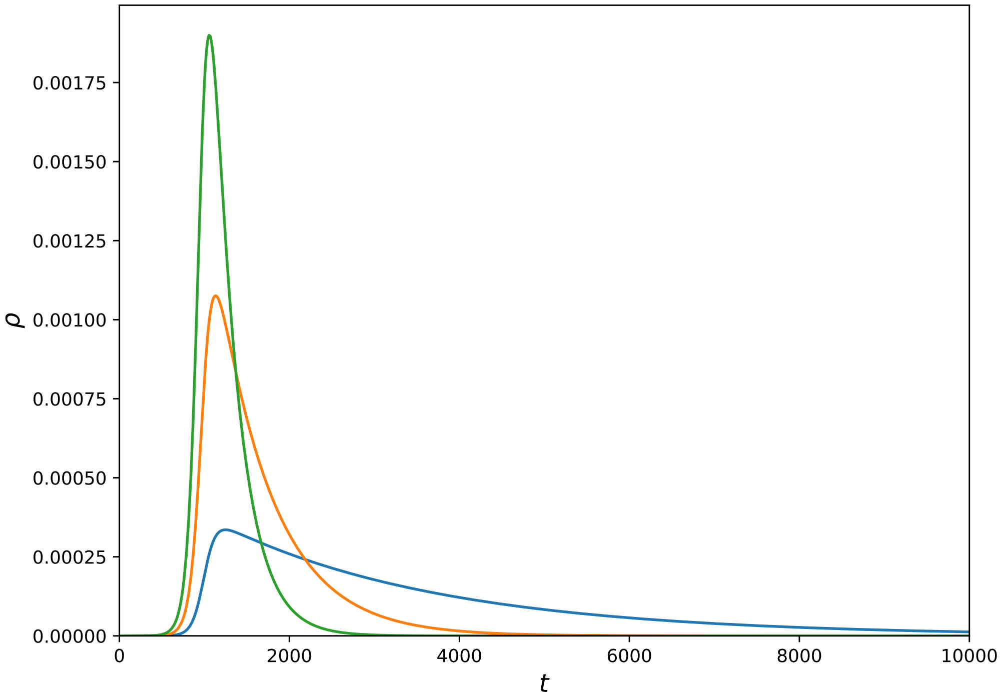

Figure 4.9: $\rho(t,\beta)$ plotted in fast time units for various values of temperature $T = 1/\beta$: $T = 7.5 \times 10^{-3}$ (blue), $T = 10^{-2}$ (orange) and $T = 1.25 \times 10^{-2}$ (green). The regression parameter has been fixed to an arbitrary value $\tau_0 = 10$ to allow plotting. System parameters were set to $\varepsilon = 10^{-2},\ a = 1.3$.

accordingly steeper and steeper for higher temperatures. It is important to note that the value of τ_0 that we used in Fig.4.9 is not derived from data, but only selected for plotting, and may in principle be β dependent.

In order to apply (4.39) to the full system we must fit it on data coming from simulations. In particular, due to our setup of the problem, we expect to only need to fit the parameter τ_0, which can be regarded in some sense as an *effective* refractory time. Approaching the problem from this point of view, we observe a general mismatch in the exponential trend of the right tail, red curves in Figures 4.10, 4.11 and 4.12, which in principle we would expect to be the most robust part of our approach. In particular we observe that the system always has a lower rate of decreasing with respect to the frozen one. In our interpretation of the FitzHugh-Nagumo system as a modulated well, this can be interpreted as a lower frozen system rate, corresponding to a deeper left well. Indeed, implicit in our derivation was the assumption that the location of the global fixed point $(u^*, v^*) = \left(-a, a^3/3 - a\right)$ remains the same in pres-

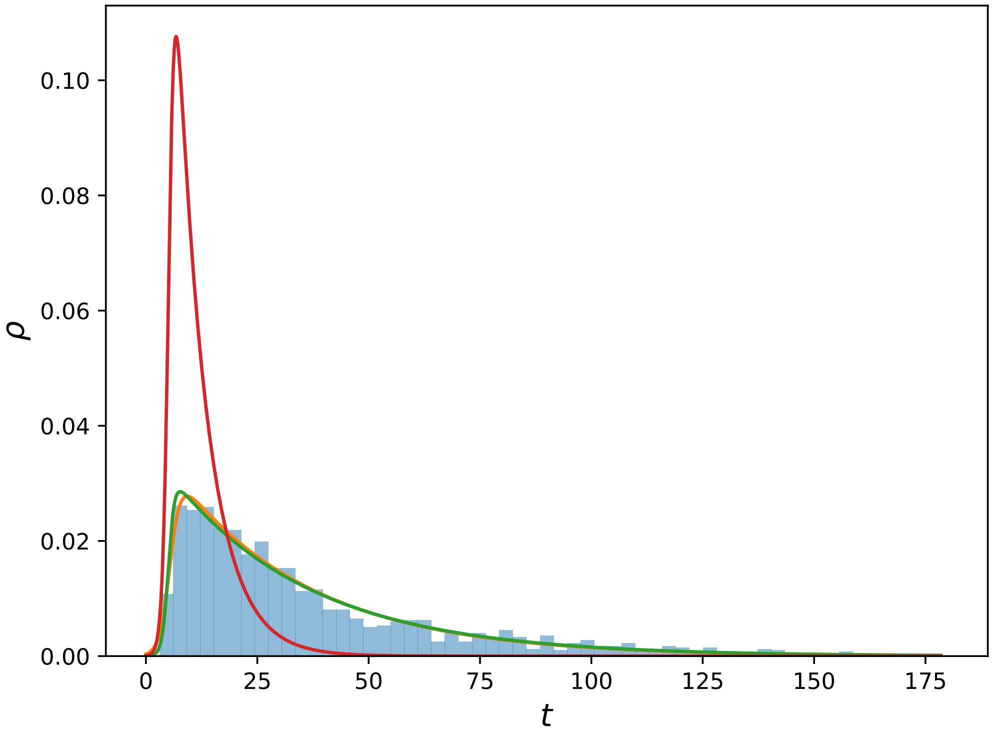

Figure 4.10: Fit of $\rho(t, \beta)$ on simulated data for $T = \beta^{-1} = 10^{-2}$. Solid lines mark fits respectively on τ_0 (red) as defined in (4.32), σ and τ_0 (green) and all parameters (orange). The histogram is density normalized with bins of width 3 slow time units. The system was simulated for a total of 5×10^4 slow time units.

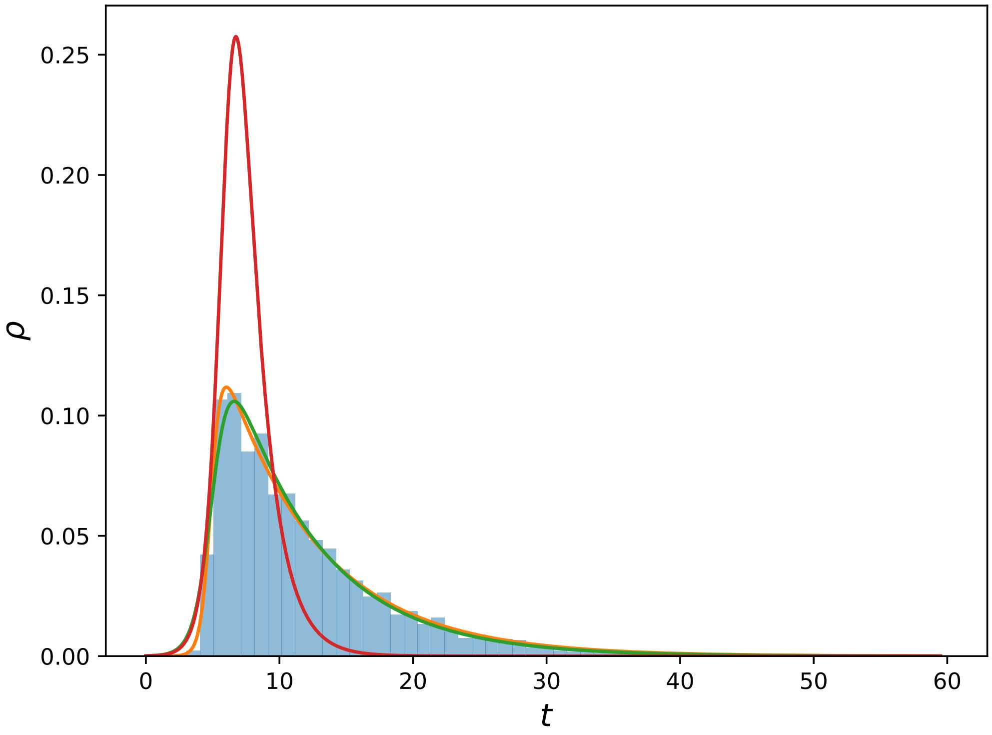

FIGURE 4.11: Fit of $\rho(t, \beta)$ on simulated data for $T = \beta^{-1} = 1.5 \times 10^{-2}$. Solid lines mark fits respectively on τ_0 (red), σ and τ_0 (green) and all parameters (orange). The histogram is density normalized with bins of width 1 slow time unit. The system was simulated for a total of 5×10^4 slow time units.

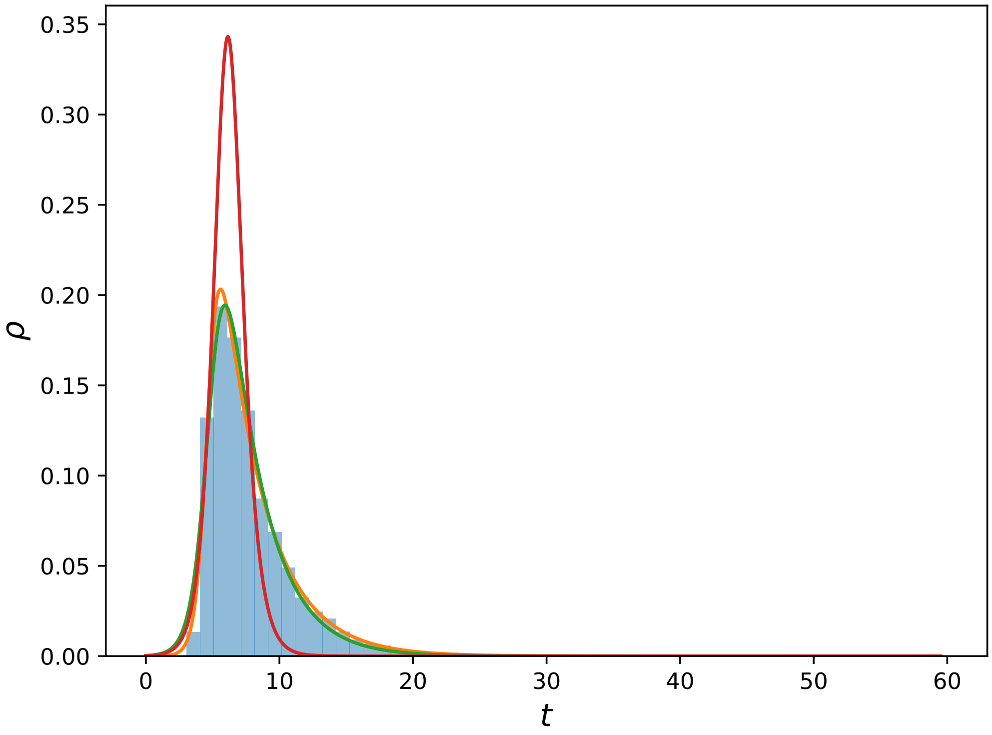

FIGURE 4.12: Fit of $\rho(t,\beta)$ on simulated data for $T = \beta^{-1} = 2 \times 10^{-2}$. Solid lines mark fits respectively on τ_0 (red), σ and τ_0 (green) and all parameters (orange). The histogram is density normalized with bins of width 1 slow time unit. The system was simulated for a total of 5×10^4 slow time units.

ence of noise, as fluctuations are averaged out. If this were not to be the case, a parametric noise-like effect could displace the global fixed point on average in a temperature dependent way, thus modifying the effective well depth governing the fast escape-like dynamics. To check this we can look at the average value of v on long evolutions of the system at various temperature values, excluding firing events, i.e. filtering out the activity that happens far from the fixed point: a parametric noise effect would give a net average displacement from the fixed point, while in a purely additive context fluctuations are expected to cancel out and not alter the equilibria of the system. To define the non-firing activity, we consider as significative neighbourhood of the fixed point a rectangle

$$u - u^* \leq \sqrt{2T}, \quad v - v^* \leq \frac{\sqrt{2T}}{a^2 - 1},$$

i.e. we measure an effect on the average of v within the standard deviation we would expect from a purely additive phenomenon with the system constrained to the nullcline. We plot the result in Fig.4.13, and observe a roughly linear dependence, which is a strong piece of evidence towards the presence correlations introduced in the slow variable by the effect of the fast noise giving rise to parametric noise-like effects.

Having pointed out the likely origin of the mismatch, we can fit the functional form by considering also σ a free parameter, so to match the rate with an *effective* well depth for the system due to correlations in the noise. By doing so we are able to better adapt our analytical forms to the simulation data, as is shown by the green lines in Figures 4.10 through 4.12. Since in principle also λ depends on the location of the fixed point, we should adapt its value based on the fitted frozen rate σ. Indeed fitting over its value as well, we obtain an even better accord with simulations, as indicated by the orange lines in Figures 4.10,4.11 and 4.12, but this could be simply the effect of an additional parameter in a fitting procedure so that a separate fit, or a functional estimate of λ from σ could resolve the ambiguity.

4.4 | Formulation of a simplified model for networked systems

The aim of this chapter is to develop a simplified model that can reproduce the statistics of the FitzHugh-Nagumo neuron, for applications related to the study information processing capabilities of neuronal networks. Specifically, we would like to reduce the full FitzHugh-Nagumo dynamics to a discrete binary system, which should bridge the gap between the easily treatable and in-

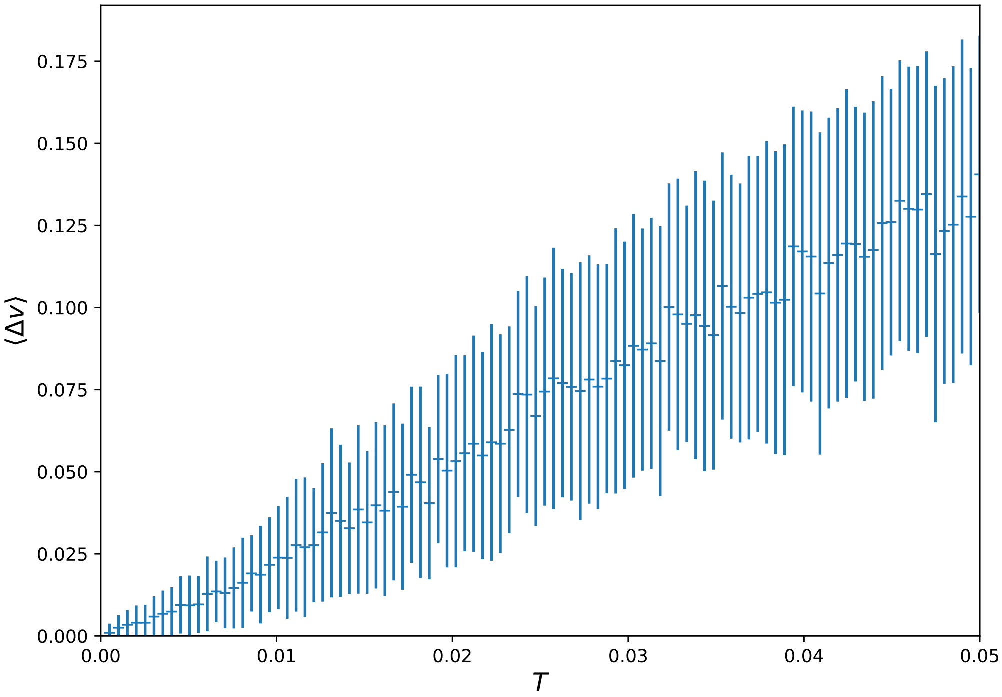

FIGURE 4.13: Average value of the $\Delta v = v - v^*$ displacement versus T. Averages were taken on evolutions of 100 slow time units. System parameters were fixed to $\varepsilon = 10^{-2}$, $a = 1.3$.

terpretable, but sharply simplistic, McCulloch-Pitts neuron, and the rich but complicated dynamics of nonlinear neural models.

To simplify the dynamics we build a system with discrete state variables and evolving at discrete time $n \in \mathbb{Z}$. Let us consider a binary unit, whose state takes a value $s \in \{0, 1\}$, representing for now generically a quiescent and activation state of the system. Let us then define the variable $n^* \in \mathbb{Z}$ which keeps track of the last time that the neuron has fired, i.e. switched from $s = 0$ to $s = 1$, as a minimal mechanism for keeping track of the dynamical history of the neuron. Our goal is then to calibrate a symbolic stochastic system as the one just introduced to reproduce the statistics of a noisy FitzHugh-Nagumo neuron, and to this end we need to introduce suitably the activation probability for the discrete unit. To do so, we consider time bins with a width of the order of the duration of a firing event, i.e. of a successful escape from the left well in the full system. This is a time $\Delta t = \mathcal{O}(\varepsilon)$ in the slow dynamics or $\mathcal{O}(1)$ in the fast one. Working equivalently in any of the two timescales, we introduce the firing probability, i.e. the probability of transitioning from $s = 0$ to $s = 1$, between time n and $n + 1$ after having last fired at n^* by interpolating the rate function $k(t, \beta)$ as follows

$$p_n(\beta) = \frac{\sigma}{2}\left[1 + \tanh\frac{1}{2}\left(\varepsilon\lambda\left(n - n^*\right) - \tau\right)\right]. \tag{4.43}$$

We define accordingly $q_n(\beta) = 1 - p_n(\beta)$ the probability of not firing, i.e. of remaining in state $s = 0$ while going from timestep n to $n + 1$. Whenever a firing transition is performed, i.e. the system finds itself in state $s = 1$, the value of n^* is set to $n^* = n$, the current timestep, and the system will transition to state 0 with probability $q_n = 1$, so that the system cannot remain for more than one timestep in the firing state $s = 1$. Considering the system at timestep n the transitions that can take place going to the next timestep are summarized as follows in terms of the activation state s and of the memory variable n^*

$$\begin{array}{lll} 0,\ n^* \le n \longrightarrow 0,\ n^* \le n & \text{with probability}\, q_n \\ 0,\ n^* \le n \longrightarrow 1,\ n^* \le n & \text{with probability}\, p_n \\ 1,\ n^* \le n \longrightarrow 0,\ n & \text{with probability}\, 1 \\ \text{otherwise} & \text{with probability}\, 0. \end{array} \tag{4.44}$$

Once the time dependent rate is defined, we can calculate the ISI probability mass function, obtaining the same result we would get by interpolating (4.39) according to the previously specified scheme. Multiplying by Δt so to obtain a probability mass from an interpolated density we get

$$\rho(\Delta n, \beta) = \frac{\sigma}{2}\cosh^{\frac{\sigma}{\varepsilon\lambda}}(\tau/2)\,\frac{e^{-\frac{\sigma}{2}\Delta n}\left(1 + \tanh\frac{1}{2}\left(\varepsilon\lambda\Delta n - \tau\right)\right)}{\cosh^{\frac{\sigma}{\lambda}}\frac{1}{2}\left(\varepsilon\lambda\Delta n - \tau\right)}. \tag{4.45}$$

To test out our construction, we proceed by simulating a FitzHugh-Nagumo neuron and fitting the τ_0 and σ parameters in (4.39) with regression routines. We then use the parameter values to setup a discrete unit and simulate a sample of interspike times from it. In Fig. 4.14 a comparison can be seen, showing good accord once the bins are mapped back to continuous time using the correct scaling.

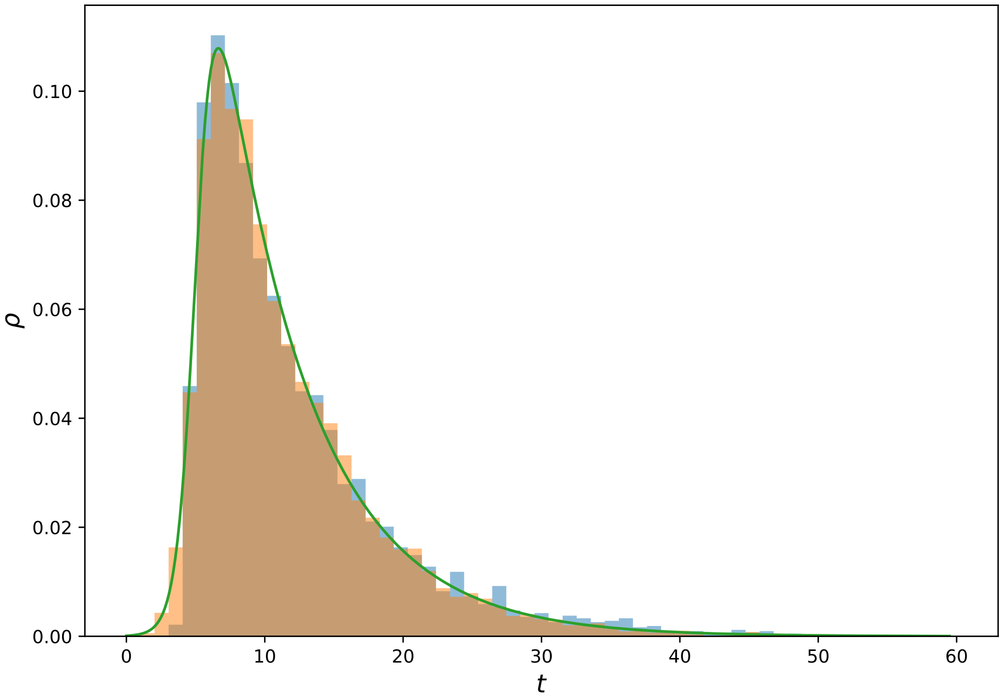

Figure 4.14: Comparison of the ISI histograms for the full FitzHugh-Nagumo system (4.18) (blue) and the discrete model (4.43) (orange). The solid greed line is the fit to ISI distribution of the full system, to obtain the values of σ and τ for the discrete model. Both systems were simulated for a total of 10^5 slow time units. Histogram are drawn in density and bins are 1 slow time unit wide.

4.4.1 | Adaptation to networked systems

In order to be able to construct networks of discrete units, we must devise a consistent way of representing external inputs. While a mapping of coupling terms present in FitzHugh-Nagumo neurons to a term in this simplified model is in principle a challenge, we propose a minimal substitution that allows to take into account the effect of an external stimulus on a discretized unit.

To get an insight we consider (4.1) in presence of a slow external input term $I(t)$ in the u variable dynamics, it reads

$$\begin{aligned}\dot{u} &= u - \frac{u^3}{3} - v + I(t) + \sqrt{2T}\xi \\ \dot{v} &= \varepsilon\left(u + a\right).\end{aligned} \tag{4.46}$$

This modification in the full dynamics translates into a change in the form of V_1 which becomes

$$V_1(u; v, I) = \frac{u^4}{12} - \frac{u^2}{2} + (v - I)u, \tag{4.47}$$

so that the value of I can change the slope of the linear term in the double well potential, possibly boosting or suppressing the firing rate. To encode this feature in the discretized model rate function (4.43), we propose to introduce a modification of the frozen rate factor σ, implemented as follows

$$p_n(\beta) = \frac{1}{4}\left[1 + \tanh\frac{1}{2}\left(\varepsilon\lambda n - \tau\right)\right]\left[(1+\sigma) + (1-\sigma)\tanh\left(JI(n) - k\right)\right], \tag{4.48}$$

where $J,\ k$ are two constants to be set phenomenologically, essentially depending on the relevance that one wants to give to the external input I in the elicitation of a spike. The role of k is essentially that of a threshold, and it should be set to $k \ll 1$ so that for $I = 0$ we recover a firing rate without input very close to σ. J on the other hand is an input gain, and to have a meaningful role it should be set to $J = \mathcal{O}\left(k\right)$, in order to balance out k in presence of nonzero input with the exact value to be chosen according to the increase in firing probability one wants to have for a given input strength.

We now aim to simulate a closed chain of FitzHugh-Nagumo neurons in presence of noise with a chain of simplified systems. The dynamics of the FitzHugh-Nagumo chain is given by

$$\begin{aligned}\varepsilon\dot{u}_i &= u_i - \frac{u_i^3}{3} - v_i + J\left(u_{i-1} - u_i\right) + \sqrt{2\varepsilon T}\xi_i \\ \dot{v}_i &= u_i + a,\end{aligned} \tag{4.49}$$

where J is a coupling strength, ξ_i is a vector of independent white noise with zero mean and autocorrelation function

$$\langle \xi_i(t)\xi_j(t+\tau)\rangle = \delta_{ij}\delta(\tau),$$

and we identify $N + 1 = 1$ implementing periodic boundary condition, so that essentially we are simulating the chain of Chapter 1 in the presence of noise.

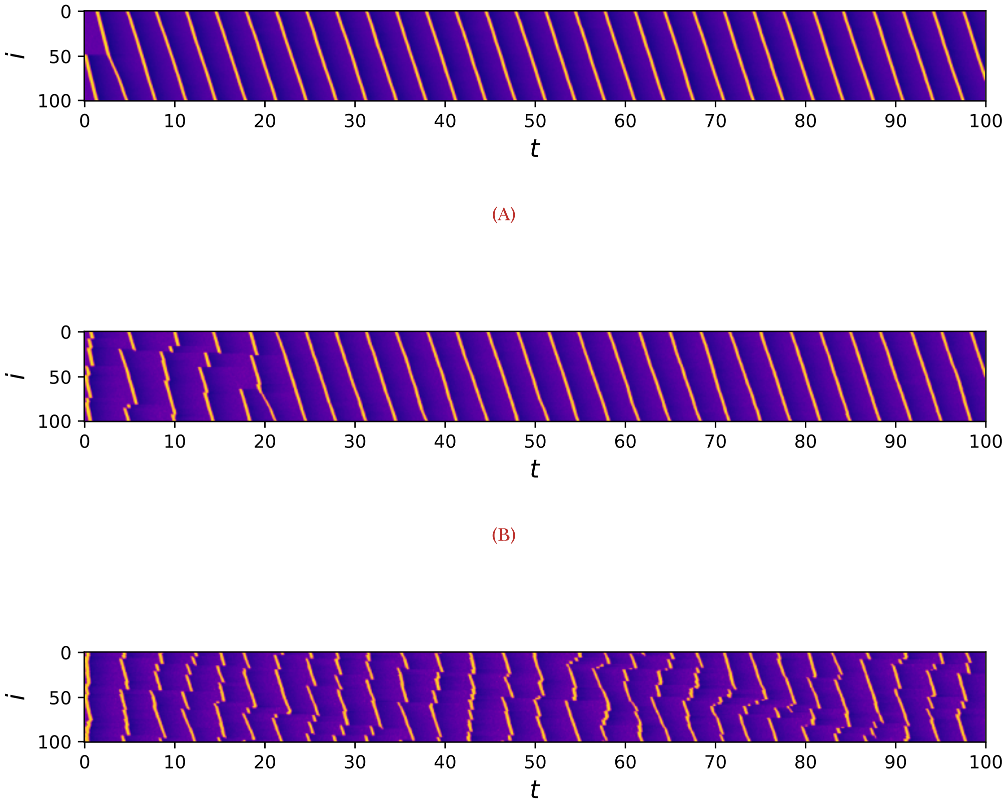

(A)

(B)

(C)

Figure 4.15: Raster plot of the u variable for the chain system (4.49) for three values of temperature: (a) $T = 10^{-2}$, (b) $T = 2.5 \times 10^{-2}$, (c) $T = 5 \times 10^{-2}$. The system is initialized with a spike of magnitude 1 on the $i = 50$ node. Node indices are read on the ordinate axis, time in slow units is read on the abscissa. The remaining system parameters are set to $a = 1.3$, $J = 0.2$, $\varepsilon = 10^{-2}$ and $N = 100$.

Some typical trajectories are shown in Fig. 4.15. For low temperatures we observe a periodic self consistent solution, reminiscent of that of the system without noise, stable over finite times which we expect to be exponentially long as a function of the inverse temperature. As the temperature is raised, stronger fluctuations are observed, prolonging the transient before the onset of the stable wave. For even higher values of T we observe a progressive disruption of the wave pattern by the white noise. The foremost mechanism through which this happens is given by the wave front colliding with neurons that have anticipated it, firing purely because of the noise. Since the Laplacian coupling modifies the dissipation of the single chain node, we fit the discrete system to the statistics of an isolated system given by

$$\begin{aligned} \varepsilon\dot{u} &= (1-J)u - \frac{u^3}{3} - v + \sqrt{2\varepsilon T}\xi \\ \dot{v} &= u + a, \end{aligned} \tag{4.50}$$

in order to be able to treat the input of the driver neuron like the term $JI(t)$ of (4.46). We now define a chain of simplified systems, denoting with the subscript $i \in \{1, \dots, N\}$ the chain site and identifying $N+1 = 1$ so to implement periodic boundary conditions. The activation probability for site i reads

$$p_{n,i}(\beta) = \frac{1}{4}\left[1 + \tanh\frac{1}{2}\left(\varepsilon\lambda n - n_i^* - \tau\right)\right]\left[(1+\sigma) + (1-\sigma)\tanh\left(Js_{i-1}(n) - k\right)\right], \tag{4.51}$$

where we have implemented a directed chain coupling via the previously introduced substitution designed to deal with external inputs. Trajectories of the simplified chains are represented in Figure 4.16 and a close up is available in Fig.4.17. Despite observing qualitatively similar behaviour to the full system, using the fitted values we do not observe (Fig. 4.51 (a)) the stabilization of a traveling wave, as expected from simulation of the full system (Fig. 4.15 (b)), but rather very sparse activity that cannot be qualified as a propagating wave. We conjecture that such a behaviour may be dictated by the fact that, as observed in the previous chapters for deterministic chains, the inter-site propagation time is $\mathcal{O}(\varepsilon)$ in slow time, but not exactly ε, so that we cannot represent with a single discrete step width the duration of both phenomena. To assess the influence of this fact we coarse grain the discrete system time, panels (b), (c) of Fig. 4.16 and close-up in Figure 4.17, respectively of a factor 10 and 100. A stabler situation is observed in both cases, with longer-lived wave fronts propagating through the system, but there are still no strong traces of a behaviour similar to that of SDE (4.49).

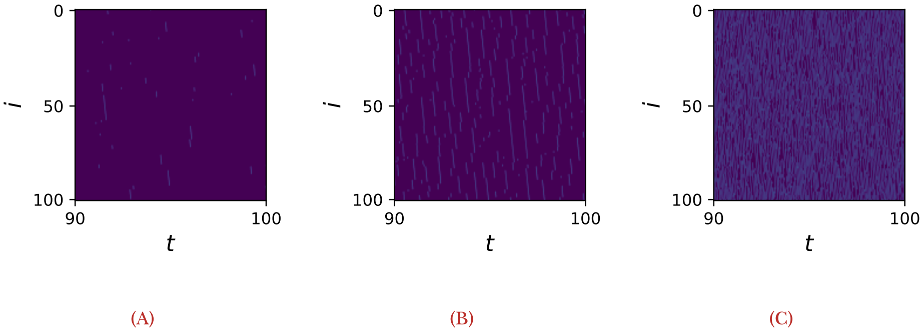

(A)

(B)

(C)

Figure 4.16: Raster plots of the state variable s_i for the simplified chain (4.51). The system parameters in panel (a) have been fitted on the single full neuron dynamics (4.50) with values $\sigma_f = 5.1 \times 10^{-4}$, $\kappa_f = 7.25 \times 10^{-3}$, $\tau_f = 447.36$. In the two other panels the simulation is performed respectively for (b) $\sigma = 10\sigma_f$, $\kappa = 10\kappa_f$, $\tau = \tau_f/10$ and (c) $\sigma = 100\sigma_f$, $\kappa = 100\kappa_f$, $\tau = \tau_f/100$. The full system parameters on which the units of panel (a) have been fitted are $a = 1.3$, $\varepsilon = 10^{-2}$, $J = 2 \times 10^{-2}$, $T = 2.5 \times 10^{-2}$. Time is marked in slow units of the full dynamics.

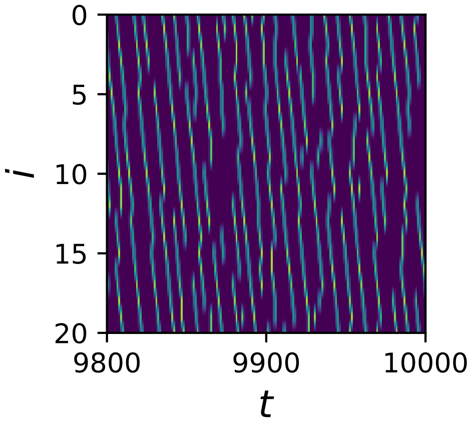

Figure 4.17: Close up of Fig. 4.16, panel (c) for the first 20 simplified units on the last 20 slow time units of the full system. Time is marked in discrete timesteps of the simplified system, corresponding to fast time units in the stochastic differential equation (4.49).

4.5 | Conclusion

In this chapter we have studied the statistical behaviour of the FitzHugh-Nagumo neuron in presence of fast, additive noise. By approximating the slow dynamics with its trajectory in the limit $\varepsilon \to 0$ we are able to treat it as a slow modulation triggered by the previous firing event. This approach allows us to close an approximated functional form for the ISI distribution, which despite being derived from first principles needs fitting in order to reliably represent the statistics of actual units. Investigating the reason of this mismatch we reveal a limit of our approximation, which rests in the assumption that for small values of ε we can treat the slow and fast dynamics as decoupled. Indeed the coupling of timescales introduces correlations in the effective noise applied to v through the dependence on u of its dynamics, so that a displacement of the fixed point is observed, in a parametric noise-like scenario reminiscent of Stratonovich equations. This average displacement of the fixed point, in turn, affects the firing rate significantly, through the exponential dependence of the Arrhenius factor on the well depth. From a more model-focused point of view, we observe that the ISI distribution takes the shape of a smoothed-out asymmetric Laplace distribution, which is observed in a broad class of models related to survival analysis, where the time necessary for an event to take place is modeled as having a clear modal value but long asymmetric tails [66].

In the final part of the chapter we are able to formulate a discrete model that well represents the firing statistics of the FitzHugh-Nagumo neuron, while relying solely on a binary state variable and an integer memory variable. While the accord is quite good for the firing statistics of a single unit, the behaviour for a ring of units is noticeably different between the discrete and the continuous system, despite showing qualitative correspondences.

Further research on these topics should surely deal with the emergent parametric noise effects via dedicated techniques, in order to possibly reconcile the effective discrete model with first principles. With respect to the discrete unit, care should be devoted to the study of appropriate coupling schemes for the study of networked systems, in particular with respect to the correct implementation of the inter-neuron propagation timescale of signals, which despite being often an overlooked feature, appears from our studies to play a paramount role in the dynamics, pointing out that its representation in simplified models should be given proper consideration.

5 | A distributed delay model for pandemics short-term forecasting in a metropolitan area

Parts of this chapter together with other research by a larger working group, have resulted in an article by F. Durazzi, E. Lunedei, G.C., G. Gatti, V. Sambri, A. De Cesare, C. Crippa, F. Pasquali, Bologna MODELS4COVID Study Group, G. Castellani, D. Remondini, A. Bazzani, *Human mobility and sewage data correlate with COVID-19 epidemic evolution in a 3-year surveillance of the metropolitan area of Bologna*, submitted to PNAS Nexus for review.

5.1 | Introduction

The COVID-19 pandemic has been one of the most challenging worldwide events of recent contemporary history, prompting a society-wide effort towards the comprehension of the pandemic phenomenon and the development of containment measures. A leading direction in this effort has been the collection of large amounts of data and the integration of different data sources, thus making the COVID-19 outbreak one of the most documented worldwide epidemic events. In particular, in response to the great infectivity of the disease, forecasting attempts have been carried out often on short, i.e. weekly, to very short, daily, time spans, conditions which can be referred to as *nowcasting* and that often require specialized approaches.

In this chapter we present our work on delayed epidemiological models for short-term forecasting on a metropolitan area level of the COVID-19 pandemic. We begin with a short presentation of the mathematical basics of epidemiological modeling, and how they can be interfaced with commonly used clinical indicators such as the basic reproduction number. We then present our distributed delay compartmental model, and comment on its application in weekly scale forecasts of the new positives time series. Subsequently we discuss a relationship observed between an inferred sociability parameter used in the regression phase and a mobility proxy for the average contact rate in the population of the metropolitan area. We remark that such a relationship can prove quite relevant in such cases, as on short periods of time it can provide a reliable almost *a priori* estimate from easily retrievable data for a parameter otherwise difficult to measure. The construction of the proxy itself, moreover, can provide insightful information on the population compliance with the government-mandated safety measures. Finally we present some linear response theory results for the delayed model, which can be applied to the regression problem, in order to quantify the sensitivity of the inferred sociability parameter time series to fluctuations in the clinical admissions data. This latter application is particularly relevant, as it can lay the basis for quantitative models to study the efficiency of different measures for pandemic containment, in particular to reach a trade-off with the social cost and economical impact often implied by such provisions.

5.2 | Some notions of mathematical epidemiology

5.2.1 | Compartmental models

The most common type of models employed in the study of epidemiological phenomena consists of compartmental models. As the name implies these models simplify the course of an infectious disease in a susceptible individual as a series of movements between compartments, each one representing a stage of the infection or the symptoms that the individual is manifesting. As patients transition to and from compartments, the compartments populations are increased or diminished accordingly, so that the time series of the compartments populations furnishes the number of patients a the various stages over time. Historically, the first development of such models has been done in terms of Distributed Delay Differential Equations [54], as they were formulated with the idea of reproducing adherently the distributed character of various stages of a disease. Due to the potentially complicated dynamics of delayed models, and since in many cases the delay kernels can be approximated by average transition rates, a simplified version has been formulated in the subsequent decades, in terms of Ordinary Differential Equations. The simplest example of a compartmental epidemiological model is the SIR model [43], which subdivides the individuals into three containers: Susceptibles S, Infected I and Removed R. It models a disease with no possibility of reinfection, for which no vaccination campaign is active and with no variations to the freedom of movement of the individuals. The governing differential equations are

$$\begin{aligned}
\dot{S} &= -\beta \frac{I}{N} S \\
\dot{I} &= \beta \frac{I}{N} S - \gamma I \\
\dot{R} &= \gamma I,
\end{aligned} \tag{5.1}$$

where the variables represent:

- S: population of the Susceptibles compartment, i.e. individuals that have not had any contact with the disease yet,
- I: population of the Infected compartment, representing patients which have had contact with the disease, developed symptoms and the ability to infect other susceptible individuals,
- R: population of the Removed compartment, comprehensive of all individuals for which the disease has run its course, which are therefore removed from any further role in the dynamics.

The model presents two parameters β and γ. β is usually referred to as the *effective contact rate* and it corresponds to the conditional probability per unit of time that a Susceptible individual have a contact and become infected as a consequence of this, provided that this encounter be with an Infected individual. γ which is the probability per unit time that an Infected individual be removed from the dynamics, i.e. the rate at which the disease runs its course in patients who have contracted it. From this definition of the parameters we intuitively expect that model (5.1) could be considered a mean field approximation for a stochastic process modeling the epidemics, so that the compartments may be considered as the mean values for the stochastic model populations. This can be proved using several approaches, and in particular by considering Poisson processes with time varying rates [4, 6]. It is important to notice, as an element of consistency, that since no birth/death dynamics has been implemented aside from the possible deadly outcome of the disease, accounted for in the R compartment, the dynamics specified by (5.1) preserves the sum $N = S+I+R$, where N is the overall population of the model. An important additional assumption for (5.1) is the so-called *well stirred* hypothesis, which amounts to requiring that the chance of meeting an infected individual is the same for each susceptible, i.e. there are no spatial features that may play a difference. While being formulated initially in the context of chemical physics, the well stirred hypothesis amounts to treating geographical structures as negligible in the formulation of the epidemiological model. A typical trajectory for the SIR model looks like

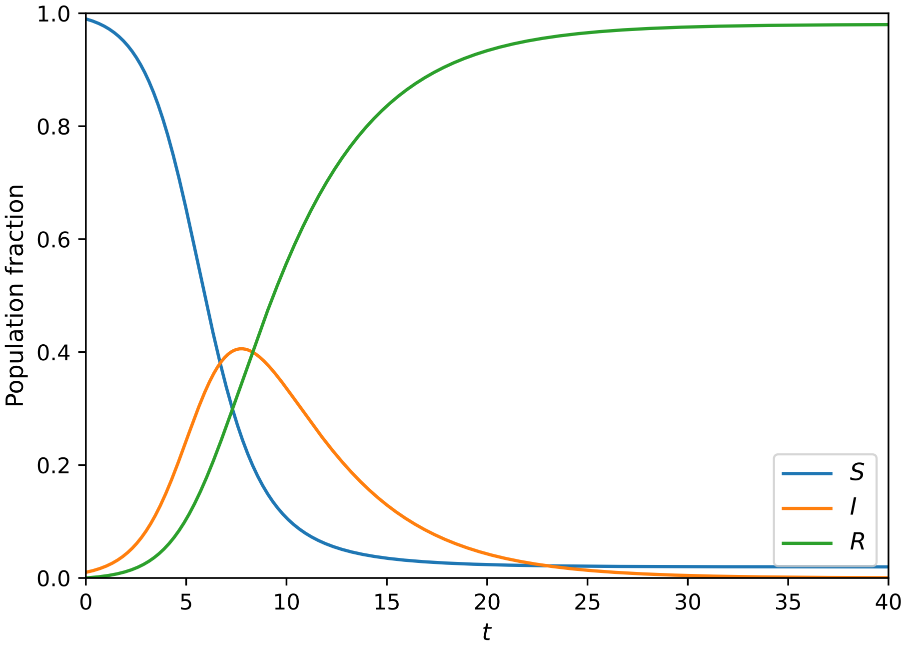

Figure 5.1: Trajectory for a SIR model with $\beta = 1$ and $\gamma = 1/4$. The initial fraction of infected individuals is the 1% of the whole population.

Figure 5.1: after the introduction of some infected individuals (1% of the whole population in this example) the number of infected cases starts to grow, then it reaches a maximum and starts to decline. Notice that it is quite common to observe a residual population of susceptibles after the epidemics ends.

5.2.2 | Relationship between model parameters and epidemiological indicators

The parameters β and γ can be estimated in applications by several means, but it is important to try to relate them to the measured quantities used by physicians and epidemiologists in the field to track the evolution of epidemics. The principal indicator considered in practical cases is the *basic reproduction number* $\mathcal{R}_0$ [25]. This quantity is a dimensionless constant and represents the expected number of secondary infections that result from a single infected case in a fully susceptible population. From an operative point of view, $\mathcal{R}_0$ can be defined via

$$\mathcal{R}_0 = \tau\, \bar{c}\, T_I, \tag{5.2}$$

where

- τ is the disease *transmissibility*, i.e. the probability that during an unprotected contact between an infected and a susceptible individual the latter be infected,
- $\bar{c}$ is the *contact rate*, the average number of contacts between infected and susceptible population individuals per unit time,
- T_I is the *duration of infection* in infected individuals.

This definition is clearly more apt to clinical settings, but we can easily relate it to the model parameters. Indeed in (5.1) the definition of β as the conditional rate of infectious contacts enables us to recognize $\beta = \tau\,\bar{c}$. Furthermore, since γ is the rate at which Infected individuals are removed, it is natural to identify $T_I = \gamma^{-1}$, thus yielding for the basic SIR model (5.1)

$$\mathcal{R}_0 = \frac{\beta}{\gamma}. \tag{5.3}$$

This identification is further backed by the role played by (5.3) in the SIR dynamics. Indeed by considering the equation for the I compartment right at the beginning of the outbreak, i.e. approximating $S \approx N$, we get

$$\dot{I} = (\mathcal{R}_0 - 1)\,\gamma I, \tag{5.4}$$

so that if $\mathcal{R}_0 < 1$ we get a decreasing exponential trend and the potential epidemic is reabsorbed before gaining momentum, conversely for $\mathcal{R}_0 > 1$ the exponential is increasing and the population suffers an epidemic outbreak. If instead we write (5.4) at a certain time instant t further during the evolution of the epidemics, we get a scaling on the threshold for a decreasing exponential, which becomes $\beta S(t)/\gamma N < 1$ and is interpreted as an indicator of the epidemic phase the system is in, i.e. whether a peak in the cases is still coming or it has already passed. Such threshold varies from model to model and is usually called the *effective reproduction number*, and denoted $\mathcal{R}_t$, as it generalizes (5.3) to a different time from the beginning of the outbreak. Therefore we are able to connect the empirical interpretation of the basic reproduction number with its role in the dynamics of a very simple epidemiological model.

5.2.3 | Limitations and possible extensions of the basic SIR model

As we have formulated it so far, the SIR model is very simplistic and fails to capture many aspects of an epidemic phenomenon that may play a relevant role in real world scenarios, to name a few:

1. the model lacks any possibility of reinfection, since after transitioning into compartment R the individuals stop playing any active role in the dynamics and cannot become susceptible again,

2. no mitigation policy (lockdowns, social activity regulations, etc.), variation of disease infectivity (e.g. as caused by different variants becoming prevalent) or vaccination strategy is present, since transition rates are constant over time and there is no modeling of vaccination in any form,

3. the model does not account for any immigration or emigration of population to and from the region of interest, which is for all purposes considered closed, similarly there is no geographical structure within the region,

4. no role is given to the age of individuals, be it through different response to the pathogen or through differentiated social interactions between age groups,

5. an instantaneous dynamics such as that of (5.1) considers neither the explicit duration of the various disease stages nor possible fluctuations of the duration, since these are modeled on average via the transition rates. The representation of these characteristic times as rates of instantaneous processes may also be a poor approximation in the case of widely differing characteristic timescales.

It must be noted that none of these aspects is a limitation *per se*, but rather may or may not be one depending on the case under study. The Physics of Complex Systems and Mathematical Biology literature is rich with variations and elaborations of the ideas presented so far depending on the characteristics of the problem being tackled. The simple addition of a reinfection process yields the classical SIS or SIRS model [44]. Similarly, the promotion of parameters such as β and γ to time dependent quantities is a classical procedure in mathematical epidemiology, to account for environmental effects such as seasonality, emergence of pathogen variants, changes in social interaction regulations and even evolution of the clinical approach. A vaccination dynamics can be taken into account [64] where susceptibles are removed without infection. The effects of age groups can be taken in consideration, both modeling different responses to the disease and accounting for the different interactions structures between age brackets [83]. A spatial structure can be added, e.g. with metapopulation models on geographical networks such as [85], with cellular automata or even with partial differential equations comprising of diffusion phenomena [93]. Explicit delay effects can be taken into account in various forms, such as in systems of delay differential equations [23, 86] or also combined with spatial effects with delayed partial differential equations [38].

5.3 | Compartmental model for the COVID-19 epidemic in the Bologna Metropolitan Area

5.3.1 | Model definition

The aim of this part of the work has been to develop an epidemiological model for the COVID-19 pandemic in the Metropolitan Area of Bologna, with the practical purpose of following the course of the pandemics and making weekly forecasts of the number of new positives and their peaking time. This work has been carried out in collaboration with the Local Health Authority (Italian *Azienda Unità Sanitaria Locale*, short AUSL), which provided data on a daily basis to inform the forecasts. The data consisted in the daily time series of admissions into ordinary wards and Intensive Care Units of the Metropolitan Area hospitals and of the new positive cases detected from swabs. The goal of the *nowcasts* obtained from the model was to provide the Bologna AUSL COVID Task Force with weekly information on the course of the pandemic, in particular to inform the readiness of the health infrastructure in terms of the expected need of ordinary ward and ICU beds, so to avoid dangerous resource stress conditions on the local healthcare system.

To model the epidemic spreading in a metropolitan area, we construct a distributed delay compartmental SEUIR model based on [11]. This model complements the SIR dynamics presented in the previous section with two compartments: the Exposed individuals who have had a contact with the SARS-CoV-2 virus but are not yet contagious and the infective Unreported individuals, who play a key role in the spread of the COVID-19 epidemics [61]. We consider a delayed model specifically to account for the significant lag between the beginning of the infectious phase and the possible development of symptoms, during which infectious individuals are free to move and spread the contagion. Moreover, the necessity of a distributed delay approach was made evident in data by the lag observed between the application of containment measures and the observation of their effect. Specifically, for any time $t \geq 0$, the total population is subdivided into two groups

$$N(t) = P(t) + I(t) \,,$$

where $N(t)$ is the total population in the area which we assume to be constant over time except for a small decrease given by dead individuals. The group $P(t)$ is the *active population*, that takes part in social activities and contributes to the contagion dynamics while group $I(t)$ contains the isolated infected population, i.e. cases that have developed some degree of symptoms and in consequence are quarantined or admitted into hospital care and are assumed not contribute to the epidemic spread. The active population, $P(t)$ is divided into four compartments:

$$P(t) = S(t) + E(t) + U(t) + R(t) ,$$

where $S(t)$ is the number of *Susceptible* individuals, $E(t)$ is number of *Exposed* individuals (i.e. people that have had a contact with the pathogen, but are not yet contagious), $U(t)$ is number of *Unreported* infected individuals (i.e. infected individuals that have not developed serious symptoms or anyway have not been reported) and $R(t)$ is number of *Recovered* individuals that have been immunized. In the R compartment we account for both subjects that have acquired immunity naturally and subjects who have been vaccinated. The epidemic evolution is simulated by a compartmental model according to the following steps (see also the diagram in Figure 5.2):

1. a *Susceptible* individual may become Exposed after meeting an *Unreported* infected individual. The rate at which infection-bearing contacts occur is regulated by β. The rate β is further modulated during the evolution of the system by two multiplicative factors, the relative infectivity τ with respect to wild-type SARS-CoV-2 and the relative sociability s which represent the variation of the average number of at-risk social contacts between individuals. Both factors are relative as the baseline value for both quantities is contained in the β parameter;

2. an *Exposed* individual becomes an *Unreported* infected one after a time interval T_E;

3. an *Unreported* individual can infect other people. After a random time interval drawn with mean T_U they can develop a symptomatic form with a probability α and be isolated, thus transitioning to compartment I, or with probability $1 - \alpha$ recover and be transferred to compartment R;

4. reportedly infected individuals are *Isolated* either in home isolation or in a hospital ward. After a time T_I they transition to the *Recovered* compartment or succumb to the illness. For simplicity we considered a time T_I corresponding to the initial quarantine period established by the Italian Health Ministry, which works as an average value between the large majority of short domestic isolations and the minority of prolonged hospital admissions, e.g. in ICUs or sub-ICUs;

5. after a longer time T_R, *Recovered* individuals are returned to the *Susceptible* compartment, as immunization is lost. For simplicity it has been assumed that the effective duration of immunity is the same regardless of its natural or vaccine-induced origin.

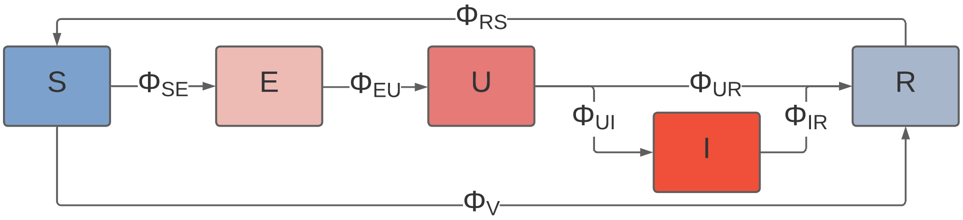

Figure 5.2: Schematic representation of the compartmental model described by (5.5).

A vaccination flow was added in correspondence of the beginning of the vaccination campaign in late 2020 (the first doses were administered to physicians and healthcare personnel from the the 28^{th} of December), using daily data provided by the AUSL. The main ingredient of the model dynamics is the average infection flux between Susceptible and Exposed individuals, from which all the other fluxes are obtained. We define it as

$$\Phi_{SE}(t) = \beta s(t)\tau(t)\frac{U(t)}{P(t)}S(t) ,$$

where one assumes that the probability of meeting an infected unreported individual U is proportional to their concentration in the active population P. This stems from the *well-stirred* assumption, which in this context takes the name of *homogeneous mixing*, i.e. that individuals are evenly diffused across the region of interest by their own mobility patterns. The parameter β has the same interpretation as in the classical SIR model of Sec. 5.2.1, but we introduce two additional relative time-dependent factors $s(t)$ and $\tau(t)$. The *relative sociability* parameter $s(t)$ is proportional to the average number of at-risk social contacts per unit time, for each individual belonging to the active population. It can be modulated over time to represent variations in social activity policies such as lockdowns, curfews, social distancing and the suspension or remote reorganization of in-presence jobs and commercial activities. The adoption of personal protection devices such as face masks is also accounted for in this factor, since they make otherwise at-risk contact safer. Another contribution to this term stems from environmental factors, such as weather seasonality, with higher temperatures acting both on a biochemical ground, by accelerating the degradation of viral capsids [40], and on a social ground by promoting the relocation of social activities in outdoor settings. It is a relative term due to the intrinsic difficulty of measuring directly an absolute value for the number of social contacts per unit time in a privacy-regulations-compliant way. With respect to the factorization of β observed in Sec. 5.2.2 it can be regarded as a time-dependent scaling of the $\bar{c}$ term. The *relative infectivity* parameter $\tau(t)$ represents the changes in the virus infectivity with respect to wild-type SARS-CoV-2 and accounts for virus evolution. In particular it can be changed based on a-priori estimates coming from available biological literature whenever a new COVID variant becomes prevalent.

The compartmental dynamics presented so far is represented schematically in Figure 5.2, and it is described by the following distributed delay differential equation:

$$\begin{aligned}
\dot{S}(t) &= -\Phi_{SE}(t) - v(t)S(t) + v(t-T_R)S(t-T_R) \\
&\quad + (1-\alpha)\int_0^\infty \mathrm{d}\tau\, \Phi_{SE}(t-T_E-T_R-\tau)\rho(\tau;T_U,\sigma_U) \\
&\quad + \alpha\int_0^\infty \mathrm{d}\tau\, \Phi_{SE}(t-T_E-T_I-T_R-\tau)\rho(\tau;T_U,\sigma_U) \\
\dot{E}(t) &= \Phi_{SE}(t) - \Phi_{SE}(t-T_E) \\
\dot{U}(t) &= \Phi_{SE}(t-T_E) - \int_0^\infty \mathrm{d}\tau\, \Phi_{SE}(t-T_E-\tau)\rho(\tau;T_U,\sigma_U) \\
\dot{I}(t) &= \alpha\int_0^\infty \mathrm{d}\tau\, \Phi_{SE}(t-T_E-\tau)\rho(\tau;T_U,\sigma_U) \\
&\quad - \alpha\int_0^\infty \mathrm{d}\tau\, \Phi_{SE}(t-T_E-T_I-\tau)\rho(\tau;T_U,\sigma_U) \\
\dot{R}(t) &= (1-\alpha)\int_0^\infty \mathrm{d}\tau\, \Phi_{SE}(t-T_E-\tau)\rho(\tau;T_U,\sigma_U) \\
&\quad - (1-\alpha)\int_0^\infty \mathrm{d}\tau\, \Phi_{SE}(t-T_E-T_R-\tau)\rho(\tau;T_U,\sigma_U) \\
&\quad + \alpha\int_0^\infty \mathrm{d}\tau\, \Phi_{SE}(t-T_E-T_I-\tau)\rho(\tau;T_U,\sigma_U) \\
&\quad - \alpha\int_0^\infty \mathrm{d}\tau\, \Phi_{SE}(t-T_E-T_I-T_R-\tau)\rho(\tau;T_U,\sigma_U) \\
&\quad + v(t)S(t) - v(t-T_R)S(t-T_R)
\end{aligned} \tag{5.5}$$

where $\rho(s;T_U,\sigma_U)$ is the probability distribution function of the permanence time in the Unreported compartment. The choice for the functional form is a Gamma distribution, which is a typical choice for incubation periods distributions, with average value T and variance σ^2

$$\rho(s;T,\sigma) = \frac{b^a}{\Gamma(a)} s^{a-1} e^{-bs} \tag{5.6}$$

with $a = (T/\sigma)^2$ and $b = T/\sigma^2$ and $\Gamma(x)$ the Gamma function. (5.5) are the equations for the full epidemiological model used for predictions in the metropolitan area of Bologna. Global solutions to (5.5) cannot be written in a closed form, so simulations were performed through numerical integration: due to the regularizing effect of the Gamma convolution [1]despite potential discontinuities that can be present in the $s(t)$ function we can integrate numerically (5.5) with a simple Euler scheme. A hourly or half-hourly timestep was usually chosen, with a rebinning of the resulting trajectory to a daily resolution for comparison with the data. Recapitulating, to run a simulation of the pandemic, model (5.5) requires the specification of several parameters, some as constants and some as functions of time:

- the permanence times T_E, T_U, T_I, T_R and the standard deviation for the U compartment σ_U, in principle it is possible to take them as functions of time we chose to keep them fixed for the sake of simplicity, [2]
- the fraction of symptomatic patients α,
- the parameter β,
- the relative transmissivity $\tau(t)$ as a function of time to represent the takeover of the various SARS-CoV-2 variants,
- the relative sociability $s(t)$ as a function of time,
- the vaccination forcing term $v(t)$ as a function of time.

In addition to these parameters a suitable initial condition must be selected. Since these equation contain a distributed delay, the initial condition formally is a function $C_0(t)\ :\ ]-\infty, 0] \rightarrow \mathbb{R}^5$. This adds in principle to the flexibility of the model, as we could for example simulate a rebound wave of cases after a pandemic wave has already struck the population, but elaborate initial conditions can sometimes have hard-to-control behaviours in DDEs, so we opt for a simpler approach. In our case we choose a constant initial condition $C_0 = (N,\ 0,\ 0,\ 0,\ 0)$ where the population is fully susceptible, and move a Susceptible to the Exposed compartment via a point-like external forcing, simulating the return into the area of an individual infected elsewhere.

---

[1] It is a known result that the convolution of any locally absolutely integrable function $f \in L^1_{\text{loc}}(\mathbb{R})$ with a kernel $g \in C^k(\mathbb{R})$ yields a function of class C^k. Since our kernel $\rho \in C^\infty(\mathbb{R})$ we will obtain an analytical function.

[2] Taking any parameter, other than those defining Φ_{SE}, to be time dependent requires great care in model implementation from both an analytical and a numerical point of view in order to avoid retrocausal effects.

5.3.2 | Sensitivity analysis of the model

While the full process used to make predictions will be presented in the following section, we can anticipate that the most of it rests on the tuning, over time, of the sociability parameter $s(t)$ during the epidemic, which has been varied to account for the social restriction measures mandated by the Italian government, for the adoption by individuals of personal protection devices in their social activities (e.g. face masks) and for the environmental conditions, in order to match the weekly trend of new positive cases. The parameter was changed, if necessary, on a weekly basis, in order to match the exponential trend of new positive cases obtained from the AUSL clinical data. A precise estimate of this parameter is critical to the model predictions and its fluctuations may have a relevant effect during the evolution of the epidemic. The quantification of these effects can be performed by computing the sensitivity of the model during the evolution for small perturbations of the sociability parameter.

Considering a perturbation to the $s(t)$ parameter at a time t_0, we start by assuming that at t_0 the prevalence ratio of susceptibles $S(t)/P(t)$ can be approximated as constant in short time scale, i.e. for $\Delta t = t - t_0$ small. This approximation is most accurate for low number of unreported individuals and if we can consider the vaccination process to be slow with respect to the dynamics. We further assume that in the time scale T_U (healing or symptom manifestation time) the $s(t)$ parameter can be considered a constant $s(t) = s$, in a more general case an average value for a short time interval $\simeq T_U$ can be considered. To unburden the notation we also assume to keep constant the relative transmissivity τ and absorb its value in the β factor. Since it is a multiplicative factor as well, the same treatment we are about to develop for the sociability parameter can be applied straightforwardly to τ. Within these approximations it is possible to reduce the system (5.5) to a single delay differential equation, setting $S(t_0)/P(t_0) = n_0 \leq 1$,

$$\dot{U} = \beta n_0 s \left[U(t - T_E) - \int_0^\infty \mathrm{d}\tau \, U(t - T_E - \tau)\rho(\tau; T_U, \sigma_U) \right] \quad \forall t \geq t_0 \quad (5.7)$$

We look for solutions of the dynamics (5.7) in the form $U(t) = U(t_0)e^{\lambda(t_0)(t-t_0)}$. After some algebraic manipulations one gets the condition

$$\frac{\lambda(t_0)}{\beta n_0 s} e^{\lambda(t_0) T_E} = 1 - \int_0^\infty \mathrm{d}\tau \, e^{-\lambda(t_0)\tau} \rho(\tau; T_U, \sigma_U) \, .$$

By substituting the Gamma distribution (5.6), the equation for $\lambda(t_0)$ becomes

$$\frac{\lambda(t_0)}{\beta n_0 s} = \left(1 - \frac{b^a}{(\lambda(t_0) + b)^a} \right) e^{-T_E \lambda(t_0)} \, . \quad (5.8)$$

The epidemic spreads exponentially if the above equation admits a positive solution, whereas the cases decrease if we have a root $\lambda < 0$. On these grounds we call λ the *local Lyapunov exponent* (of the origin) of the system. Indeed in such epidemiological models the global Lyapunov exponent in its standard formulation tends to carry very little information, due to the fact that on long periods of time the dynamics tends to assume a relaxational character towards the post-epidemic equilibrium, which is not a uniquely defined attractor fixed by the system parameters, but depends on the initial conditions of the system. In this sense even if the qualitative character of the final state is the same, one can speak of multi-attractive behaviour. Solving (5.8) in principle can be done via numerical root-finding algorithms, but a closer inspection allows us to determine analytically the region in parameter space where it yields a positive solution. It is straightforward to note that if $\lambda \geq 0$, the second derivative of the r.h.s. of (5.8) is always negative, this means that the slope is always smaller than

$$\frac{d}{d\lambda}\,(\text{r.h.s.})\bigg|_{\lambda=0} = \frac{a}{b} = T_U \ ,$$

and decreases as λ increases. So, a necessary and sufficient condition for the existence of a positive solution to (5.8) is that

$$T_U > \frac{1}{s(t_0)\beta n_0} \quad \rightarrow \quad T_U s(t_0)\beta n_0 > 1 \ . \tag{5.9}$$

Introducing the adimensional parameter $\mu \equiv T_U\lambda$, the relation (5.8) can be written in the form

$$\frac{\mu}{T_U s(t_0)\beta n_0} = \left(1 - \frac{a^a}{(\mu + a)^a}\right)\exp\left(-\frac{T_E}{T_U}\mu\right) = F(\mu) \tag{5.10}$$

We call μ adimensional Lyapunov exponent since it represents the exponential rate of change for the linearized system in a time scale T_U that is the average lifetime of an individual in the unreported compartment: i.e. the time interval during which an individual spreads the infection. It is convenient to consider the quantity

$$r(s) = T_U s \beta n_0 \tag{5.11}$$

so that according to eq. (5.9) if $r(s) > 1$ we have a positive solution of (5.8) and the unreported infected individuals increase exponentially, whereas if $r(s) < 1$ we have a negative solution $\lambda < 0$ and the Unreported compartment decreases. $r(s) = 1$ is the critical value, for which $\lambda = 0$: by construction this condition is satisfied when the Unreported compartment is at its maximal value, i.e. at the peak time of infections, or it can be achieved by applying social activity restriction policies to limit the epidemic spread. It can easily proved, e.g. by following

[26], that $r(s(t_0))$ is the $\mathcal{R}_{t_0}$ parameter of the model, entirely analogous to what we presented in Sec. 5.2.2 for basic models.
The sensitivity analysis of the model considers the effect of local fluctuations of the sociability parameter and how they affect the value of the local Lyapunov exponent in order to estimate the uncertainty in the short term predictions. The susceptivity estimate depends on the derivative $\mathrm{d}\mu/\mathrm{d}s$ computed on the solutions of (5.8). Indeed, a fluctuation Δs in the sociability parameter at a time t_0 introduces an error $\Delta\mu$ in the adimensional local Lyapunov exponent so that the expect variation in the short term prediction reads

$$\Delta U(t_0 + \Delta t) = U(t_0)\exp\left(\mu(t_0, s_0)\frac{\Delta t}{T_U}\right)\frac{\Delta t}{T_U}\frac{\mathrm{d}\mu}{\mathrm{d}s}\Delta s \tag{5.12}$$

The error depends exponentially on the local Lyapunov exponent and increases linearly with Δs. A direct calculation of the susceptivity $\mathrm{d}\mu/\mathrm{d}s$ provides

$$\frac{\mathrm{d}\mu}{\mathrm{d}s} = \frac{\mu(s)}{s(1 - r(s)\mathrm{d}F/\mathrm{d}\mu)} \tag{5.13}$$

If we look at the evolution of the local Lyapunov exponent and its susceptivity along a sample trajectory of (5.5) we observe what follows. The adimensional Lyapunov exponent has a decreasing sigmoid behavior as a function of t (see Figure 5.3) with an inflection point close to the critical value $\mu = 0$. The derivative $\mathrm{d}\mu/\mathrm{d}s$ is continuous at the critical value and has a decreasing sigmoid behaviour as well. This means that the presence of small fluctuations in the sociability parameter $s(t)$ mainly increases the prediction error during the expansion of the epidemic wave, whereas they play a limited role when the herd immunity is reached. From this analysis it becomes also evident that enforcing restrictions on social activities to control the epidemic spread also improves the prediction capabilities of the model, that could in turn be used to optimize the application of the social restriction policies.

5.4 | Epidemic forecasting and data analysis

5.4.1 | Nowcasting the COVID-19 pandemic in the Bologna metropolitan area

As it has been pointed out in Sec. 5.3, several parameters must be fixed in order to perform simulations of the pandemic using (5.5). More specifically, making short-term forecasts using a dynamical model entails adapting its parameters according to a data driven approach, in order to match the dynamical

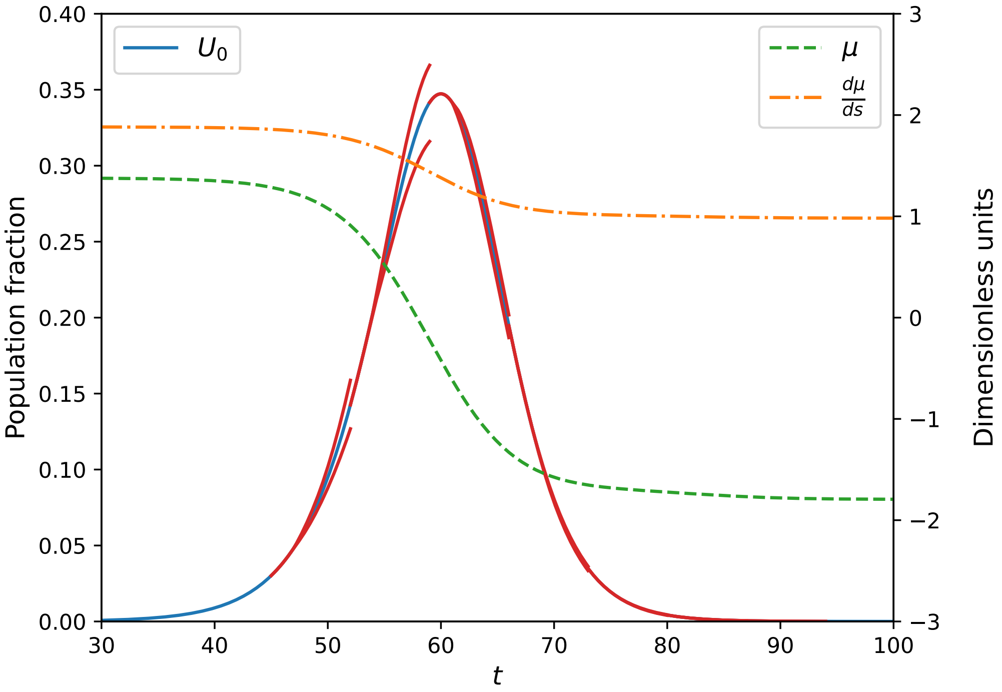

Figure 5.3: Example of epidemic evolution (blue continuous line) using model (5.5) for a fixed value of $\beta = (1.2\,\mathrm{d})^{-1}$ and a baseline relative sociability parameter $s = 0.7$. The red brackets show the variability of weekly forecasts under a ±10% change in the value of m. The dashed green line represents the adimensional Lyapunov exponent μ. The dash-dotted orange line is the local Lyapunov exponent susceptivity $\mathrm{d}\mu/\mathrm{d}s$. Population values are read on the left axis, exponent and susceptivity values on the right. Time on the abscissae is marked in days.

Parameter	Time (days)	σ (days)
T_E	2	–
T_U	5.5	2.3
T_I	21	–
T_R	180	–

Table 5.1: Permanence times of each compartment in the model. The standard deviation σ_U is reported only for the compartment where it is defined.

state at the time of prediction to a decided accuracy and then project it in the near future via the dynamics specified by the model. From this point of view, having many free parameters can result in instability of the estimates, and possibly lead to overfitting phenomena. The value of the reported symptomatic fraction has been fixed to $\alpha = 0.14$ according to the available literature [61], and has been treated as a fixed constant throughout the simulations. The permanence times have been set to the values presented in Table 5.1 and were kept fixed as well. Their values have been taken from literature [58], except for the I compartment, where the value $T_I = 21\,\mathrm{d}$ was chosen in the beginning as it corresponded to the duration of the state-mandated isolation period for individuals who tested positive to SARS-CoV-2 , and has been kept later as an effective duration in order to account for both short-term home isolations and hospital admissions of longer duration. The relative transmissivity τ was changed three times during the simulation, at the times when it was estimated that variants had arrived in Bologna. Fixed in the beginning to a value of $\tau_0 = 1$ it has been changed for the first time on the 20th of October 2020 to a value $\tau_1 = 1.56$ accounting for the increased infectivity of the Alpha variant. Subsequent changing points were on the 1st of April 2021 to a value $\tau_2 = 2.50$ for the arrival of Delta variant and finally to a value $\tau_3 = 12.5$ accounting for the estimated arrival of the Omicron variant on the 1st of December 2021. These values were not obtained from data, but corresponded to values published in periodic bulletins [52] available from the Italian National Health Institute (Italian *Istituto Superiore di Sanità*) Since in the initial stage of the pandemic no social restrictions were in place, also the relative sociability parameter s has been set in the beginning to a value of $s = 1$. This allowed us to obtain the value of β from testing data during the initial exponential growth phase of the cases, as it is unmodulated by the other factors. An exponential fit on the daily new positive cases in Bologna for the first 10 days of data from 24/02/2020 to 04/03/2020 yielded the value $\beta = (0.833 \pm 0.34)\,\mathrm{d}^{-1} \approx (1.2\,\mathrm{d})^{-1}$. Using (5.11) we can compute the value of $\mathcal{R}_0$ in our model, obtaining $\mathcal{R}_0 = 4.6 \pm 1.9$

which is compatible with the value $\mathscr{R}_0 = 2.9 \pm 0.5$ at 95% confidence interval reported e.g. in [15]. Finally, the effect of the vaccination campaign, modeled through the term $\Phi_V(t) = v(t)S(t)$, with $v(t)$ the function quantifying the effect of vaccination in reducing the susceptible population S. The vaccination rate function $v(t)$, which lowers the number of susceptible individuals because of immunization, was set to 0 up to the 28th of December 2020 and its value was afterwards updated to the vaccination rates provided by the local health unit on a weekly basis. This leaves the relative sociability parameter $s(t)$ as the only free parameter of the model, around which our prediction strategy was constructed. The relative sociability parameter s was defined as a piecewise constant function and varied on an approximately weekly basis during two years from the beginning of COVID-19 epidemic, in order to minimize the difference between predicted and observed new cases of infections (i.e. considering the incoming flow into the I compartment). To formalize the procedure we write the sociability function as

$$s(t) = s_n \quad \forall\, t_n^* \le t < t_{n+1}^*$$

where $\{t_0^* = 0,\ t_1^*,\ \ldots,\ t_n^*,\ \ldots,\ \infty\}$ is the sequence of the changing times of the function (with the change at infinity being included for consistency with the definition) and $\{s_0 = 1,\ s_1,\ \ldots,\ s_n,\ \ldots,\ s_\infty\}$ its constant values. If we consider a new variation being introduced at a time t_n^* we select the new value through a grid search, performed with a granularity of 10^{-2}, selecting the optimal point as the minimizer of the weekly RMSE, i.e.

$$s_n = \underset{s=s_{n-1}+10^{-2}[-\Delta,+\Delta]}{\arg\min} \frac{1}{\sqrt{7}} \left[\int_{t_n^*+T_{\text{eff}}}^{t_n^*+T_{\text{eff}}+7} \mathrm{d}t\, (\Phi_{\text{model}}(t;\, s) - \Phi_{\text{data}}(t))^2 \right]^{1/2} \tag{5.14}$$

where $\Phi_{\text{data}}(t)$ is the weekly running average of the measured new positives at time t, t_n^* is the beginning of the n-th constant interval in the piecewise sociability function, $\Phi_{\text{model}}(t)$ is the flow of new isolated cases estimated by the model and Δ is the maximum allowed number of optimization steps [3] away from the previous sociability value. By denoting the $\Phi_{\text{model}}(t; s_n = s)$ we intend that we are keeping all sociability values fixed up to s_{n-1} and varying s, i.e. the s_n candidate to minimize the RMSE. Notice how we have to insert an offset $T_{\text{eff}} = T_E + T_U$ in the integration limits, since to start noticing the effect of a change in the parameter at t^* we need to wait approximately T_{eff},

---

[3] This quantity has changed through the period during which forecasts were being made, as sometimes very strong restrictions, or the lifting thereof, made large variations necessary. Nevertheless, the values were always selected that allowed the best accord with data through a minimal perturbation of the sociability parameter.

i.e. the average time between exposition to the pathogen and manifestation of symptoms, before we see any effects. Therefore, using a data driven approach such as the one described so far, applied in the Metropolitan area of Bologna during the COVID-19 pandemic, when a time series of the incoming flow to the I compartment is available from the observations, it is possible to infer the value of $s(t)$. To mitigate the risk of overfitting, the levels of $s(t)$ were generally tuned in correspondence of changes in the sociability restriction policies applied in Italy during the COVID-19 epidemic, or changed as a consequence of wide-impact social events (such as the reopening of schools), but small weekly modifications in the social activity parameter could often be necessary for unpredictable causes. In Fig. 5.4 we show how the model (5.5) was able to reproduce the observed new reported infected during the first two years of COVID-19 epidemic. The Mean Absolute Error (MAE) achieved by the model is 42 patients (RMSE = 97 patients) over a study duration of 866 days. As discussed in Sec. 5.3.2 and showcased in Fig. 5.3, the possibility of performing accurate short-time predictions is sensitive to fluctuations of the $s(t)$ parameter and hence strictly related to the possibility of estimating the parameter accurately using the real-time observed data. One of the foremost disturbances in the regression was related to the time delay between the sociability changes and their effect in the new detected infected and despite the good interpolation of the observed data, the short term predictions were sometime affected by this fact. Therefore the possibility of having a precise, ideally *a priori*, measure of the sociability parameter is a fundamental step in the deployment of predictive models that could allow to mitigate the spread of epidemics like COVID-19 where the number of unreported infected individuals has a relevant role. In the next section we show how mobility data could be used as a proxy for a real time estimate of the changes in the sociability parameter, thus potentially improving the predictivity of the model.

5.4.2 | Construction of a proxy for the sociability parameter using mobility data

The mobility data used for this study are part of the “Open Data Bologna" project of the Bologna township [78–80], which is an open access repository containing several datasets, among which are traffic flows data with a hourly resolution, measured from 292 magnetic coils in the city of Bologna and in the Bologna metropolitan area. The available data cover the full span of the study from year 2020 through 2022. Our working assumption is that traffic flow data are a proxy of the level of social activity taking place in the city, one of the foremost contribution to the spreading of the COVID-19 epidemic and

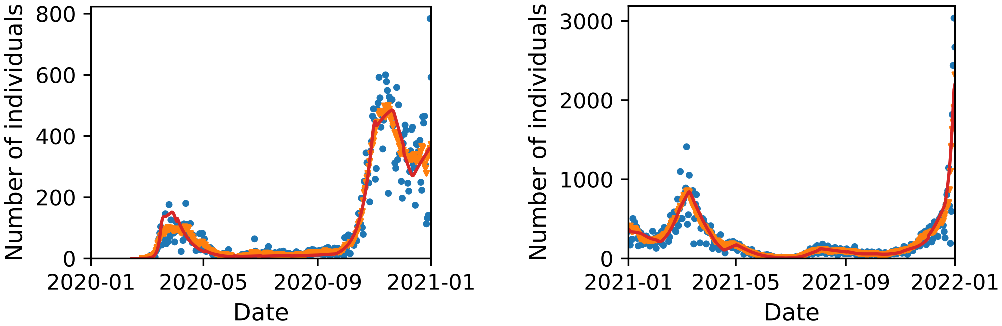

Figure 5.4: The blue dots are the daily number of new positive recorded in the metropolitan area of Bologna (AUSL dataset) whereas the orange triangles are a running average over a week. The red curve is the data-driven model simulation results inferring the sociability parameter. Note the different scales in the two timespans due to the increase efficiency in the detection of the new positive during the epidemic waves.

the only free parameter in (5.5), thus we expect that changes in the traffic flows will correspond to changes in the social activity levels. The interest in this approach lies in the fact that while the mobility data are easily measurable and often made available under open data policy initiatives, it is quite difficult to estimate a-priori the levels of social activity in a population. To build the proxy we apply a weekly moving average to the data, in order to mitigate the periodic fluctuations corresponding to the natural weekly cycle of mobility (e.g. a drop in the weekends due to the reservation to pedestrians of various areas). Finally, the total traffic flow was normalized to a maximum value of 1 at the local maximum anterior to the start of the COVID-19 pandemic, so to match it to the value of the relative sociability parameter at the beginning of the simulation. We define this rescaled value as the mobility index $m(t)$. In Fig. 5.5 we show the mobility index derived for the traffic flows time series. With the onset of the first national lockdown (march 2020, first red shaded region of 5.5), the traffic flow index undergoes a drop to $\simeq 20\%$ of the initial value. Upon lifting of the national lockdown, several restrictions were kept in place to mitigate the resurgence of cases, with a corresponding growth of the mobility index to values that remained smaller than the pre-pandemic ones (a reduction approximately to the 80% of the pre-COVID value in June 2020) that could also give an interesting estimate of the impact of measures such as remote working on the urban traffic of Bologna. The regional-scale introduction of pandemic severity-dependent restrictions and curfews (Autumn 2020) in Italy is marked by the second red shaded region in Fig. 5.5 and corresponds to a mobility index value around the 70% of pre-pandemic levels. A further reduction in mobility

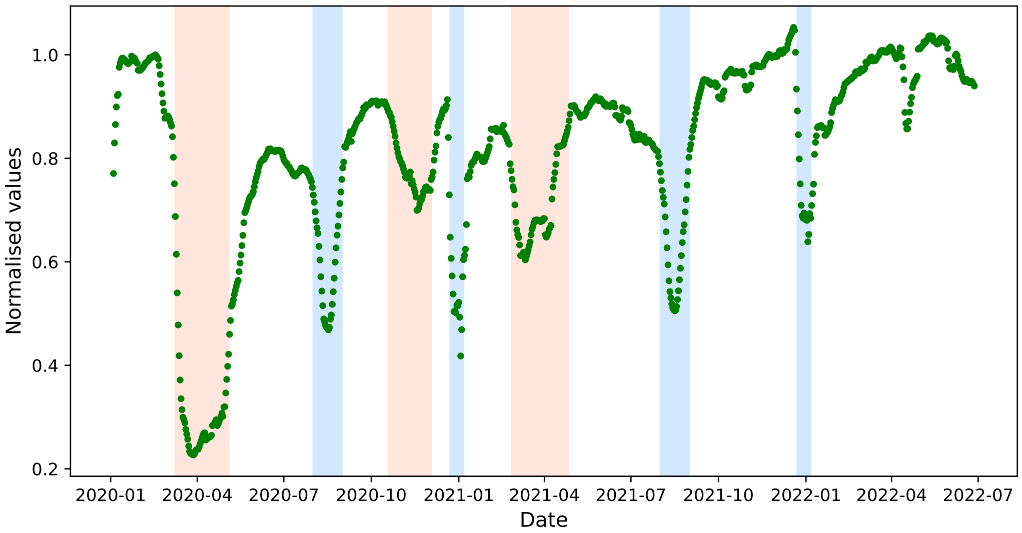

Figure 5.5: The red-shaded areas mark in, in chronological order: the Italian national lockdown during the first epidemic wave, from the 3rd of March to the 4th of May 2020, a set of government-mandated countermeasures during the second pandemic wave, such as the shutting down of in-presence commercial activities, the introduction of night curfews and of pandemic severity-based color-coded regions from the 19th of October 2021 to the 3rd of December 2020 and winter-time restrictions from the 26th of February to the 26th of April 2021. The blue-shaded areas mark winter holidays and the month of August, which is a typical month for company holiday periods in Italy.

is measured in March and April 2021, this period corresponds to the enactment of some restrictions on social activities by the national authorities. Ulterior particularly localized trends may reflect the behavior of individuals, also influenced by the news, social media and personal risk perception. Other oscillations are observed in conjunction with holiday periods, shaded in blue in Fig. 5.5, during summer (August 2020 and 2021) or the end of the year (Christmas holidays). In the case of Christmas holidays, the decrease is often preceded by a short and sudden increase in the mobility time series, likely related to Christmas shopping. The mobility drop during holiday periods can be also the consequence of the population leaving the the Bologna area. We finally observe a global trend to recover the initial value of the mobility index during the course of the pandemic, which is approximately re-achieved around December 2021.
A slightly more elaborate version of model (5.5), accounting for a very simple hospitalization dynamics (i.e. a dynamics completely internal to the I compartment, which has not been presented for simplicity) has been used to weekly

predict the number new positive and the hospitalizations in the metropolitan area of Bologna during COVID-19 epidemic. The model provided reasonable short term predictions of epidemic evolution on a city spatial scale. We intend to perform a comparison of the inferred piecewise constant $s(t)$ parameter and the $m(t)$ time series obtained from the data, to understand to which extent we can treat the latter as a proxy for the former. The use of the mobility index as a proxy of the social activities is justified by the fact that among the containment measures implemented during the pandemic, there were mobility restrictions and the implementation of remote-working whenever possible, which are both aspects we expect to be able to retrace in the urban mobility. A direct comparison of the mobility index and the inferred values of $s(t)$ during more than two years from the outbreak of the pandemic is made in Fig. 5.6.

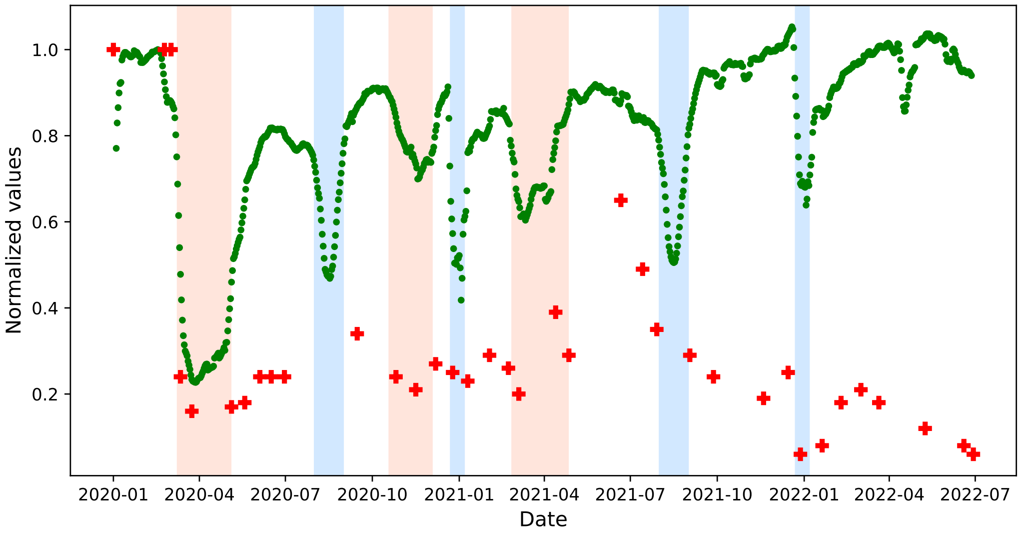

FIGURE 5.6: Comparison between the inferred sociability parameter $s(t)$ (red crosses) and the weekly running average of the normalized daily mobility, i.e. the mobility index $m(t)$ (green dots). The shaded regions mark the the same events as in Fig. 5.5.

5.4.3 | The role of social activity regulations

At the start of the first lockdown (first red shaded area) the mobility index and the inferred sociability s have roughly the same behaviour, so that the values of $m(t)$ could have been taken as a good estimate for $s(t)$. However, once the mobility restrictions are partially lifted (May 2020), we start to observe a systematic mismatch between the mobility index value and the sociability parameter. While the $m(t)$ time series goes back to $\approx$ 80% the pre-pandemic

Day	Event	Shift
18/05/2020	Activities reopening (bars, restaurants)	0.58
17/05/2021	Delta variant in Emilia Romagna	0.23
15/09/2021	Schools reopening	0.71

Table 5.2: Breakpoints for the correlation analysis between sociability and mobility indexes. The values in the Shift column were added separately (not cumulatively) to the baseline sociability index.

mobility value, the $s(t)$ parameter remains much lower, only slightly above the lockdown level. Possible explanations could be a radical change in the population's behaviour during social activities due to regulations, such as the compulsory use of respiratory masks, which reduce drastically the risk involved in social contacts, nonetheless allowing most social activities to happen. The discrepancy between the two indices can be removed by introducing a systematic additive shift $s \mapsto s + 0.58$ without changing the relative fluctuations. The results shown in Fig. 5.7 suggest that, after the shift, the mobility index fluctuations are still able to reproduce the changes of the sociability parameter, even if care should be taken regarding mobility index drops during holiday periods. The introduction of the shift allows better agreement over a period of almost a year, after which it is likely that the effect of the vaccination campaign, the Delta variant (black line in Fig. 5.7) and the warmer summer climate changed the contagion dynamics, thus requiring a smaller shift of $s \mapsto s + 0.23$. This smaller mismatch can be interpreted as the result of a possible diminished compliance with social distancing and respiratory hygiene practices on the one hand and of a faster environmental degradation of the pathogen due to the warmer temperatures. To this it shall be added that the number of new positive recorded during Summer 2021 was very low (see e.g. Fig. 5.4 right), conditions that make compartmental models generally less reliable. In the early autumn of 2021 a resurgence of the epidemic is observed, that can likely be attributed to the reopening of schools (see Table 5.2), and the realignment of the sociability index s with the mobility m requires a positive shift of the former of an amount 0.71. Finally we observe that, in early 2022, the empirical sociability parameter starts to decrease and there is no apparent correlation with the mobility index despite the shift. However at that time the epidemic dynamics was complicated by the presence of several variants and the heterogeneous effects of vaccination coverage in the population so that the simple compartmental model (5.5) was likely not able to capture the epidemic evolution correctly any longer. An interesting perspective offered by these results is that they could allow a quantification of the impact on the epidemic spread of the measures increasing social distancing, such as the use of face masks or the crowding limit in public locations. For example, after the first lockdown of 2020, the effective reduction in the contagion probability is almost a factor 4, while a comparable mobility of individuals on the metropolitan area scale was restored with respect to pre-pandemic levels. The measurement of the effect of these policies at the beginning of the COVID-19 epidemic spread could have been a useful *quantitative* guide for government officials, e.g. when evaluating the necessity of a complete lockdown versus other effective strategies with a lower economic impact.

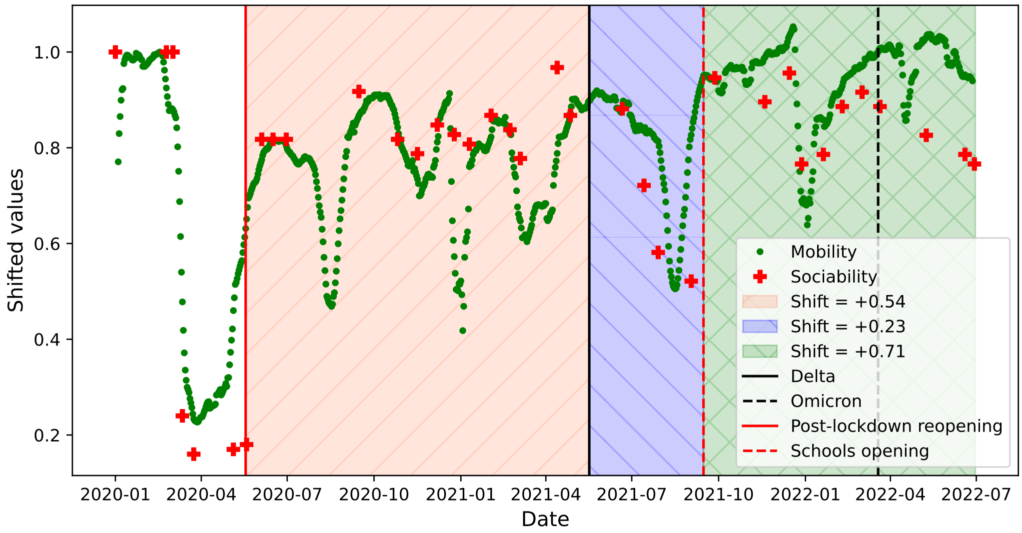

FIGURE 5.7: The shifted piece-wise constant sociability rate function s (red crosses) is plotted against the mobility data (green dots). The shaded regions refer to different shifts applied to the sociability rate (see legend).

5.4.4 | Estimation of the effects of sociability fluctuations on the accuracy of predictions

We can use the findings of Sec. 5.3.2 to estimate the amount by which the accuracy of our prediction will be afflicted by fluctuations in the sociability parameter $s(t)$. To follow the pandemic course in Bologna the parameter has been adjusted weekly, regressing with respect to the number of new cases in the Metropolitan area, thus defining over time a piecewise constant function. The levels of the piecewise constant function are solutions to the optimization problem (5.14), which is solved every time a new sociability level is introduced.

Since the new positive cases are the Unreported individuals that develop symptoms and are isolated, we identify

$$\Phi_{\text{model}}(t) = \alpha \int_0^\infty \mathrm{d}\tau \; \rho(\tau; T_U, \sigma_U) \Phi_{EU}(t - \tau)$$

which is the incoming flow for the I compartment, where we have denoted $\Phi_{EU}(t) = \Phi_{SE}(t - T_E)$. Our aim is to quantify how large can the fluctuations in $s(t)$ be, while causing a relative fluctuation in our prediction of the new cases $\Delta\Phi_{\text{model}}(t_0)/I(t_0)$ below a certain accuracy threshold which we may decide to set. We can formalize the problem as follows: let us consider a positive instant $t_0 > 0$ during the evolution of the model, at which we decide to readjust the sociability parameter to fit better the clinical data. To do so, we solve the optimization problem (5.14) for s, and obtain a value s^*, which is our best guess for the new sociability level. Let us then consider an ensemble of simulations, all identical to each other until time t_0, in particular with the same piecewise-constant sociability function up to that time, and let us perturb, in each copy of the simulation, the sociability for $t > t_0$ with a value drawn from a Gaussian distribution $\mathcal{N}(0, \sigma)$, i.e. for each simulation let us take

$$s^* \mapsto s^* + \Delta s, \qquad \Delta s = \mathcal{N}(0, \sigma).$$

We then evolve the simulations for the $T_{\text{eff}} + 7$ days necessary to solve problem (5.14), and calculate the quantity

$$\sigma_{\text{model}}(t_0) = \int_{t_0 + T_{\text{eff}}}^{t_0 + T_{\text{eff}} + 7} \mathrm{d}t \, \sqrt{\langle \Phi^2_{\text{model}}(t; s^* + \Delta s) \rangle_{\Delta s} - \langle \Phi_{\text{model}}(t; s^* + \Delta s) \rangle^2_{\Delta s}}, \tag{5.15}$$

i.e. the ensemble standard deviation of the predicted new positives, averaged over the prediction period of a week starting from $t_0 + T_{\text{eff}}$. Up to the further normalization over $I(t_0)$ this is to all effects the standard deviation of the fluctuations in the new positives induced by a sociability random perturbation. With these definitions in place, we can ask the question of how large we can take σ in the sociability parameter perturbation while still having $\sigma_{\text{model}}(t_0)/I(t_0) \leq r$ where we denote by r the chosen threshold value.

The estimation of fluctuations in the compartments is a typical question addressed via linear response theory, which we considered for the model at hand in subsection 5.3.2. Indeed according to our results, and considering a localized variation Δs at time instant t_0, we can write

$$\Delta U(t_0 + \Delta t) = U(t_0) \exp\left(\mu(t_0, s_0) \frac{\Delta t}{T_U}\right) \frac{\Delta t}{T_U} \frac{\mathrm{d}\mu}{\mathrm{d}s} \Delta s \tag{5.16}$$

which corresponds to (5.12). This is the linear response approximation for the fluctuation in the population of the Unreported compartment induced by a change Δs of the sociability parameter. If we consider $\Delta s = \mathcal{N}(0, \sigma)$ we can take the variance on both sides

$$\mathrm{Var}\left[\Delta U\right](t_0 + \Delta t) = U^2(t_0)\exp\left(2\mu(t_0, s^*)\frac{\Delta t}{T_U}\right)\frac{\Delta t^2}{T_U^2}\left(\frac{\mathrm{d}\mu}{\mathrm{d}s}\right)^2\sigma^2 \tag{5.17}$$

This is not completely satisfactory, though, because our regression has been performed on the newly isolated infected patients, the only infection data available with a reasonable accuracy, and these correspond to a fraction α of the outgoing flow from the Unreported compartment. The relationship between the flow and the compartment is

$$\dot{U}(t) = \Phi_{EU}(t) - \int_0^\infty \mathrm{d}\tau\ \rho(\tau; T_U, \sigma_U)\Phi_{EU}(t-\tau) \tag{5.18}$$

where Φ_{EU} is the Exposed-Unreported flow and ρ_U is the Gamma distribution of the permanence time within the Unreported compartment, with parameters as explained in section 5.3. By introducing the linear integral operator $\mathscr{L}$

$$\mathscr{L}\left[f\right](t) = \int_0^\infty \mathrm{d}s(\delta(s) - \rho_U(s))f(t-s) \equiv \int_0^\infty \mathrm{d}s g(s)f(t-s)$$

we can recast (5.18) as

$$\dot{U}(t) = \mathscr{L}\left[\Phi_{EU}\right](t) \tag{5.19}$$

we can formally invert the flow-compartment relationship as

$$\Phi_{EU}(t) = \mathscr{L}^{-1}\left[\dot{U}\right](t) \tag{5.20}$$

such an inversion, technically referred to as a *raw deconvolution* problem, is usually tackled exactly via a Laplace transform.

By linearity of $\mathscr{L}$, the relationship between fluctuations in the flow and the compartment derivative caused by a parameter change has the same form of (5.20), i.e. $\Delta\Phi_{EU}(t) = \mathscr{L}^{-1}\left[\Delta\dot{U}\right](t)$. A direct calculation provides for $\Delta\dot{U}$

$$\Delta\dot{U}(t_0 + \Delta t) = U(t_0)\exp\left(\mu\frac{\Delta t}{T_U}\right)\left(\frac{\mu\Delta t}{T_U} + 1\right)\frac{\mathrm{d}\mu}{\mathrm{d}s}\frac{\Delta s}{T_U}, \tag{5.21}$$

for the sake of clarity in the following let us collect $\kappa = U(t_0)\frac{\mathrm{d}\mu}{\mathrm{d}s}\frac{\Delta s}{T_U}$ and perform the scaling $\mu\Delta t/T_U \mapsto t$, so that the linear response law for the time derivative of the U compartment reads

$$\Delta\dot{U}(t) = ke^t\,(t+1)\,. \tag{5.22}$$

By the properties of the Laplace transform, which we denote for a function $f(t)$ as $\widetilde{f}(\ell)$, we can recast (5.20) for the case of the fluctuation as

$$\widetilde{\Phi}_{EU}(\ell) = \widetilde{\Delta\dot{U}}(\ell)/\widetilde{g}(\ell) = \frac{\kappa\ell}{(\ell-1)^2\left(\frac{b^a}{(\ell+b)^a}+1\right)} \tag{5.23}$$

Taking the antitransform of the r.h.s. of (5.23) will yield the linear response law for the flow perturbation. In light of recent developments [32], it is likely possible to leverage results from fractional calculus and at least express the antitransform in a convolution form, but further investigation is necessary.
For this reason we trace back to (5.18) applied to fluctuations and try to work out an approximation. We start by expanding the integral in the central moments of the distribution $\rho(t; T_U, \sigma_U)$. Keeping the contribution at lowest order we get

$$\Delta\dot{U}(t) = \Delta\Phi_{EU}(t) - \Delta\Phi_{EU}(t - T_U). \tag{5.24}$$

In this simplified version of the fluctuation dynamics the outgoing flow, in which we are interested, is just a delayed version of the incoming one. For this reason it is easier to study the latter, and take its scaled and delayed value as the rate of new identified infected people. Isolating $\Delta\Phi_{EU}$ from (5.24), and identifying $t = t_0 + \Delta t$ as it is intended in the formulation of the argument, we get

$$\Delta\Phi_{EU}(t_0 + \Delta t) = \Delta\dot{U}(t_0 + \Delta t) + \Delta\Phi_{EU}(t_0 + \Delta t - T_U). \tag{5.25}$$

On causality grounds, any term in the previous formula is identically 0 when evaluated with an argument smaller than t_0. For this reason, in the whole interval $\Delta t \in [0,\ T_U[$, the flow fluctuation $\Delta\Phi_{EU}$ corresponds to the fluctuation in the compartment time derivative. For larger $\Delta t \in [T_U, 2T_U[$ we must include an additional delayed term, but this eventually is just the derivative perturbation evaluated at an earlier time. At longer delays $\Delta t \in [nT_U, (n+1)T_U[$ we will have to consider n additional terms, which can all be lead back to the derivative perturbation in the first interval[4].

$$\Delta\Phi_{EU}(t_0 + \Delta t) = U(t_0)\frac{\mathrm{d}\mu}{\mathrm{d}s}\frac{\Delta s}{T_U}\sum_{k=0}^{\lfloor \Delta t/T_U \rfloor}\exp\left(\frac{\mu\Delta t}{T_U} - k\mu\right)\left(\frac{\mu\Delta t}{T_U} + 1 - k\mu\right) \tag{5.26}$$

where $\lfloor\cdot\rfloor$ denotes the floor function, i.e. the truncation to the closest smaller integer. While (5.26) is the linear response law for the incoming flow into the Unreported compartment, we need to delay it of T_U to obtain the law for the

---

[4] To this it shall be added that, for a nonlinear system, linear response theory will yield sensible results only for short durations of time so that reasonable evaluation of the flow perturbation will contain just few terms.

outgoing flow. Moreover, if we scale it by the symptomatic cases ratio α we obtain

$$\Delta\Phi_{\text{model}}(t_0+\Delta t) = \alpha U(t_0)\frac{\mathrm{d}\mu}{\mathrm{d}s}\frac{\Delta s}{T_U}\sum_{k=1}^{\lfloor \Delta t/T_U \rfloor}\exp\left(\frac{\mu\Delta t}{T_U}-k\mu\right)\left(\frac{\mu\Delta t}{T_U}+1-k\mu\right) \tag{5.27}$$

which is a sensible expression only for $\Delta t > T_U$ on causality grounds, i.e. because we cannot observe the outgoing perturbation before at least a permanence time has elapsed. For consistency therefore we set

$$\Delta\Phi_{\text{model}}(t_0+\Delta t) = 0 \quad \forall \Delta t < T_U .$$

By bringing Δs to denominator we get the susceptivity of $\Delta\Phi_{\text{model}}$ with respect to sociability

$$\frac{\Delta\Phi_{\text{model}}(t_0+\Delta t)}{\Delta s} = \frac{\alpha U(t_0)}{T_U}\frac{\mathrm{d}\mu}{\mathrm{d}s}\sum_{k=1}^{\lfloor \Delta t/T_U \rfloor}\exp\left(\frac{\mu\Delta t}{T_U}-k\mu\right)\left(\frac{\mu\Delta t}{T_U}+1-k\mu\right), \tag{5.28}$$

which is set to 0 for $\Delta t < T_U$. This susceptivity provides the scaling factor that relates a fixed perturbation of the sociability parameter Δs at time t_0 with its effect after a time interval Δt on the flow of newly infected isolated patients in the model. In particular this allows us also to compute the quantity $\sigma_{\text{model}}(t_0)$ without performing an ensemble of simulations, but directly from the ensemble standard deviation σ. The explicit calculation reads

$$\begin{aligned}
\sigma_{\text{model}}(t_0) &= \int_{T_{\text{eff}}}^{T_{\text{eff}}+7}\mathrm{d}t\left|\frac{\Delta\Phi_{\text{model}}(t_0+t)}{\Delta s}\right|\sigma \\
&\approx \sigma\frac{\alpha U(t_0)}{T_U}\frac{\mathrm{d}\mu}{\mathrm{d}s}\int_{T_U}^{2T_U}\mathrm{d}t\left(\frac{\mu t}{T_U}+1-\mu\right)\exp\left(\frac{\mu t}{T_U}-\mu\right) \\
&= \frac{\alpha U(t_0)}{T_U}\frac{\mathrm{d}\mu}{\mathrm{d}s}e^{\mu}\sigma,
\end{aligned}$$

where we have approximated $T_{\text{eff}} \approx T_U$, $T_{\text{eff}}+7 \approx 2T_U$ to obtain a more manageable final form. Dividing by $I(t_0)$ we can write down an explicit formula for the standard deviation of the sociability perturbations as a fraction of the current positive cases

$$\frac{\sigma_{\text{model}}(t_0)}{I(t_0)} = \frac{\alpha U(t_0)}{I(t_0)}\frac{\mathrm{d}\mu}{\mathrm{d}s}\frac{e^{\mu}}{T_U}\sigma. \tag{5.29}$$

The problem in applying the above formula rests in the fact that $U(t_0)$ is by construction an unobservable compartment, so that in real application cases one has no means of comparing the simulated value with data. For this reason, we approximate $U(t_0)/I(t_0) \approx \alpha/(1-\alpha)$. We can now bound from above $\sigma_{\text{model}}/I(t_0) \leq r$ with the acceptable error threshold r and solve for σ

$$\sigma \leq \frac{T_U e^{-\mu}}{1-\alpha}\left(\frac{\mathrm{d}\mu}{\mathrm{d}s}\right)^{-1} r. \tag{5.30}$$

Formula (5.30) estimates the maximal acceptable fluctuation in the sociability for the prediction fluctuation of new positives to remain below a fraction r of the current number of isolated patients. To gain an insight on the values at play, using the physical values for β, α and the delays, we evaluate the equality value for σ given by (5.30) as a function of the Susceptibles concentration n_0 and the mean sociability value s_0 around which the fluctuations oscillate. In Fig. 5.8 we show the maximal σ that keeps the prediction fluctuations below a value of $r = 10\%$ of the value of isolated patients. The emerging interpretation is interesting and potentially relevant for policy makers. Indeed we are able to see

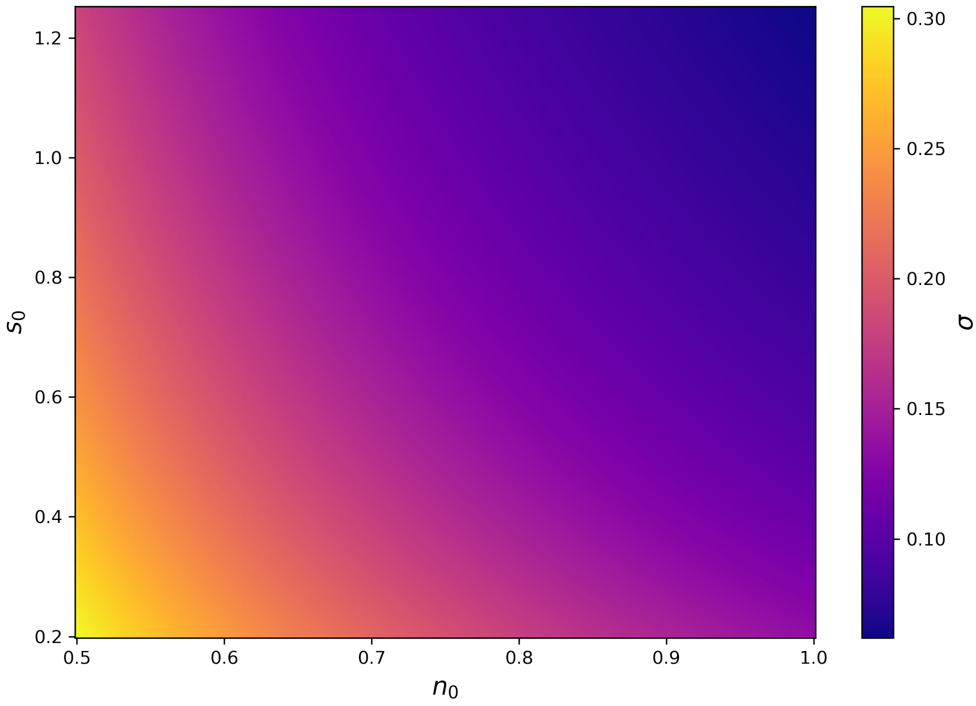

Figure 5.8: Heatmap of the maximal acceptable sociability fluctuation σ yielding an average new positives prediction error relative to the current Isolated Infected patients inferior to $r = 10\%$.

that for high concentrations of susceptibles and high sociabilities the admissible fluctuation is quite low, tending to 0, as the system is at its highest sensitivity in these conditions. If we decrease the concentration of susceptibles we observe a higher tolerance to fluctuations, as the system is inherently less reactive. The trend of the tolerance increase is quicker for lower sociabilities, as the foremost contribution to new infection comes still from the mean value.
These findings highlight a double implication for policy making and the planning of response strategies to pandemic events. On the one hand these response estimates are a valid instrument when evaluating the necessity of strict containment measures. Indeed measures such as complete lockdowns have a high economic impact and a considerable social cost for individuals, and their deployment should be mandated with great care. Our analysis shows in this regard that these are most effective in the initial stages of the pandemic, i.e. for large n_0, where imposing a low s_0 allows the system to accommodate some degree of sociability fluctuations while keeping their influence limited. On the contrary once the pandemic peak has passed or vaccines have been deployed, i.e. for lower values of n_0, our analysis shows that a higher average sociability can be restored without amplifying the effects of fluctuations on predictions. On the other hand, our results have implications concerning the importance of contact tracing and case reporting in the different phases of the pandemic, to ensure accurate predictions. What Fig. 5.8 tells us in this regard is that accurate positive reporting is paramount in the early stages, where even an arbitrarily small fluctuation can significantly alter model predictions. In the later stages of a pandemic wave, instead, we expect that even less resolute tracing and testing campaigns will suffice to follow with reasonable accuracy the development of epidemiological events. In the present state of affairs, the design of management strategies for pandemic phenomena on regional and national scales must indeed not only consider the significant economical endeavour of testing, tracing and reporting infrastructures, but also carefully address the understandable growing concern among citizens on privacy and personal data processing. For these precise reasons we believe our contribution can be a valuable aid in quantifying trade-offs between various approaches in responding to pandemic events.

5.5 | Conclusion

In this chapter we present our approach to the problem of short term forecasting the evolution of the COVID-19 epidemic in the metropolitan area of Bologna using a simple compartmental model based on delay differential equations and a data driven approach. The available data consisted of new positive cases recorded daily by the testing campaign, and further during the course of the pandemics, of the daily number of vaccinated individuals. With this knowledge, the sociability parameter of the model was tuned on a roughly weekly basis to match the trend of new cases, and taking into account the social restriction policies applied by the central government to get weekly forecast of the epidemic evolution. While the introduction of explicit delays in the model is fundamental for capturing the evolution of the COVID-19 spread, the reliability of the predictions suffers from the delay between the changes in social activity and its impact on new positives. Indeed, we show that a theoretical computation of local Lyapunov exponent and its susceptivity allows an estimate of the predictability error due to the fluctuations of the sociability parameter, and that especially in the initial stages of a pandemic wave data quality is paramount to adequate predictions. Hence we expect that the predictivity of the model would enjoy a great improvement with the introduction of a real time measure of the social activity. Comparing the traffic data recorded by a system of magnetic coils in the city of Bologna and the time series of the sociability parameter $s(t)$ inferred by the model (5.5) from the new positive individuals time series, we show that the urban mobility index can be a good and robust proxy of the sociability parameter fluctuations, at least on a medium range of prediction. At the beginning of the epidemic there is a strong correlation between mobility and social activities since strong mobility restrictions were the main measures implemented by the central government to control the spread of the epidemic. However, the introduction of other mitigating measures which do not impact directly mobility, but are related to people behaviour during social activities (i.e. sanitary masks, willing reduction of social contacts, crowding limits for enclosed spaces), paired with the lifting of lockdowns, seems to introduce a discontinuity in the observed correlation. One can take into account of the discontinuity by shifting the sociability parameter to recover a quite good correlation between the fluctuations of the two time series for a period of almost one year, up to the summer 2021. At this point a smaller shift must be considered, up to the reopening of schools in September 2021, possibly accounting for the reduced care in observing respiratory hygiene and social distancing and the environmental effect on the basis transmissivity of the virus. After the summer 2021 when there was a resurgence of the epidemic, the scenario changes again both for the effect of the vaccination campaign and emergence of new virus variants. A new shift value is required to match the mobility data: these recover almost the pre-COVID values whereas the sociability parameter has a small increase. By this final shift we recover a correlation up to the beginning of 2022 when the pandemic began to draw to a close, at least for the dynamics captured by our model. These findings point to the fact that a proxy for the sociability parameter can be constructed from mobility data, provided that soft containment measures are not varied too greatly during the period of prediction, otherwise a realignment will be needed. The relevance of these findings rests particularly in the fact they could provide a first approach for the quantitative inference of the effect of containment measures, especially when these are adjusted and introduced continuously with respect to the propagation time scales of a pandemic, which has been recognized as difficult task [3] in general. Moreover, if one assumes that mobility data can estimate up to a normalization the social activity in an area of interest, the shift needed to match inferred and measured data could quantify the difference between the overall rate of contact and that of unprotected contacts, that contribute to the dynamics of contagion, which can in some sense estimate in turn the compliance of the population with mandated measures. The quantification of the shift, in addition, suggests that even softer measures, such as those in place after the lifting of the first lockdown, had a strong effect (a reduction of a factor $\simeq 4$ of the relative sociability parameter) on mitigating the contagion diffusion during social activities. Furthermore, it may be argued that once a strong lockdown is in place, softer measures are scarcely effective (e.g. the widespread adoption of face masks has a limited additional effect if most people are home confined in the first place). We would therefore like to remark that in a future scenario of a quick-spreading pandemic disease, dynamical models, used in conjunction with mobility data in data-driven approaches, could be an important asset for policy making and the optimization of control strategies, in particular by providing quantitative predictions to compare different measures.

Conclusion

In the present thesis we have examined the emergence and the role that delay effects play in the context of Complex Systems, and the possibility to model them by using DDEs as effective equations for collective states. In the first part of the thesis we have focused our attention on problems originating from the field of neurobiological modeling.
In **Chapter 2** we have shown how in the context of directed networks, loop structures can give rise to stationary soliton-like waves, which we conjecture to originate in a similar way to Non Equilibrium Steady States upon breaking of a detailed balance condition in a master equation. We are able to show numerically that the soliton wave in a directed loop arises in analogy to an attractive limit cycle in a DDE with an explicit feedback term, and the two solutions correspond, so that an interpolation of the DDE solution yields a solution to the networked system. By studying the solution dependence on the inherent timescale separation of the FitzHugh-Nagumo, a task made much simpler by the DDE analogue of the chain system, we are able to elucidate that it plays a fundamental role in the definition of the solitonic state, as a scaling of ε is to some extent analogous to one of the global coupling. The physical interpretation of this fact is that the properties, and even the existence, of this type of solution, rests fundamentally on the interplay of local timescales, linked to the reactivity time of a single neuron, and propagation timescales affecting the global coordination of the solution, regulated by the coupling strength. The natural outlook of this work rests in the extension of these findings to more elaborate network structures, in order to see how much of a full network's dynamics can be disentangled by looking at the role of loops. Furthermore, the universality of such behaviour holds some interest in itself. This type of saddle-node bifurcation of limit cycles, is observed in several other systems, such as traffic models [68], where the origin of the bifurcation is in an interaction of explicit delays on a network. The particular interest in this mechanism of stabilization rests also in its interpretation from a functional viewpoint. The most common bifurcation for the birth of an attractive limit cycle, the Hopf bifurcation, is indeed a quite destructive phenomenon, as a global fixed point of the system,

i.e. a physical equilibrium, must loose stability in order to let self-sustained activity arise, while a saddle node bifurcation of limit cycles leaves the phase space untouched, save for a tubular neighbourhood of the cycle itself, so that other invariant manifolds can survive the bifurcation hardly, if at all, affected by it. If we interpret the dynamical states as playing functional roles for a self-organized system, we can conjecture that the introduction of new functions, i.e. the bifurcation of solutions, will be favoured to happen without an excessive perturbation or destruction of the other ones, i.e. pre-existing attractors. This functional interpretation could be particularly interesting to consider when related to reservoir computing models, in order to connect it intuitively with the capabilities of a network of neurons to perform computation and information processing tasks.

In **Chapter 3** we have developed and expanded our intuition on delay induced bifurcations by formulating a simple nonlinear model. Our findings clarify the interplay between the natural frequencies of a dynamical system and a delayed feedback in the presence of quasi-invariant orbits. In particular we elucidate how, for systems that do not possess a dense frequency spectrum, the principal bifurcation parameter is the difference between the quasi-invariant orbit period and the feedback delay, and a skewness condition is required on the coupling with the delayed term, at least when the system is cast in normal coordinates. This is in contrast with previous theories [82] introduced for chaotic systems but often applied in general, which assume that the difference is infinitesimal or vanishing, while we have analytical and numerical evidence that in systems endowed with a specific frequency, at the bifurcation point the gap is small but nonzero. Moreover, we lay down the construction of perturbative 2-dimensional approximation to the full delayed dynamics, expanding in the gap between delay and period, and prove at the first two lowest order that these approximations exhibit the same bifurcation of the full system, thus providing evidence towards the planarity of the bifurcation, at least at its onset. This is a particularly remarkable feature, especially in reference to the phenomenon of spontaneous dimensionality reduction, often observed in datasets obtained from Complex Systems, where highly dimensional data prove to contain in fact very few independent or significative dimensions. Considering our original problem concerning a FitzHugh-Nagumo model neuron, by building a set of normal coordinates near its fixed point we are able to show the existence of a quasi-invariant orbit in a quasi-adiabatic setting, and we confirm numerically that a skew delay coupling can stabilize it. We remark though that the case in which we are able to build the coordinate mapping is not the original one, as we must enforce a specific condition on the timescale separation ε to be able to construct it. Despite this, we expect that in the original setting the bifurcation mechanism shall be the same, if an adequate set of normal coordinates is constructed in the vicinity of the origin of the initial coordinates. Finally we observe that a directed loop of this type of simplified units can show analogous states to those of the DDE, with a few difference and the presence of some more complicated states, which are worthy of further investigation. A natural continuation of this chapter's work can be developed mainly along one of three lines. The first and foremost would be the formulation of an analogous approach for systems that do not have a proper period, such as the original FitzHugh-Nagumo neuron with its parameters taken at the values of chapters 1, 2 and 4, which is an example of overdamped oscillator. We expect our approach to be extensible to this setting as in numerical simulations we still observe a small but finite difference between feedback delay and period, which we believe to be the hallmark of the described stabilization mechanism. The second line would have to contend with the formulation of adequate normal coordinates centered in the coordinate origin, which is a highly unstable area for the dynamics. This is to some extent correlated with the first line, and could in principle allow for a full characterization of the FitzHugh-Nagumo system with our approach. Finally, the third line would deal with the further investigation of the DDE ↔ directed loop relationship, and investigate the more complicated states that have so far been just observed on a loop of simplified systems.

In **Chapter 4** we have approached the reconstruction of the firing statistics for a FitzHugh-Nagumo neuron in the presence of a stochastic input, with the ultimate goal of constructing a simpler binary model to be used in information theoretical approaches. To this end we have developed an original approach, based on the approximate separation of dynamical timescales and Kramers escape rate theory. By introducing a self interaction between the time since the last firing and the probability of firing after a certain time, we are able to reconstruct the shape of the InterSpike Interval distribution from first principles. Due to emergent correlations in the noise, our approximations hold only partially, and the system parameters have to be inferred from a statistical sample of the full system. If this datum is available, although, through a simple regression procedure we can fit a discrete model to the data and replicate the isolated neuron firing statistics. We devise a minimal coupling strategy to study networked systems, but this proves to be satisfactory only to a qualitative level, highlighting once again that the interplay of activation and propagation timescales in this type of system cannot be simplified straightforwardly, under risk of the removal of the destruction of dynamical stationary states, which may be meaningful in applications and real systems. A furthering of this research line should primarily deal with the parametric-noise like effects, and account for the interaction between slow and fast local timescales of the neuron, i.e. for the lack of full separability of the dynamics. Concentrating one's view on the networking of the binary systems, on the other hand, one should investigate possibilities for the improvement of the correspondence between networked noisy FitzHugh-Nagumo units and the simplified ones, a possible direction being the introduction of inter-unit explicit discrete delays. Once these developments have been considered, the natural application of these models would consist in the contextualization of concepts like channel capacity in more realistic neural models with respect to what is available in past literature, in particular with respect to systems that can evolve different encoding and information passing strategies. In **Chapter 5** we have turned our attention to the use of distributed delay equations for the short term *nowcasting* of the course of pandemic events in a metropolitan area. We show that distributed delay equations are the right tool for this type of task as they encompass both the differences and the inter-individual variability of timescales in respiratory pandemic diseases such as the SARS-CoV-2 disease. In addition to this we have performed a parametric linear response analysis for this type of model, a contribution we were not able to find elsewhere in literature, which despite some approximations allows us to quantify the impact of a change in restrictions on the population of infectious individuals after a certain time, and highlight that effective restriction strategies improve both the actual pandemic situation and the accuracy of the model predictions. A comparison of urban mobility open data and of the time series of the effective sociability parameter inferred from clinical data through the model has also highlighted the important role that the integration of this type of information can play in a pandemic containment context. Indeed, provided that *soft measures* such as social distancing and personal protection devices regulations or climatic conditions do not change too significantly during the period of interest, these anonymous mobility data can provide a useful proxy for the average sociability in the metropolitan area. The main development of interest for this line of work consists in the further study of the regression problem, so to better formalize it and tackle it with the appropriate tools. In particular building on the linear response results, it would be important to fully extend them to the flows, such as that from the Unreported to the Isolated Infected compartment, which are actually observed, so to pave the road to the solution of the regression on clinical data in terms of the solution of a constrained optimization problem.

Bibliography

[1] I. Akjouj *et al.* "Complex systems in ecology: a guided tour with large Lotka-Volterra models and random matrices". *Proceedings of the Royal Society A: Mathematical, Physical and Engineering Sciences* 480(2285) (Mar. 6, 2024). Publisher: Royal Society, p. 20230284. doi: `10.1098/rspa.2023.0284`.

[2] B. Al Beattie, P. Feketa, K. Ochs, and H. Kohlstedt. "Criticality in FitzHugh-Nagumo oscillator ensembles: Design, robustness, and spatial invariance". *Communications Physics* 7(1) (Feb. 2, 2024). Publisher: Nature Publishing Group, pp. 1–14. issn: 2399-3650. doi: `10.1038/s42005-024-01530-y`.

[3] R. M. Anderson, H. Heesterbeek, D. Klinkenberg, and T. D. Hollingsworth. "How will country-based mitigation measures influence the course of the COVID-19 epidemic?" *The Lancet* 395(10228) (2020), pp. 931–934. doi: `10.1016/S0140-6736(20)30567-5`.

[4] H. Andersson and T. Britton. "Density dependent jump Markov processes". *Stochastic Epidemic Models and Their Statistical Analysis*. Ed. by H. Andersson and T. Britton. New York, NY: Springer, 2000, pp. 39–49. isbn: 978-1-4612-1158-7. doi: `10.1007/978-1-4612-1158-7_5`.

[5] D. Angeli. "A tutorial on Chemical Reaction Networks dynamics". *2009 European Control Conference (ECC)*. 2009 European Control Conference (ECC). Aug. 2009, pp. 649–657. doi: `10.23919/ECC.2009.7074477`. (Visited on 10/22/2024).

[6] B. Armbruster and E. Beck. "Elementary proof of convergence to the mean-field model for the SIR process". *Journal of Mathematical Biology* 75(2) (Aug. 1, 2017), pp. 327–339. issn: 1432-1416. doi: `10.1007/s00285-016-1086-1`.

[7] V. I. Arnol'd, V. V. Kozlov, and A. I. Neishtadt. *Mathematical Aspects of Classical and Celestial Mechanics*. Vol. 3. Springer, 2006.

[8] A. G. Balanov, N. B. Janson, and E. Schöll. "Delayed feedback control of chaos: Bifurcation analysis". *Physical Review E – Statistical, Nonlinear, and Soft Matter Physics* 71(1) (2005), p. 016222.

[9] D. S. Bassett, P. Zurn, and J. I. Gold. "On the nature and use of models in network neuroscience". *Nature Reviews Neuroscience* 19(9) (Sept. 2018). Publisher: Nature Publishing Group, pp. 566–578. issn: 1471-0048. doi: `10.1038/s41583-018-0038-8`.

[10] A. Bayani *et al.* "The transition to synchronization of networked systems". *Nature Communications* 15(1) (June 10, 2024). Publisher: Nature Publishing Group, p. 4955. issn: 2041-1723. doi: `10.1038/s41467-024-48203-6`.

[11] A. Bazzani, E. Lunedei, and S. Rambaldi. "A stochastic compartmental model to simulate the Covid-19 epidemic spread on a simple network". eng. *Theoretical Biology Forum* 113(1-2) (Jan. 2020), pp. 31–46. issn: 2282-2593. doi: `10.19272/202011402004`.

[12] N. Berglund and B. Gentz. "Beyond the Fokker-Planck equation: pathwise control of noisy bistable systems". *Journal of Physics A: Mathematical and General* 35(9) (Feb. 2002), p. 2057. issn: 0305-4470. doi: `10.1088/0305-4470/35/9/301`.

[13] N. Berglund and B. Gentz. *Noise-Induced Phenomena in Slow-Fast Dynamical Systems*. Probability and Its Applications. London: Springer-Verlag, 2006. isbn: 978-1-84628-038-2. doi: `10.1007/1-84628-186-5`.

[14] N. Berglund and D. Landon. "Mixed-mode oscillations and interspike interval statistics in the stochastic FitzHugh–Nagumo model". *Nonlinearity* 25(8) (2012), p. 2303.

[15] M. A. Billah, M. M. Miah, and M. N. Khan. "Reproductive number of coronavirus: A systematic review and meta-analysis based on global level evidence". *PLoS ONE* 15(11) (Nov. 2020), e0242128. issn: 1932-6203. doi: `10.1371/journal.pone.0242128`.

[16] G. D. Birkhoff. "Surface transformations and their dynamical applications". *Acta Mathematica* 43(1) (Dec. 1, 1922), pp. 1–119. issn: 1871-2509. doi: `10.1007/BF02401754`.

[17] H. W. Broer. "Normal Forms in Perturbation Theory". *Encyclopedia of Complexity and Systems Science*. Ed. by R. A. Meyers. New York, NY: Springer New York, 2009, pp. 6310–6329. isbn: 978-0-387-30440-3. doi: `10.1007/978-0-387-30440-3_372`.

[18] F. R. Chung. *Spectral Graph Theory*. CBMS Regional Conference Series No. 92. Conference Board of the Mathematical Sciences, 1997. ISBN: 978-0-8218-8936-7.

[19] A. C. C. Coolen, R. Kühn, and P. Sollich. *Theory of Neural Information Processing Systems*. Oxford University Press, July 2005. ISBN: 9780198530237. DOI: `10.1093/oso/9780198530237.001.0001`.

[20] R. S. Costa, A. Hartmann, and S. Vinga. "Kinetic modeling of cell metabolism for microbial production". *Journal of Biotechnology* 219 (Feb. 10, 2016), pp. 126–141. ISSN: 0168-1656. DOI: `10.1016/j.jbiotec.2015.12.023`.

[21] D. Dasgupta, ed. *Artificial Immune Systems and Their Applications*. Berlin, Heidelberg: Springer, 1999. ISBN: 978-3-642-64174-9. DOI: `10.1007/978-3-642-59901-9`. (Visited on 10/22/2024).

[22] M. M. Dekker, A. S. von der Heydt, and H. A. Dijkstra. "Cascading transitions in the climate system". *Earth System Dynamics* 9(4) (Nov. 6, 2018). Publisher: Copernicus GmbH, pp. 1243–1260. ISSN: 2190-4979. DOI: `10.5194/esd-9-1243-2018`.

[23] L. Dell'Anna. "Solvable delay model for epidemic spreading: the case of Covid-19 in Italy". en. *Scientific Reports* 10(1) (Sept. 2020). Publisher: Nature Publishing Group, p. 15763. ISSN: 2045-2322. DOI: `10.1038/s41598-020-72529-y`.

[24] L. Di Meco, M. Degli Esposti, F. Bellisardi, and A. Bazzani. "Congestion Transition on Random Walks on Graphs". *Entropy* 26(8) (Aug. 2024). Number: 8 Publisher: Multidisciplinary Digital Publishing Institute, p. 632. ISSN: 1099-4300. DOI: `10.3390/e26080632`.

[25] O. Diekmann and J. A. P. Heesterbeek. *Mathematical epidemiology of infectious diseases: model building, analysis and interpretation*. Vol. 5. John Wiley & Sons, 2000.

[26] O. Diekmann, J. A. P. Heesterbeek, and M. G. Roberts. "The construction of next-generation matrices for compartmental epidemic models". *Journal of the Royal Society Interface* 7(47) (June 6, 2010), pp. 873–885. ISSN: 1742-5689. DOI: `10.1098/rsif.2009.0386`.

[27] I. R. Epstein. "Delay effects and differential delay equations in chemical kinetics". *International Reviews in Physical Chemistry* 11(1) (1992), pp. 135–160. DOI: `10.1080/01442359209353268`.

[28] E. Estrada. *The structure of complex networks: theory and applications*. American Chemical Society, 2012.

[29] R. FitzHugh. "Impulses and physiological states in theoretical models of nerve membrane". *Biophysical journal* 1(6) (1961). Publisher: Elsevier, pp. 445–466.

[30] L. J. Gentet, G. J. Stuart, and J. D. Clements. "Direct Measurement of Specific Membrane Capacitance in Neurons". *Biophysical Journal* 79(1) (2000), pp. 314–320.

[31] L. Glass *et al.* "Nonlinear dynamics, chaos and complex cardiac arrhythmias". *Proceedings of the Royal Society of London. A. Mathematical and Physical Sciences* 413(1844) (Jan. 1997). Publisher: Royal Society, pp. 9–26. doi: `10.1098/rspa.1987.0097`.

[32] J. L. González-Santander, G. Spada, F. Mainardi, and A. Apelblat. "Calculation of the Relaxation Modulus in the Andrade Model by Using the Laplace Transform". *Fractal and Fractional* 8(8) (Aug. 2024). Number: 8 Publisher: Multidisciplinary Digital Publishing Institute, p. 439. issn: 2504-3110. doi: `10.3390/fractalfract8080439`.

[33] J. M. Gottman *et al. The Mathematics of Marriage: Dynamic Nonlinear Models*. MIT Press, Jan. 14, 2005. 428 pp. isbn: 978-0-262-25045-0.

[34] D. M. Grobman. "Homeomorphisms of systems of differential equations". *Doklady Akademii Nauk SSSR* (128) (1959), pp. 880–881.

[35] N. Guglielmi and E. Hairer. "Implementing Radau IIA methods for stiff delay differential equations". *Computing* 67(1) (2001), pp. 1–12. issn: 0010-485X,1436-5057. doi: `10.1007/s006070170013`.

[36] N. Guglielmi and E. Hairer. "Computing breaking points in implicit delay differential equations". *Adv. Comput. Math.* 29(3) (2008), pp. 229–247. issn: 1019-7168,1572-9044. doi: `10.1007/s10444-007-9044-5`.

[37] N. Guglielmi and E. Hairer. "Order stars and stability for delay differential equations". *Numer. Math.* 83(3) (1999), pp. 371–383. issn: 0029-599X,0945-3245. doi: `10.1007/s002110050454`.

[38] N. Guglielmi, E. Iacomini, and A. Viguerie. "Delay differential equations for the spatially resolved simulation of epidemics with specific application to COVID-19". *Mathematical Methods in the Applied Sciences* 45(8) (May 2022), pp. 4752–4771. issn: 0170-4214. doi: `10.1002/mma.8068`.

[39] E. Hairer and G. Wanner. "Solving ordinary differential equations II". Vol. 375. Springer Berlin Heidelberg New York, 1996. Chap. IV.8.

[40] H. Harapan *et al.* "Effect of elevated temperature on SARS-CoV-2 viability". *F1000Research* 11 (June 15, 2023), p. 403. ISSN: 2046-1402. DOI: `10.12688/f1000research.110305.2`.

[41] P. Hartman. "A lemma in the theory of structural stability of differential equations". *Proceedings of the American Mathematical Society* 11(4) (1960), pp. 610–620. ISSN: 0002-9939, 1088-6826. DOI: `10.1090/S0002-9939-1960-0121542-7`.

[42] C. Hens *et al.* "Spatiotemporal signal propagation in complex networks". *Nature Physics* 15(4) (Apr. 2019). Publisher: Nature Publishing Group, pp. 403–412. ISSN: 1745-2481. DOI: `10.1038/s41567-018-0409-0`.

[43] H. W. Hethcote. "The Mathematics of Infectious Diseases". *SIAM Review* 42(4) (2000), pp. 599–653. DOI: `10.1137/S0036144500371907`.

[44] H. W. Hethcote. "Three Basic Epidemiological Models". *Applied Mathematical Ecology*. Ed. by S. A. Levin, T. G. Hallam, and L. J. Gross. Berlin, Heidelberg: Springer Berlin Heidelberg, 1989, pp. 119–144. ISBN: 978-3-642-61317-3. DOI: `10.1007/978-3-642-61317-3_5`.

[45] J. L. Hindmarsh, R. M. Rose, and A. F. Huxley. "A model of neuronal bursting using three coupled first order differential equations". *Proceedings of the Royal Society of London. Series B. Biological Sciences* 221(1222) (Jan. 1997). Publisher: Royal Society, pp. 87–102. DOI: `10.1098/rspb.1984.0024`.

[46] J. L. Hindmarsh, R. M. Rose, and A. F. Huxley. "A model of neuronal bursting using three coupled first order differential equations". *Proceedings of the Royal Society of London. Series B. Biological Sciences* 221(1222) (Jan. 1997). Publisher: Royal Society, pp. 87–102. DOI: `10.1098/rspb.1984.0024`.

[47] A. L. Hodgkin and A. F. Huxley. "A quantitative description of membrane current and its application to conduction and excitation in nerve". *The Journal of physiology* 117(4) (1952). Publisher: Wiley Online Library, pp. 500–544.

[48] A. L. Hodgkin and A. F. Huxley. "A quantitative description of membrane current and its application to conduction and excitation in nerve". *The Journal of Physiology* 117(4) (Aug. 28, 1952), p. 500. DOI: `10.1113/jphysiol.1952.sp004764`.

[49] P. C. Hohenberg and A. P. Krekhov. "An introduction to the Ginzburg–Landau theory of phase transitions and nonequilibrium patterns". *Physics Reports* 572 (2015), pp. 1–42.

[50] J. J. Hopfield. "Neural networks and physical systems with emergent collective computational abilities". *Proceedings of the National Academy of Sciences of the United States of America* 79(8) (Apr. 1982), p. 2554. doi: `10.1073/pnas.79.8.2554`.

[51] S. Ikeda and J. H. Manton. "Capacity of a single spiking neuron channel". *Neural Computation* 21(6) (2009), pp. 1714–1748.

[52] Istituto Superiore di Sanità. *COVID-19 Special: Virus variants (italian: Speciale COVID-19: Varianti del virus)*. url: `https://www.iss.it/en/cov19-cosa-fa-iss-varianti`.

[53] E. M. Izhikevich. *Dynamical Systems in Neuroscience: The Geometry of Excitability and Bursting*. The MIT Press, July 2006. isbn: 978-0-262-27607-8.

[54] W. O. Kermack and A. G. McKendrick. "A Contribution to the Mathematical Theory of Epidemics". *Proceedings of the Royal Society of London. Series A, Containing Papers of a Mathematical and Physical Character* 115 (1927), pp. 700–721. doi: `10.1098/rspa.1927.0118`.

[55] H. A. Kramers. "Brownian motion in a field of force and the diffusion model of chemical reactions". *Physica* 7(4) (1940), pp. 284–304. issn: 0031-8914. doi: `https://doi.org/10.1016/S0031-8914(40)90098-2`.

[56] Y. Kuramoto. "Self-entrainment of a population of coupled non-linear oscillators". *International Symposium on Mathematical Problems in Theoretical Physics*. Ed. by H. Araki. Berlin, Heidelberg: Springer Berlin Heidelberg, 1975, pp. 420–422.

[57] P. Landi *et al.* "Complexity and stability of ecological networks: a review of the theory". *Population Ecology* 60(4) (Oct. 1, 2018), pp. 319–345. issn: 1438-390X. doi: `10.1007/s10144-018-0628-3`.

[58] S. A. Lauer *et al.* "The Incubation Period of Coronavirus Disease 2019 (COVID-19) From Publicly Reported Confirmed Cases: Estimation and Application". eng. *Annals of Internal Medicine* 172(9) (May 2020), pp. 577–582. issn: 1539-3704. doi: `10.7326/M20-0504`.

[59] J. Lehnert, T. Dahms, P. Hövel, and E. Schöll. "Loss of synchronization in complex neuronal networks with delay". *EPL (Europhysics Letters)* 96(6) (Mar. 2011). Publisher: IOP Publishing, p. 60013.

[60] J. Lehnert. *Controlling Synchronization Patterns in Complex Networks*. Springer Theses. Cham: Springer International Publishing, 2016. isbn: 978-3-319-25113-4. doi: `10.1007/978-3-319-25115-8`.

[61] R. Li *et al.* "Substantial undocumented infection facilitates the rapid dissemination of novel coronavirus (SARS-CoV-2)". *Science* 368(6490) (2020), pp. 489–493. DOI: `10.1126/science.abb3221`.

[62] A. Liénard. "Etude des oscillations entretenues". *Revue Générale de l'Électricité* 23 (1928), pp. 901–902.

[63] M. C. Mackey and L. Glass. "Oscillation and Chaos in Physiological Control Systems". *Science* 197(4300) (1977), pp. 287–289. DOI: `10.1126/science.267326`.

[64] T. T. Marinov and R. S. Marinova. "Adaptive SIR model with vaccination: simultaneous identification of rates and functions illustrated with COVID-19". *Scientific Reports* 12(1) (Sept. 20, 2022), p. 15688. ISSN: 2045-2322. DOI: `10.1038/s41598-022-20276-7`.

[65] W. S. McCulloch and W. Pitts. "A logical calculus of the ideas immanent in nervous activity". *The bulletin of mathematical biophysics* 5(4) (Dec. 1, 1943), pp. 115–133. ISSN: 1522-9602. DOI: `10.1007/BF02478259`.

[66] C. Mizzi *et al.* "A survival model to explain the statistical properties of multimodal mobility". *Journal of Statistical Mechanics: Theory and Experiment* 2022(2) (Feb. 2022). Publisher: IOP Publishing and SISSA, p. 023404. ISSN: 1742-5468. DOI: `10.1088/1742-5468/ac4c40`.

[67] C. Mizzi *et al.* "Unraveling pedestrian mobility on a road network using ICTs data during great tourist events". *EPJ Data Science* 7(1) (Dec. 1, 2018). Number: 1 Publisher: Springer Berlin Heidelberg, p. 44. ISSN: 2193-1127. DOI: `10.1140/epjds/s13688-018-0168-2`.

[68] T. Nagatani. "Modified KdV equation for jamming transition in the continuum models of traffic". *Physica A: Statistical Mechanics and its Applications* 261(3) (Dec. 15, 1998), pp. 599–607. ISSN: 0378-4371. DOI: `10.1016/S0378-4371(98)00347-1`.

[69] T. Nagatani. "Modified KdV equation for jamming transition in the continuum models of traffic". *Physica A: Statistical Mechanics and its Applications* 261(3) (1998), pp. 599–607. ISSN: 0378-4371. DOI: `https://doi.org/10.1016/S0378-4371(98)00347-1`.

[70] T. Nagatani. "The physics of traffic jams". *Reports on progress in physics* 65(9) (2002), p. 1331.

[71] J. Nagumo, S. Arimoto, and S. Yoshizawa. "An active pulse transmission line simulating nerve axon". *Proceedings of the IRE* 50(10) (1962). Publisher: IEEE, pp. 2061–2070.

[72] M. Newman. *Networks*. Oxford University Press, July 2018. isbn: 978-0-19-880509-0. doi: `10.1093/oso/9780198805090.001.0001`.

[73] M. Nowak and R. M. May. *Virus Dynamics : Mathematical Principles of Immunology and Virology: Mathematical Principles of Immunology and Virology*. Oxford University Press, UK, Nov. 23, 2000. 253 pp. isbn: 978-0-19-158851-8.

[74] R. Pastor-Satorras, C. Castellano, P. Van Mieghem, and A. Vespignani. "Epidemic processes in complex networks". *Reviews of Modern Physics* 87(3) (Aug. 31, 2015). Publisher: American Physical Society, pp. 925–979. doi: `10.1103/RevModPhys.87.925`.

[75] L. M. Pecora and T. L. Carroll. "Master Stability Functions for Synchronized Coupled Systems". *Phys. Rev. Lett.* 80(10) (Mar. 1998). Publisher: American Physical Society, pp. 2109–2112.

[76] S. A. Plotnikov and A. L. Fradkov. "On synchronization in heterogeneous FitzHugh-Nagumo networks". *Chaos, Solitons & Fractals* 121 (Apr. 1, 2019), pp. 85–91. issn: 0960-0779. doi: `10.1016/j.chaos.2019.02.006`.

[77] A. Polynikis, S. Hogan, and M. Di Bernardo. "Comparing different ODE modelling approaches for gene regulatory networks". *Journal of theoretical biology* 261(4) (2009), pp. 511–530.

[78] Progetto Open Data Comune di Bologna. *Rilevazione flusso veicoli tramite spire - anno 2020*. url: `https://opendata.comune.bologna.it/explore/dataset/rilevazione-autoveicoli-tramite-spire-anno-2020/`.

[79] Progetto Open Data Comune di Bologna. *Rilevazione flusso veicoli tramite spire - anno 2021*. url: `https://opendata.comune.bologna.it/explore/dataset/rilevazione-autoveicoli-tramite-spire-anno-2021/`.

[80] Progetto Open Data Comune di Bologna. *Rilevazione flusso veicoli tramite spire - anno 2022*. url: `https://opendata.comune.bologna.it/explore/dataset/rilevazione-flusso-veicoli-tramite-spire-anno-2022/`.

[81] K. Pyragas. "Continuous control of chaos by self-controlling feedback". *Physics Letters A* 170(6) (Nov. 23, 1992), pp. 421–428. issn: 0375-9601. doi: `10.1016/0375-9601(92)90745-8`.

[82] K. Pyragas. “Delayed feedback control of chaos”. *Philosophical Transactions of the Royal Society A: Mathematical, Physical and Engineering Sciences* 364(1846) (July 27, 2006). Publisher: Royal Society, pp. 2309–2334. DOI: `10.1098/rsta.2006.1827`.

[83] V. Ram and L. P. Schaposnik. “A modified age-structured SIR model for COVID-19 type viruses”. *Scientific Reports* 11(1) (July 26, 2021), p. 15194. ISSN: 2045-2322. DOI: `10.1038/s41598-021-94609-3`.

[84] A. Rapoport and W. J. Horvath. “The theoretical channel capacity of a single neuron as determined by various coding systems”. *Information and control* 3(4) (1960), pp. 335–350.

[85] A. Reyna-Lara *et al.* “A metapopulation approach to identify targets for Wolbachia-based dengue control”. *Chaos: An Interdisciplinary Journal of Nonlinear Science* 32(4) (Apr. 2022), p. 041105. ISSN: 1054-1500. DOI: `10.1063/5.0087435`.

[86] F. A. Rihan and H. J. Alsakaji. “Dynamics of a stochastic delay differential model for COVID-19 infection with asymptomatic infected and interacting people: Case study in the UAE”. *Results in Physics* 28 (Sept. 2021), p. 104658. ISSN: 2211-3797. DOI: `10.1016/j.rinp.2021.104658`.

[87] N. F. Rulkov. “Modeling of spiking-bursting neural behavior using two-dimensional map”. *Physical Review E* 65(4) (Apr. 10, 2002). Publisher: American Physical Society, p. 041922. DOI: `10.1103/PhysRevE.65.041922`.

[88] J. Schnakenberg. “Network theory of microscopic and macroscopic behavior of master equation systems”. *Reviews of Modern Physics* 48(4) (Oct. 1, 1976). Publisher: American Physical Society, pp. 571–585. DOI: `10.1103/RevModPhys.48.571`.

[89] C. M. Schneider *et al.* “Unravelling daily human mobility motifs”. *Journal of the Royal Society Interface* 10(84) (July 6, 2013), p. 20130246. DOI: `10.1098/rsif.2013.0246`.

[90] E. Schöll and H. G. Schuster. “Handbook of Chaos Control” (2008).

[91] M. C. Soriano, J. Garcia-Ojalvo, C. R. Mirasso, and I. Fischer. “Complex photonics: Dynamics and applications of delay-coupled semiconductors lasers”. *Rev. Mod. Phys.* 85(1) (2013).

[92] G. Tkačik and A. M. Walczak. “Information transmission in genetic regulatory networks: a review”. *Journal of Physics: Condensed Matter* 23(15) (Apr. 2011), p. 153102. ISSN: 0953-8984. DOI: `10.1088/0953-8984/23/15/153102`.

[93] A. Viguerie *et al.* "Diffusion–reaction compartmental models formulated in a continuum mechanics framework: application to COVID-19, mathematical analysis, and numerical study". *Computational Mechanics* 66 (2020), pp. 1131–1152.

[94] P. Virtanen *et al.* "SciPy 1.0: Fundamental Algorithms for Scientific Computing in Python". *Nature Methods* 17 (2020), pp. 261–272. doi: `10.1038/s41592-019-0686-2`.

[95] G. Wanner and E. Hairer. *Solving ordinary differential equations II*. Vol. 375. Springer Berlin Heidelberg, 1996.

[96] H. Wernecke, B. Sándor, and C. Gros. "Chaos in time delay systems, an educational review". *Physics Reports*. Chaos in time delay systems, an educational review 824 (Sept. 3, 2019), pp. 1–40. issn: 0370-1573. doi: `10.1016/j.physrep.2019.08.001`.

[97] N. Wunderling, J. F. Donges, J. Kurths, and R. Winkelmann. "Interacting tipping elements increase risk of climate domino effects under global warming". *Earth System Dynamics* 12(2) (2021), pp. 601–619. doi: `10.5194/esd-12-601-2021`.

[98] S. Yanchuk, S. Ruschel, J. Sieber, and M. Wolfrum. "Temporal dissipative solitons in time-delay feedback systems". *Physical review letters* 123(5) (2019), p. 053901.

Acknowledgements

> *Signori, di fuori*
> *son già i suonatori.*
>
> Wolfgang Amadeus Mozart,
> *Le Nozze di Figaro,*
> Atto Secondo, Scena IX.
> 1786, Vienna

In the development of the work presented in this Thesis, many contributions have been essential. First and foremost I would like to thank my supervisor Prof. Armando Bazzani for the numerous suggestions and enlightening help in navigating the many nonlinearities of Complex Systems Physics, and in developing all those ideas that probably would not have resulted in this work otherwise. My gratitude goes as well to Prof. Nicola Guglielmi of the Gran Sasso Science Institute for the many discussions on the interesting and often surprising topic of Delay Differential Equations, and especially for providing help, and the algorithms that made possible all of our numerical explorations. From my research visits in Vienna, I would like to thank Prof. Rudolf Hanel for the interesting discussions and the support in the development of many concepts and ideas for future development, and the Hub director Prof. Stefan Thurner for the hospitality. I would then like to thank all my colleagues at Physycom, the Complex Systems Physics group at the University of Bologna for the interesting and thought-provoking conversations, but also for the many moments of mutual support that are part of a Ph.D., so thank you Alberto, Aldo, Federico, Lorenzo and Filippo. I would also like to thank all the Ph.D.'s, Post-Docs and Researchers I interacted with in CSH and MedUni for making my experience much better, so thank you Simone, Leonardo, Giacomo, Mauritz, Alessandro, Şeyda, Vito, Sina, Jan, Samuel, Tim, Hana, Markus for providing countless interesting scientific discussions and many non-scientific, but still important ones.

During the journey of a Doctorate, the pursuit of non-scientific activities

is at least as important as that of scientific ones. For this reason I would like to start by thanking the Collegium Musicum Almae Matris for all the people I have met there in my musical activities, for letting me discover some beautiful music that has remained with me ever since and for all the moments spent performing it. Within the Collegium, special thanks must go to all the members, present and past, of the Corpo Filarmonico Universitario, the CFU, for having embarked together with me in what looked at first like an unlikely experiment, but has developed into a new ensemble of the association. For the possibility of performing music also during my period abroad, many thanks are addressed to the BOKU Blaskapelle as well, and to all the people I have met there. Seeing the Ph.D. as a continuation, although with many differences, of my years of B.Sc. and M.Sc. at the Department of Physics in Bologna, an important thank you is also in order for all the colleagues of those years, without whom the road would have for sure been more difficult. Many friends that I would like to thank particularly fall in none, or in too many, of the former categories, therefore thank you Marco, Federico, Lorenzo, Lorenzo, Roberta, Michele, Andrea, Giacomo, Sofia and Giuseppe.

The most important thank you, finally, to my parents and grandparents, actual and acquired, for having sparked in me the curiosity that drove me through this path, and having supported me ever since.